

OCS INSTRUMENTATION
MONITORING EVALUATION

Prepared by
Energy and Resources Division
Resource Technology Directorate
THE AEROSPACE CORPORATION
El Segundo, California 90245

Principal Investigators: Sheldon Rubin and Robert N. Coppolino
Task Leader: J. Arthur Conley

June 1979

Contract No. 14-08-0001-17224

Contracting Officers Authorized Representative: R. Giangerelli

Prepared for
Conservation Division
Geological Survey
U.S. DEPARTMENT OF THE INTERIOR
Reston, Virginia 22092

Neither the Department of the Interior, The Aerospace Corporation, nor any person acting on behalf of either: (a) makes any warranty or representation, express or implied, with respect to the accuracy, completeness, or usefulness of the information contained in this report, or that the use of any information disclosed in this report does not infringe on privately owned rights; or (b) assumes any liability for loss or damage of any kind arising or resulting from the use of any information disclosed in this report.

ACKNOWLEDGEMENTS

The authors of this report acknowledge the many contributions of those who provided data and support to the research and analysis efforts discussed within this study. Particular thanks are extended to Mr. Ruhl of the Shell Development Company for providing the mathematical model of Platform C on South Pass OCS Tract 62 in The Gulf of Mexico and for sharing the results of Shell's tests on the same structure. Thanks are also due Miss J. E. Peach who contributed to the computer coding of the mathematical model.

CONTENTS

	Page
FOREWORD	ii
ACKNOWLEDGEMENTS	iii
1. INTRODUCTION	1-1
1.1 Goals and Objectives	1-3
1.2 Approach	1-3
2. MODE EXTRACTION FROM AMBIENT VIBRATIONS	2-1
2.1 Description of Field Test	2-1
2.2 Periodic Noise	2-5
2.3 Mechanization of Spectral Analysis	2-8
2.4 Full System Calibration	2-9
2.5 Discussion of Modal Results	2-11
2.6 Forced Vibration Testing Comparison	2-22
2.7 Summary and Conclusions	2-24
3. MATHEMATICAL MODEL OF PLATFORM	3-1
3.1 Approach	3-1
3.2 Jacket/Pile/Conductor Model	3-1
3.3 Deck Model	3-3
3.3.1 Stiffness Model	3-3
3.3.2 Deck Mass Distribution	3-6
3.3.3 Assembly of Dynamic Model of Decks	3-6
3.4 Fluid Virtual Mass	3-8
3.5 Foundation Model	3-11
3.6 Assembly of the Complete Mathematical Model	3-12
3.7 Adjustment of Model	3-14

CONTENTS (Continued)

	Page
4. DAMAGE SENSITIVITY STUDIES	4-1
4.1 Efficient Analysis Method	4-1
4.2 Interpretation of Analytical Sensitivity Data	4-6
4.3 Criteria for Failure Detection	4-10
4.4 Mode Observability	4-13
4.5 Failure Sensitivities for First Three Mode Groups	4-16
4.5.1 Face 4 Diagonal Member Failures	4-16
4.5.2 Face A Diagonal Member Failures	4-19
4.5.3 Face 3 Diagonal Member Failures	4-22
4.5.4 Horizontal Member Failures	4-22
4.5.5 Skirt Pile Diagonal Support Member Failures	4-25
4.5.6 Vertical Member and Main Pile Failures	4-25
4.5.7 Summary of Sensitivities and Detectability Judgments . .	4-28
4.6 Modal Sensitivity and Load Path Alteration	4-28
4.6.1 Frequency Sensitivity of the Fundamental Mode Group . .	4-28
4.6.2 Sensitivity of Simplified Platform Structures	4-32
4.7 Higher Mode Sensitivity	4-39
5. EVALUATION OF PROTOTYPE SYSTEM	5-1
5.1 Description of Instrumentation System	5-1
5.2 Data Analysis Method	5-5
5.3 Requirements for Field Testing	5-7
5.3.1 Program for Field Evaluation	5-7

CONTENTS (Continued)

	Page
5.3.2 Generalized Procedures for Installation, Calibration and Measurement Operations	5-8
6. CONCLUSIONS	6-1
7. RECOMMENDATIONS	7-1
REFERENCES	R-1
NOMENCLATURE	N-1
APPENDIX A. AMBIENT VIBRATION DATA	A-1
B. MASS DISTRIBUTION AND MODAL PLOTS	B-1
C. ACCELEROMETER TECHNOLOGY	C-1

TABLES

		Page
2-1	Observed Signal/Noise for Higher Modes	2-18
2-2	Summary of Mode Identification from Field Data on SP-62C (October 1977)	2-19
2-3	Tentative Comparison with Frequencies Determined from Forced Vibration Tests	2-23
3-1	Natural Frequencies for Model Adjustments Referenced to Measured and Supplied Frequencies	3-15
4-1	Comparison of Modal Frequencies from NASTRAN and Efficient Method (Member 4530 Failure)	4-5
4-2	Estimates of Thresholds for Detectability of Frequency Changes	4-12
4-3	Face 4 Diagonal Member Failure Modal Sensitivity	4-18
4-4	Face A Diagonal Member Failure Modal Sensitivity	4-20
4-5	Face 3 Diagonal Member Failure Modal Sensitivity	4-23
4-6	Face 4 Horizontal Member Failure Modal Sensitivity	4-24
4-7	Skirt Pile Diagonal Support Member Failure Modal Sensitivity	4-26
4-8	First Three Mode Groups and Summary of Frequency Changes by Failure Class and Judgment of Detectability	4-29
4-9	Wide Frequency Range Modal Frequency Sensitivity	4-40
4-10	Wide Frequency Range Mode Shape Sensitivity	4-42
4-11	Summary of Cross Section Warping Mode Sensitivity	4-44
5-1	Examples of Candidate Equipment for Prototype System	5-2
5-2	Examples of Record Lengths Required for Given Bandwidth and Number of Averages	5-6
A-1	Data Acquisition Runs	A-2
A-2	Data Analysis Runs	A-3
A-3	Mode Shape Parameters	A-5
B-1	Deck Mass Distribution	B-2

FIGURES

	Page
2-1 View of SP-62C	2-2
2-2 Base Section of SP-62C	2-2
2-3 Accelerometer Locations	2-4
2-4 Autospectrum of X (A1-14) for B = 0.06 Hz, BT = 57.6, 20 Hz Low Pass Filter	2-6
2-5 Tape Recorder Noise Peaks	2-7
2-6 Typical Results for Relative Calibration of Two Signal Paths	2-10
2-7 Autospectrum of \ddot{X} (A1-14) for B = 0.03 Hz, BT = 28.8	2-12
2-8 Autospectrum of \ddot{Z} (A1-49) for B = 0.03 Hz, BT = 28.8	2-13
2-9 Autospectrum of $\ddot{\theta}_z$ (A1-49) for B=0.03 Hz, BT = 28.8	2-14
2-10 Typical Coherences for B = 0.03 Hz, BT = 28.8	2-15
2-11 Experimentally Detected Deck Motion Shape for Well Identified Modes .	2-17
3-1 Jacket/Pile/Conductor Model Configuration	3-2
3-2 Structural Idealization of Decks	3-4
3-3 Interdeck Trusswork Member Configurations	3-5
3-4 Member Network for Floors	3-7
3-5 Arbitrarily Oriented Cylindrical Beam	3-9
3-6 Assembly of Mathematical Model	3-13
3-7 Illustration of Reduced Mathematical Model Degrees of Freedom . . .	3-16
4-1 Lateral Modal Deflection Patterns in a Corner Leg	4-14a,b
4-2 Modal Amplitudes at Various Upper Platform Stations	4-15
4-3 Identification of Member Failure Cases	4-17
4-4 Vertical Member Failure Modal Sensitivity	4-27
4-5 Typical Idealized Platform for Mode/Load Sensitivity Evaluation	4-30

FIGURES (Continued)

	Page
4-6 Description of Structural Configurations Used for Sensitivity Studies . . .	4-35
4-7 Frequency Sensitivity of Fundamental Mode Group for Failure of a Single Diagonal Member.	4-36
4-8 Simplified Model Load Sensitivity Versus Frequency Sensitivity for Failure of a Single Diagonal Member	4-37
4-9 Illustration of Cross-Sectional Shape of Warping Mode at 14 ft (4.3 m) Level	4-43
5-1 Sunstrand QA 1300 Accelerometer	5-3
5-2 Arrangements of Accelerometers	5-10
B-1 Mode Shape 1, 0.639 Hz	B-4
B-2 Mode Shape 2, 0.659 Hz	B-5
B-3 Mode Shape 3, 0.935 Hz	B-6
B-4 Mode Shape 4, 1.50 Hz	B-7
B-5 Mode Shape 5, 1.53 Hz	B-8
B-6 Mode Shape 6, 1.69 Hz	B-9
B-7 Mode Shape 7, 1.85 Hz	B-10
B-8 Mode Shape 8, 1.88 Hz	B-11
B-9 Mode Shape 9, 1.89 Hz	B-12
B-10 Mode Shape 10, 1.92 Hz	B-13
B-11 Mode Shape 11, 2.00 Hz	B-14
B-12 Mode Shape 12, 2.43 Hz	B-15
B-13 Mode Shape 13, 2.68 Hz	B-16
B-14 Mode Shape 14, 3.08 Hz	B-17
B-15 Mode Shape 15, 3.13 Hz	B-18
B-16 Mode Shape 16, 3.14 Hz	B-19
B-17 Mode Shape 17, 3.28 Hz	B-20

FIGURES (Continued)

	Page
B-18 Mode Shape 18, 3.53 Hz	B-21
B-19 Mode Shape 19, 3.71 Hz	B-22
B-20 Mode Shape 20, 3.81 Hz	B-23
B-21 Mode Shape 21, 3.97 Hz	B-24
B-22 Mode Shape 22, 4.13 Hz	B-25
C-1 Schematic Design of Hinged Pendulum Accelerometer	C-2
C-2 Sunstrand QA 1300 Accelerometer	C-4
C-3 Schematic of the Systron Donner Angular Accelerometer	C-7
C-4 Systron Donner Model 4590F Angular Accelerometer	C-8
C-5 Mounting of Three Translational and One Angular Accelerometer	C-9
C-6 Rear View of the Accelerometer Illustrating the Glued Pad and Mounting Legs	C-10
C-7 Mounting Fixture with Three FBA-1 Accelerometers	C-11
C-8 Accelerometer Locations	C-12
C-9 Instrumentation Flow Chart	C-13
C-10 Instrumentation	C-14
C-11 Attaching Pad	C-15
C-12 Mounting Fixture Attached to Simulated Leg of Platform	C-16
C-13 Two Translational Accelerometers Mounted on B-4 Leg	C-17
C-14 Angular Accelerometer Mounted on Leg	C-18

I. INTRODUCTION

The quest for the discovery of new oil and gas deposits has driven government and industry to expanded exploration of the Outer Continental Shelf (OCS) for new sources of supply. The hostile environments encountered in these explorations have stimulated considerable effort in the formulation of new methods for verification of the structural integrity of fixed offshore platforms. Progressively larger structures, deeper waters and more severe weather conditions have prompted a growing concern for the safety of diving personnel required for underwater inspections, and the risk to platform crews and the environment from structural failures that may occur.

Historically, the structural integrity of fixed offshore platforms has been periodically assessed through the use of divers or remotely controlled unmanned submersibles for inspection. These methods have also been used to perform inspections after storms or other occurrences which could damage the platform. Even in fairly shallow waters, these techniques for inspection are only marginally effective, are time consuming and are costly, becoming exorbitant in deeper OCS areas where saturation diving is required. As a consequence, platform monitoring techniques are desired which reduce inspection costs and provide a reliable indicator for the performance of detailed inspections. The U.S. Geological Survey (USGS) considers such platform monitoring techniques as potentially useful in their OCS Platform Verification Programs.

In response to this need, the USGS initiated a study in October 1976 with the Aerospace Corporation under Contract 14-08-0001-15989 to (a) review existing inspection approaches in the United States and the North Sea; (b) perform analyses of selected options; and (c) develop alternative instrumentation configurations for possible operational applications. This study was completed in October 1977 and is covered in Aerospace Report No. ATR-77(7627-02)-1, "Instrumentation of Fixed OCS Platforms". In the latter stages of that contract, actual physical measurements were performed on an existing offshore platform (Shell Oil Company's Platform C on South Pass OCS Tract 62 in the Gulf of Mexico) to assess one of the options studied. These measurements were performed using a mix of linear

and angular accelerometers for vibration analysis. A quick look at the data gathered offered encouragement for the possible feasibility of an ambient vibration monitoring technique, and the need for further analytical evaluations were identified.

Optimism for ambient vibration monitoring had also been evident from other sources such as measurements made on two relatively simple Coast Guard towers and their companion analytical studies (19, 20)*. In addition, the technique has been developed in Great Britain to the point where substantial application has been made in the North Sea. It has been stated that "measurements made on 18 different structures have shown that on many steel platforms, the changes in natural frequencies caused by failure of a single, structurally important member are large enough to be detected unambiguously" (6). Moreover, it was stated that difficulties may be encountered with squat platforms (base dimensions comparable to height) and platforms which exhibit strong nonlinearities due to pile/soil or pile/jacket interaction (such as occur in ungrouted piles); the latter difficulty may be overcome if the monitoring is limited to amplitudes lower than those which develop the nonlinearities. The ability to detect failure of members of lesser structural importance or of partially failed members (i.e., not completely severed) was not claimed.

In the above mentioned Aerospace study, it was not possible to fully evaluate the North Sea applications because of proprietary restrictions. That fact led to the tests performed on the Shell platform as a means of addressing matters of instrumentation, data analysis, interference from operating machinery, modal identification and the effects of a high degree of structural redundancy. The Shell platform was located in 327 ft (100 m) of water, and until a few years ago, was among the taller structures in the Gulf. A total of 26 hours of ambient vibration data were recorded, which included periods of both calm and stormy sea conditions. These basic data, after the mentioned quick look analysis, were to be utilized as a basis for a subsequent study to evaluate further the utility of the vibration monitoring concept.

The ensuing contract (14-08-0001-17224) was let by the USGS to The Aerospace Corporation in September 1978 and the results of that effort are contained herein. The guidelines used for the study are presented in the following.

*Numbers in parenthesis are references.

1.1 GOALS AND OBJECTIVES

The primary goals of this study were to analyze the previously gathered measured data on the Shell platform using computer technology to evaluate the diagnostic capabilities of the technique, its capabilities and limitations and its overall feasibility. Specific objectives included:

- Perform a detailed analysis of the recorded ambient vibration data and extract modal frequencies and shape parameters.
- Develop a dynamic model of the subject offshore platform which yields modes in good agreement with those measured.
- Determine modal changes associated with single structural failures using the dynamic model.
- Develop a plan for evaluating prototype instrumentation.

In addition to the above, the general guidelines that were used to structure a candidate monitoring system were:

- Be capable of detecting failures that are considered significant to the strength and safety of the structure and its personnel.
- Be cost-effective, in that the cost of the monitoring and recording equipment and its operation should be more than offset by the savings incurred by reducing the use of divers and submersibles.
- Utilize off-the-shelf hardware wherever possible.
- Be adaptable to either permanent installation or portable utilization.

1.2 APPROACH

The approach taken in this study to evaluate the vibration monitoring technique consisted of the following steps:

- Extract modal parameters (natural frequencies and mode shapes) from the field measured dynamic response data via determination of autospectral densities and transfer functions for pairs of measurement locations.
- Develop a baseline mathematical dynamic model of the platform by refinement of a design model to bring the lower modes of vibration into good agreement with those extracted from the field data.
- Employ the baseline model to predict changes in the modal parameters for various representative member failures.

- Assess the predicted modal changes and make an engineering judgement about the likelihood of detection with this technique.
- Judge the likelihood of detection relative to the significance of a failure from the standpoint of overall platform structural integrity.

The following sections present coverage of the mode extraction, mathematical model of the platform, damage sensitivity studies, evaluation of a prototype system candidate, conclusions, recommendations and detailed backup appendices.

2. MODE EXTRACTION FROM AMBIENT VIBRATIONS

2. MODE EXTRACTION FROM AMBIENT VIBRATIONS

This section describes the evaluation of the measured ambient vibration data from the SP-62C platform and the subsequent extraction of natural frequencies and mode shapes. The previous report and a paper contain a detailed description of the instrumentation and preliminary data evaluation (2, 18). For completeness, selected material from that report is included herein. The field test is reviewed briefly, followed by a description of the data analysis and results. Further, a tentative comparison is made with results from forced vibration tests performed on SP-62C subsequent to the work reported here (17).

2.1 DESCRIPTION OF FIELD TEST

The instrumented platform is an eight-leg diagonally braced jacket construction supporting two full decks (Figures 2-1 and 2-2). The lower deck (production deck) measures 85 by 165 ft (26 by 50 m), and the deck beams are centered at 49 ft (15 m) above the sea surface. The platform stands in 327 ft (100 m) of water and is located about 55 mi (40 km) east of the mouth of the Mississippi River. The main legs are 4.5 ft (1.4 m) in diameter and are battered (sloped) 1:10, as seen in Figure 2-2. Each main leg contains a pile driven through and welded just above the 14 ft (4.3 m) level. The eight main piles are ungrouted. In addition, eight skirt piles are driven through guide sleeves at the base of the jacket and are grouted in place.

Of the several possible platforms offered for our study by the Shell Oil Company, this particular one was selected because of its prior history of experimental and analytical studies (16). Specifically, a mathematical structural dynamic model was available, and measurements had been made of its fundamental natural frequencies on several occasions by Shell Oil Company.

The literature implies the use of lateral accelerometers for the monitoring. For this investigation, it was decided to look into the additional benefit of vertically directed accelerometers and angular accelerometers. The accelerometers were all of the force-balance type which quite comfortably meet the frequency

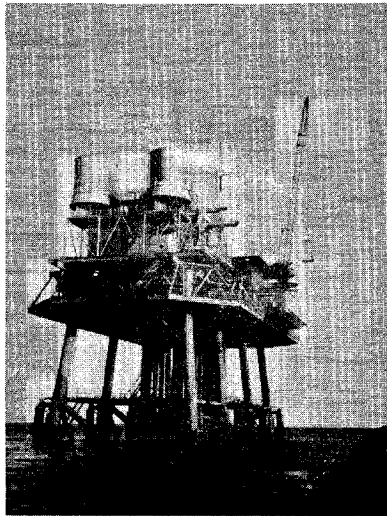


Figure 2-1. View of SP-62C

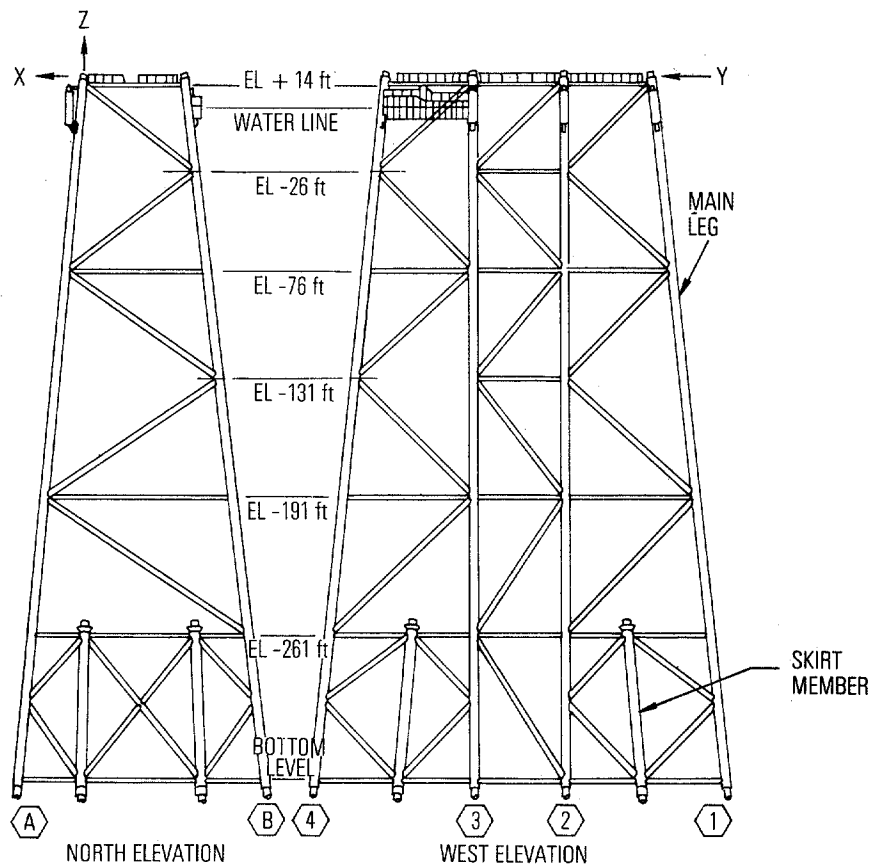


Figure 2-2. Base Section of SP-62C (Courtesy of Shell Oil Company)

response and sensitivity needs for this application. Seven accelerometers, six translational and one angular, were affixed to the main legs in several deployments, and from two to six hours of data were recorded on FM tape (8-channel) for each setup. Two ranges of bandpass filtering were employed: 0.03 to 5 Hz and 0.03 to 20 Hz. The various locations and orientations of the accelerometers are shown schematically in Figure 2-3 which depicts the 49 ft (15 m) level (lower deck), the 14 ft (4.3 m) level (boat landing level containing a peripheral walkway Figure 2-2), and the eight main legs. The accelerometers were actually located about 5 ft (1.5 m) above these two working levels. The legs are designated A1 through A4 and B1 through B4 as shown (Figure 2-2). The axis X is also called the broadside direction; Y, end-on; Z, vertical; and θ_z , torsional. A typical designation is $\ddot{X}(A1-14)$, denoting an X-directed acceleration on the A1 leg measured at the 14 ft (4.3 m) level. The fixtures employed to affix the accelerometers to a leg were only capable of correcting for about half the batter in an attempt to align with the X, Y, Z coordinate axes. Figure 2-3 shows the 17 locations employed. Two reference positions $\ddot{X}(A1-14)$ and $\ddot{Y}(A1-14)$ were common to all deployments so that all the data could be interrelated to develop mode shape parameters. In addition, during one deployment one translational accelerometer was moved to record X- and Y- directed accelerations adjacent to rotating machinery to sample their vibration signatures.

Data were taken over a three-day period. An identification of the data acquisition runs is given in Table A-1 of Appendix A. Rough seas were encountered during the first two days with visually estimated 15 to 18 ft ($4\frac{1}{2}$ to $5\frac{1}{2}$ m) waves. About 12 hours of data were collected during this period. Calm seas, with 2 to 3 ft ($\frac{1}{2}$ to 1 m) swells, followed and about 10 hours of data were recorded. Data were obtained under both conditions, permitting an evaluation of the linearity of structural response and of the relative quality of the modal determinations in the two sea states.

The recorded data were processed onshore by anti-alias filtering the demodulated signals, digitizing, and finally performing auto- and cross-spectral density analyses to develop frequency response relationships for coherent modal responses among pairs of records (7). An identification of the data analysis runs is given in Table A-2. The software program employed the Blackman-Tukey method of first determining correlation functions and then Fourier transforming to obtain spectra (13). The specifics of these analyses and the results will be discussed.

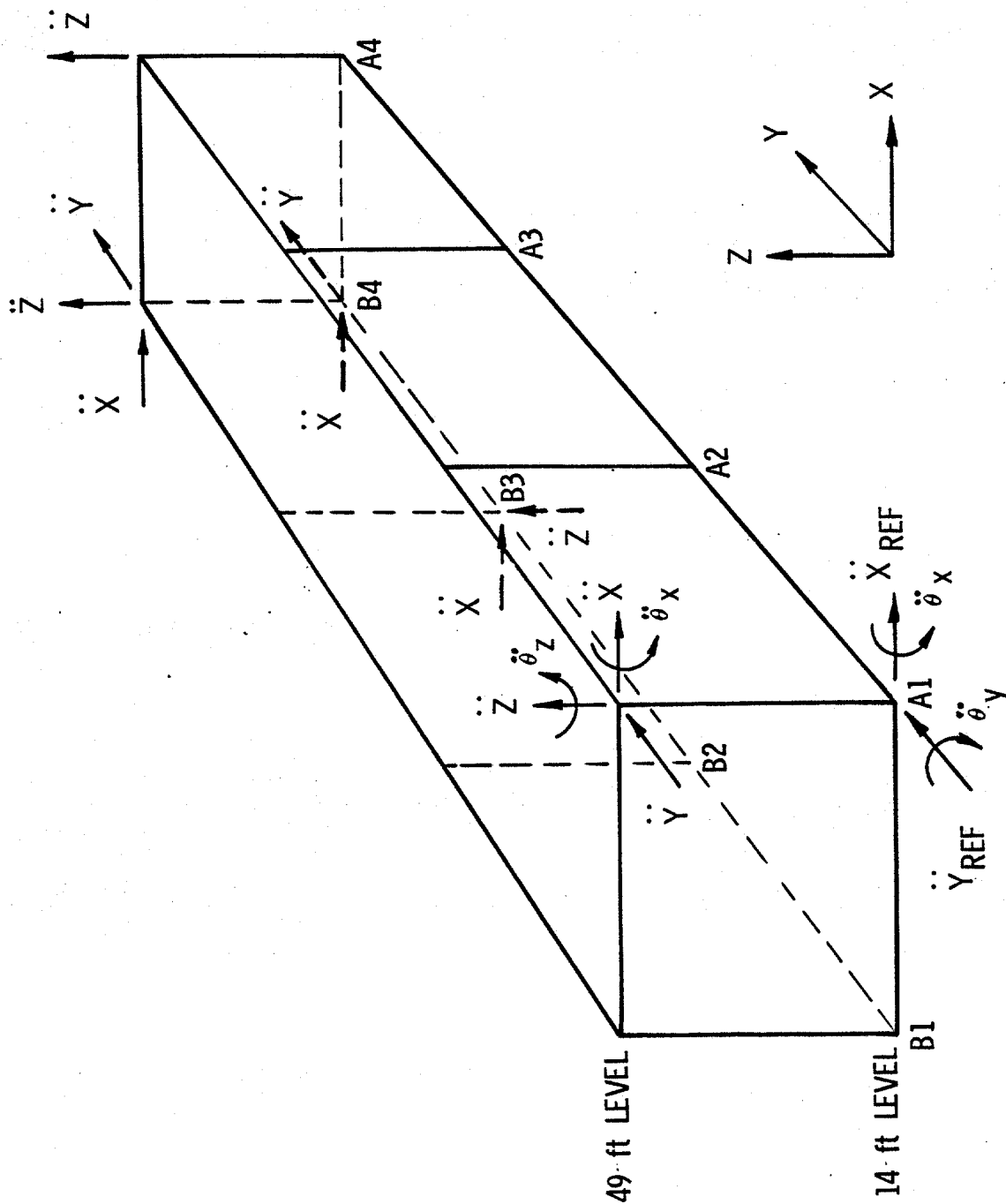


Figure 2-3. Accelerometer Locations

2.2 PERIODIC NOISE

Investigations were performed to identify machinery and tape recorder noise in order to avoid their misinterpretation as modal responses. Autospectra were computed for records obtained near the major machines: A diesel-powered generator operating continuously, a duty-cycled air compressor, and two pipeline pumps intermittently operated singly or together. Also, autospectra were computed simultaneously at selected leg positions to see the consequence of the machinery noise at monitoring locations. One such spectrum is shown in Figure 2-4 for data low-pass filtered to 20 Hz using a bandwidth $B = 0.06$ Hz and a bandwidth time product $BT=57.6$. Machinery-induced peaks (denoted by symbol "M") were identified at 5.12, 5.4, and 7.5 Hz and higher frequencies. Occasionally a peak at 2.7 Hz appears (not on Figure 2-4) apparently as a consequence of pipeline pump operation which usually only yields the 5.4 Hz and higher frequencies. The reason for the sporadic appearance of the 2.7 Hz is unknown, although a speculation is that it may result from operation of only one of the two pumps.

Selected autospectra were also obtained with and without operation of the pumps and compressor to address their contribution to broad band noise. Unfortunately this was not possible for the generator. It was established that operation of pumps and compressor did not noticeably increase the broad band noise below 5 Hz.

Tape recorder noise was identified by computing the autospectrum of the signal produced by the recorder in the absence of an applied input to the recorder (Figure 2-5). Of greatest significance was a periodic signal introduced by the capstan drive. The fundamental, labeled ① in Figure 2-5, was at 0.824 Hz at 41 dB down from full scale (0.9% full-scale amplitude); the first few harmonics labeled ②, ③, ④ in Figure 2-5, decreased in magnitude with higher frequency, reaching 48 dB down for the third harmonic at 3.30 Hz. These peaks were frequently seen in the data (denoted by symbol "R"; e.g., Figure 2-4). Lower level peaks were also observed in the recorder noise (see peaks labeled 1, 3, 5 in Figure 2-5). In a few instances, it is suspected that one of the lower level recorder noise peaks at 1.18 Hz, labeled 3, also encroached into spectra.

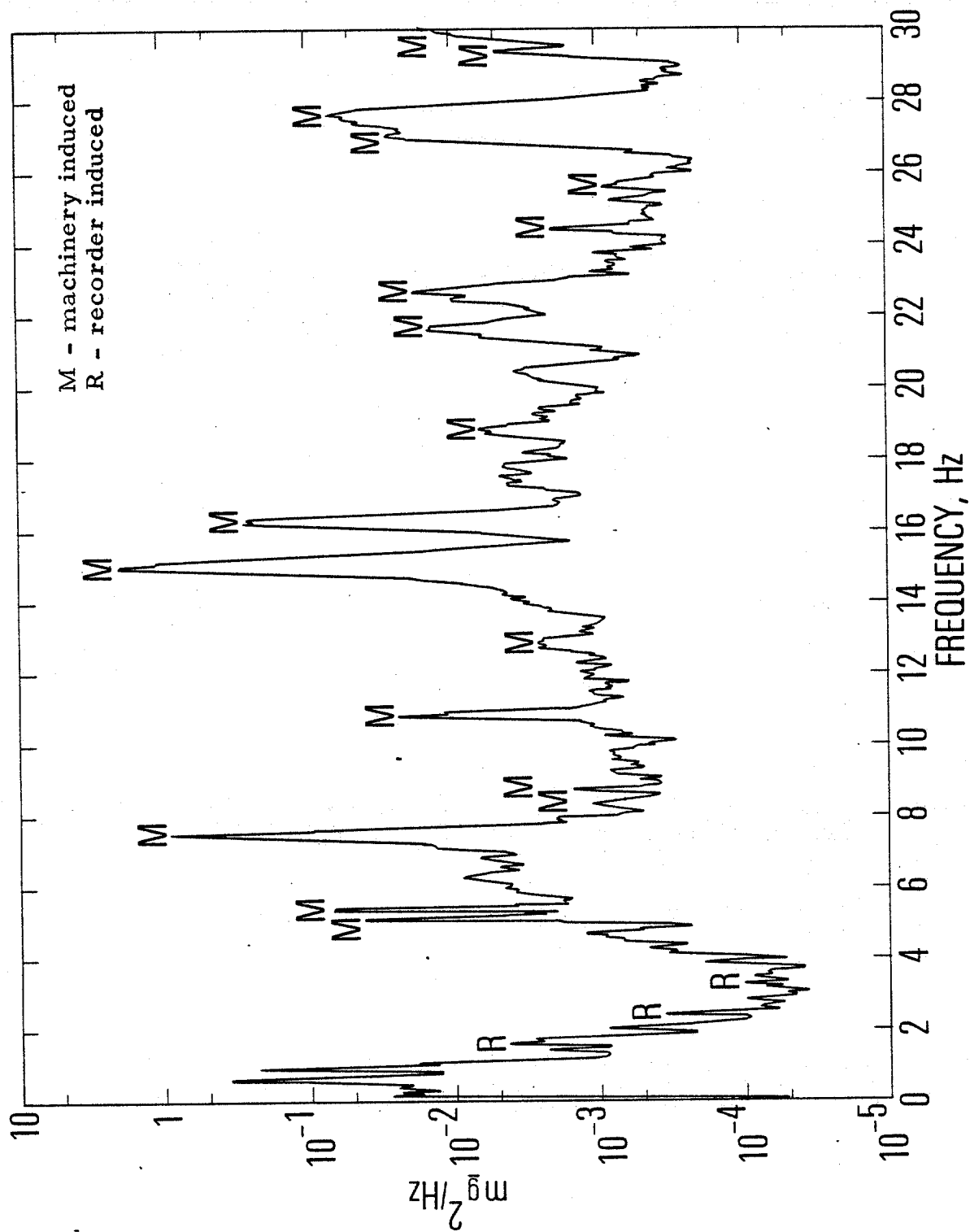


Figure 2-4. Autospectrum of $\ddot{X}(A1-14)$ for $B = 0.06$ Hz, $BT = 57.6$,
20 Hz Low-Pass Filter

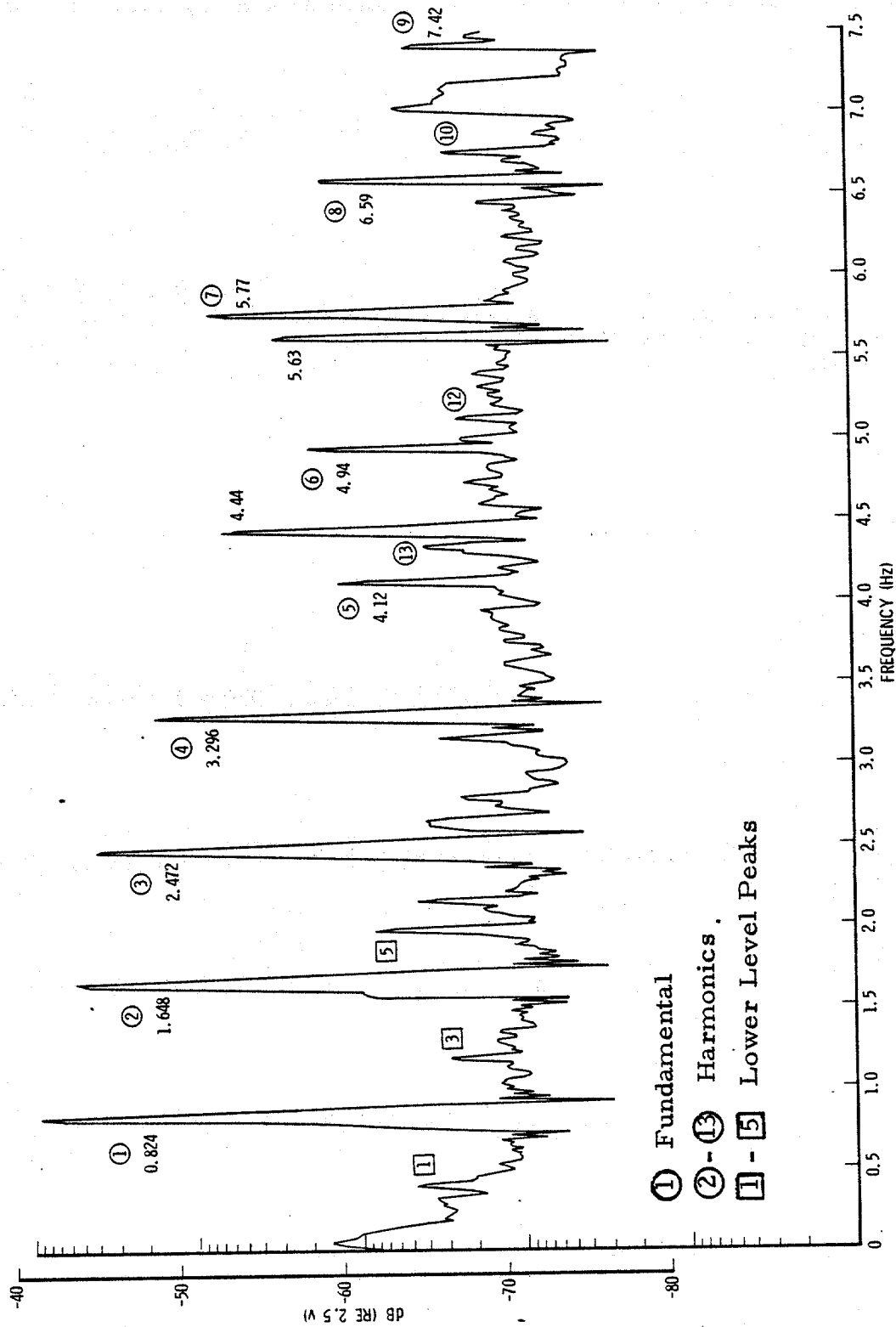


Figure 2-5. Tape Recorder Noise Peaks for $B=0.03$ Hz, $BT=28.8$

It is understood that such drive mechanism "noise" peaks are typical of analog tape recording and that this noise is generally the limiting factor for the recorder signal/noise ratio. The 0.824 Hz fundamental frequency is associated with the record speed of 15/16 ips and will increase in frequency in proportion to tape speed. Thus, this noise could be moved to above 5 Hz by speeding up the recording to 7½ ips. The penalty would be the use of much more tape.

2.3 MECHANIZATION OF SPECTRAL ANALYSIS

It was decided to direct detailed attention below 5 Hz, which was certain to encompass the three lowest frequency modes in lateral and torsional directions. The aim was to identify at least these nine modes (as suggested in Ref. 11). It was decided to convert all the data to a 15 samples per second (SPS) rate after appropriate anti-alias filtering. In a few test cases the sampling rate was converted further to five SPS.

Next, a few cross-spectra were calculated to examine the effect of alternative windows. A window tapers the data at the ends of a record to reduce leakage (i.e., increase side lobe attenuation for the digital filter), but does so at the expense of increased width of the main filter lobe (i.e., a loss in frequency resolution). Three cases were treated: no window, Hanning window, and a Hanning-twice window (Hanning function squared). The unwindowed spectra were totally unusable since large regions of frequency contained meaningless spectral results (specifically, negative autospectral values). The Hanning window all but eliminated such spurious results and both Hanning types appeared to yield comparable results in the regions of possible modes. The standard Hanning window was therefore selected for further use since the penalty in resolution was not as great as for the Hanning-twice window.

The raw bandwidth B and the BT product was explored next (T is the time duration of the total record analyzed). The range explored was B from 0.005 to 0.06 Hz and BT from 8 to 173. With a view toward achieving high quality, coupled with practicality in terms of computational costs and length of data recording, it was judged best to employ $B = 0.03$ Hz, $BT = 28.8$ ($T = 16$ min) for the bulk of the spectral analyses. In particular, neither $B = 0.015$, $BT = 28.8$ ($T = 32$ min) nor $B = 0.03$, $BT = 172.8$ ($T = 96$ min) led to general improvement in the signal/noise ratio of higher modes (i.e., as a whole, peaks did not stand out taller from the noise

background and coherences were not improved). It is interesting to note that about the same optimum bandwidth, $B = 0.025$ Hz, was arrived at for normal analysis on North Sea platforms (11).

2.4 FULL SYSTEM CALIBRATION

To enhance the accuracy of the extracted model shape, a method was evaluated to enable end-to-end calibration of the system. It involved the recording of all the translational accelerometers colocated so that the acceleration sensed by each is identical. The location employed was on the upper flange of a heavy deck beam member near the A1 leg on the lower deck. Data were recorded for about 20 min. These data were then processed to determine frequency response relationships of the complete path of the signal for each accelerometer relative to one path used as a reference. Each path involves: accelerometer, cable, signal conditioner channel, recorder tape channel, dub tape channel, discriminator/filter, and digitizer channel.

Highly coherent results were obtained with some deterioration at frequencies for which the signals were extremely weak (spectral shape is similar to that in Figure 2-4). A typical result is shown in Figure 2-6. Guided by the most coherent data, the phase characteristic has the character associated with a pure time difference (i.e., phase proportional to frequency). In the case shown, the time difference is 14 msec. It is judged that such a time difference can be estimated to within 1 msec, with the result that the uncertainty in phase calibration is negligible (less than 2 deg below 5 Hz). Similarly, the amplitude characteristic can be smoothed. At frequencies where modes exist and good mode shapes can be determined (discussed in the next section), the uncertainty in amplitude ratio is judged to be no more than 2%.

In our experiment, all the hardware elements from accelerometer through to each recorder channel were not kept in the same grouping during the various accelerometer deployments and recalibration for each grouping was not done. The relative calibration process, therefore, was not used to full advantage in our tests. It was shown, however, that the process is both practical and accurate. It is clear that this calibration method can be employed to enhance the accuracy of mode shape results.

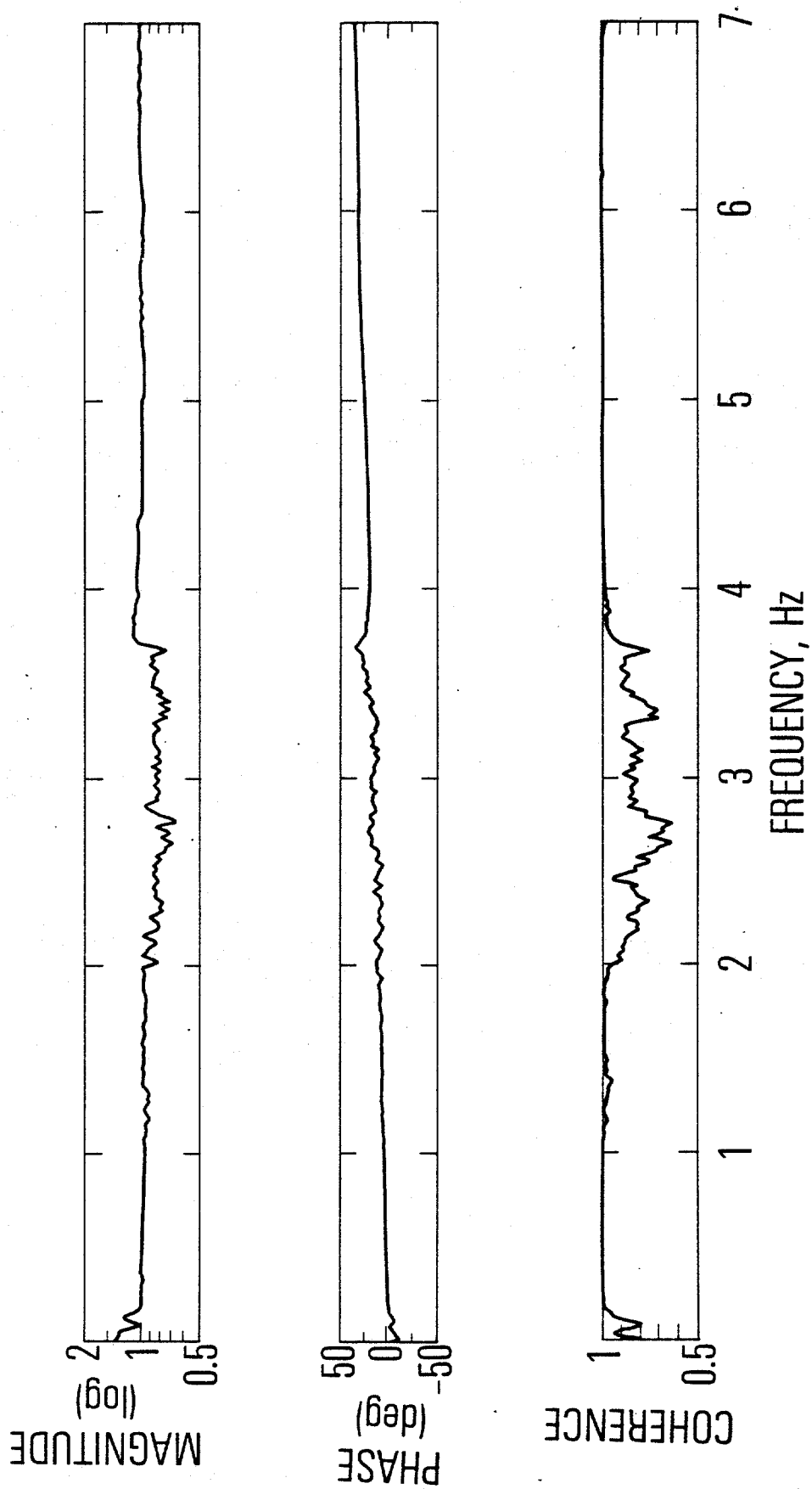


Figure 2-6. Typical Results for Relative Calibration of Two Signal Paths

A disadvantage in the use of angular accelerometers is that they do not lend themselves to simple calibration relative to the translational accelerometers.

2.5 DISCUSSION OF MODAL RESULTS

Autospectra for \ddot{X} (A1-14) and \ddot{Z} (A1-49) are shown below 5 Hz in Figures 2-7 and 2-8, respectively, for data acquired in the rough and calm seas. These are reasonably typical results for lateral and vertical measurements. An autospectrum of torsional acceleration, $\ddot{\theta}_z$ (A1-49), is shown in Figure 2-9 for a calm sea. (This measurement was not acquired for the rough sea.) A typical coherence is shown in Figure 2-10a for two lateral measurements in the same direction and in Figure 2-10b for a measurement in one lateral direction and one in the other. Recorder-induced peaks (R) and one machinery-induced peak (M) on Figure 2-8 are identified as previously discussed. Peaking appearing below 0.5 Hz is presumed to be due to basic periodicity in the waves and as a consequence of their spatial interaction with the structural members. This data would be sensitive to sea state and its directionality, and relatively insensitive to underwater structural failure. Consequently, these data are ignored for monitoring purposes.

The fundamental broadside (X) and torsion (θ_z) natural modes are responsible for the 0.646 Hz and 0.965 Hz peaks, respectively, in the calm sea spectra. Moreover, the fundamental end-on (Y) mode is identified from any end-on acceleration as being at 0.658 Hz. Slightly lower frequencies were observed in the rough sea and this will be discussed subsequently. Lateral accelerations in the fundamental modes ranged between 0.02 and 0.7 mg rms. It was quite simple to distinguish between the end-on and broadside fundamentals, even though separated by only 0.012 Hz, since they were so pure in their directionality. This was evidenced by the fact that coherence between any measurement in one direction with one in the other direction was very low, even though very strong peaks at seemingly the same frequency appeared in both autospectra (Figure 2-10). Evidence that no significant torsion was involved in either fundamental lateral mode is provided by the virtual absence of any evidence of a peak on the torsional autospectrum of Figure 2-9.

Mode shapes for the three fundamental modes were accurately determined from calculated frequency responses, yielding amplitude and phase relationships between pairs of measurements. Coherences between lateral motions were usually

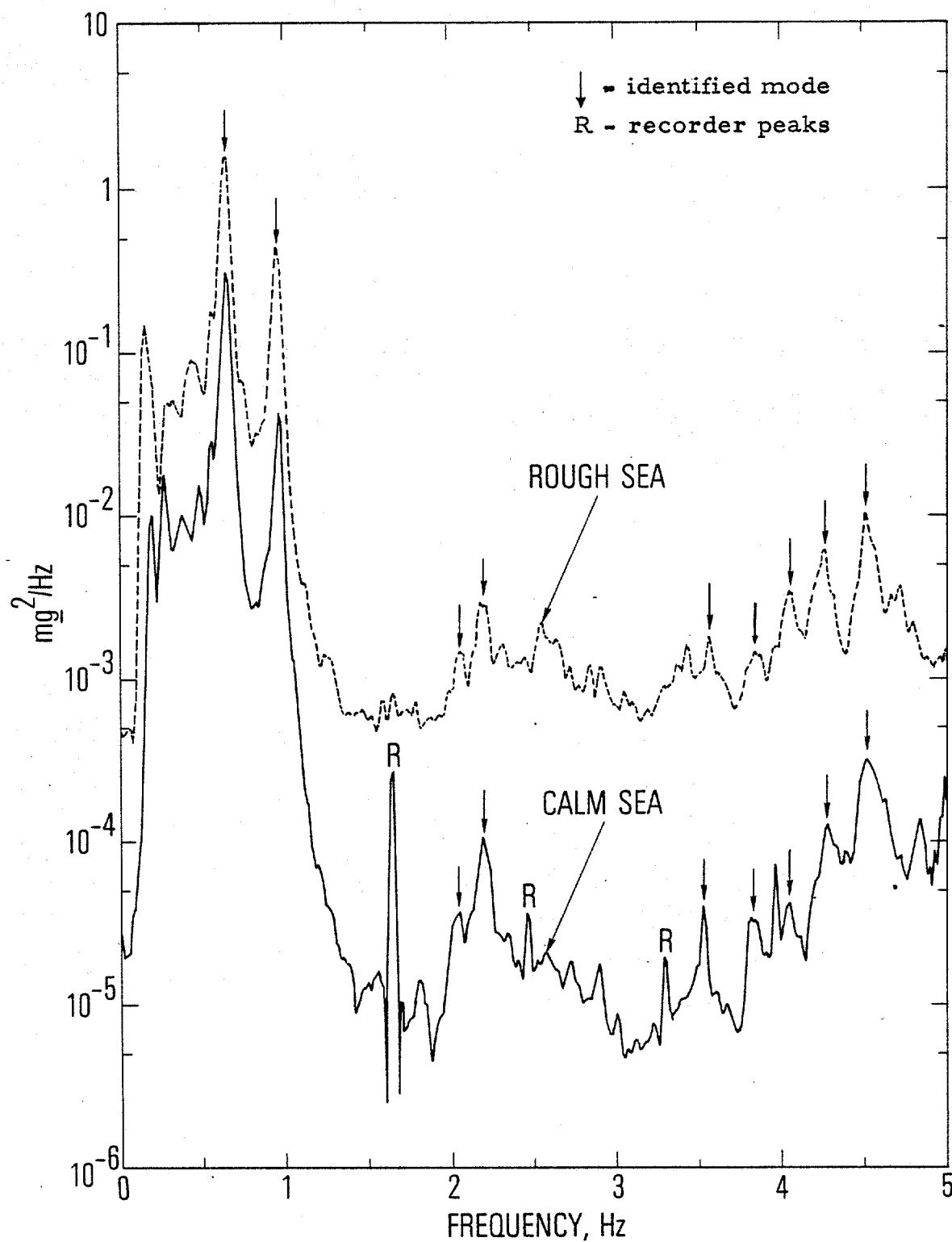


Figure 2-7. Autospectrum of $\ddot{X}(A1-14)$ for $B = 0.03$ Hz,
BT = 28.8

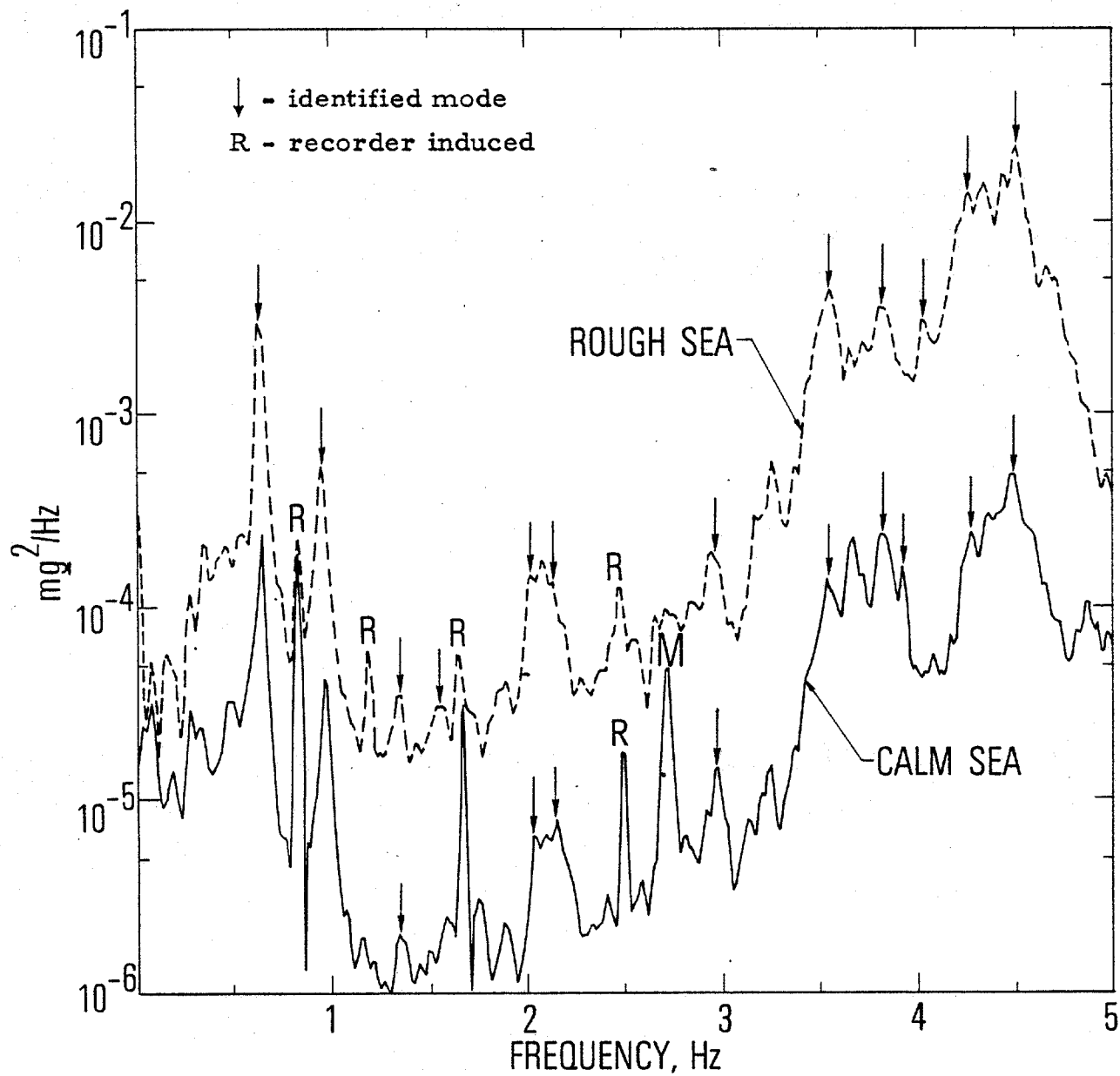


Figure 2 -8. Autospectrum of \ddot{Z} (A1-49) for $B = 0.03$ Hz,
BT = 28.8

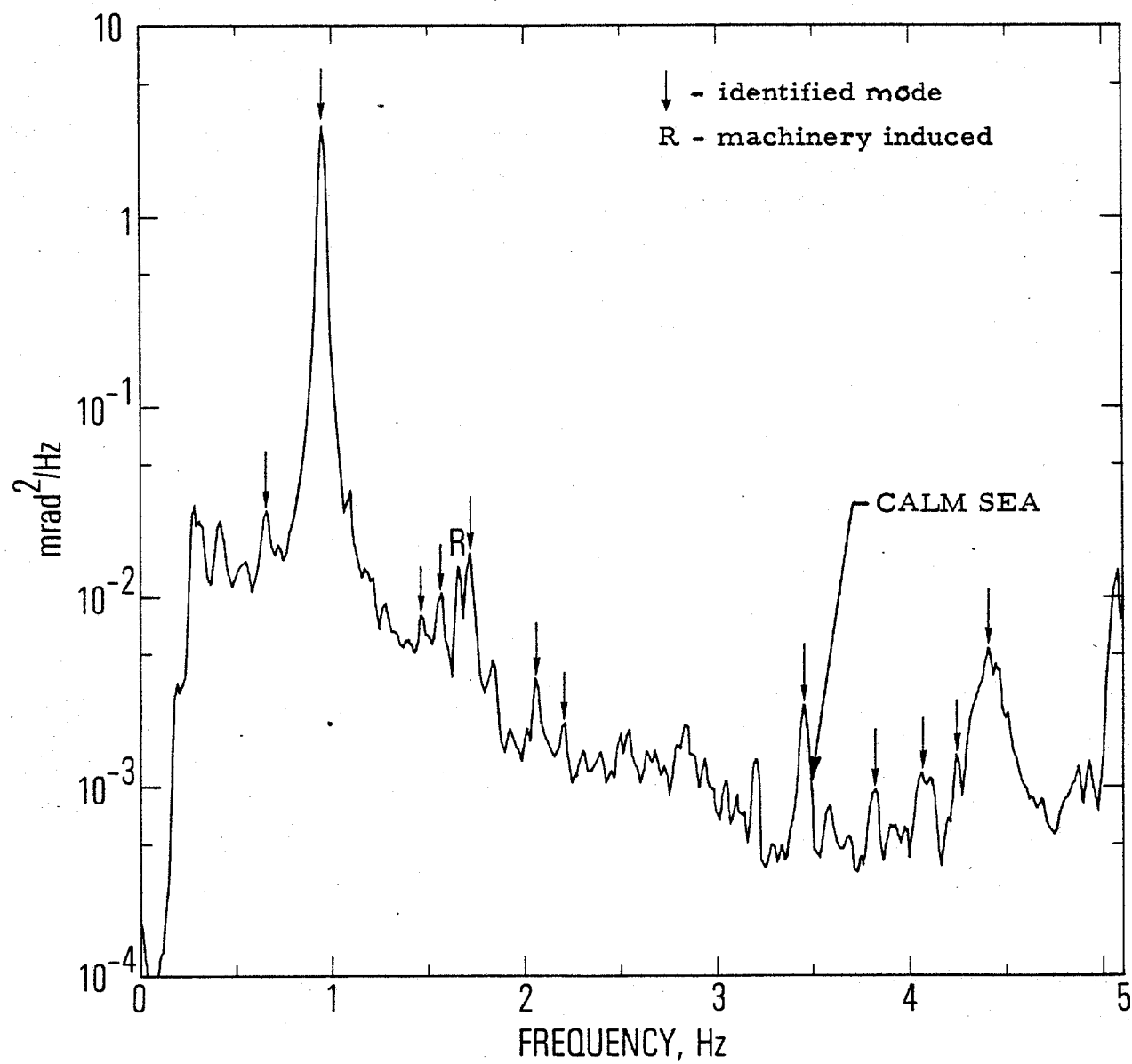


Figure 2-9. Autospectrum of $\ddot{\theta}_z$ (A1-49) for $B = 0.03$ Hz, $BT = 28.8$

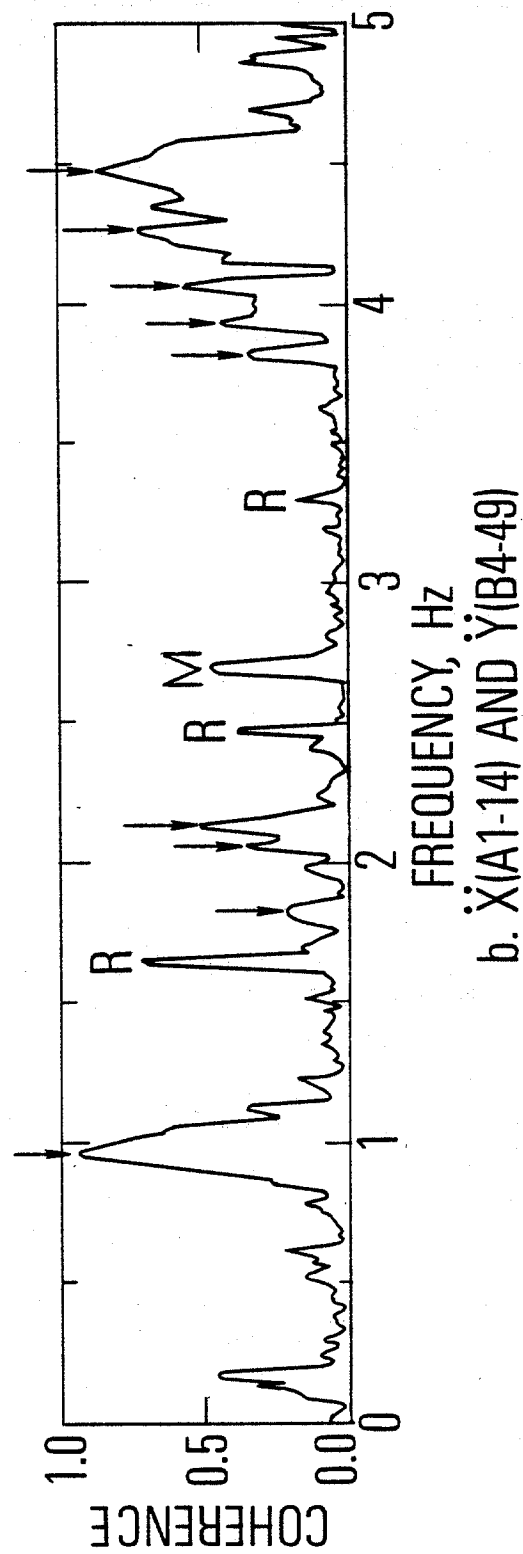
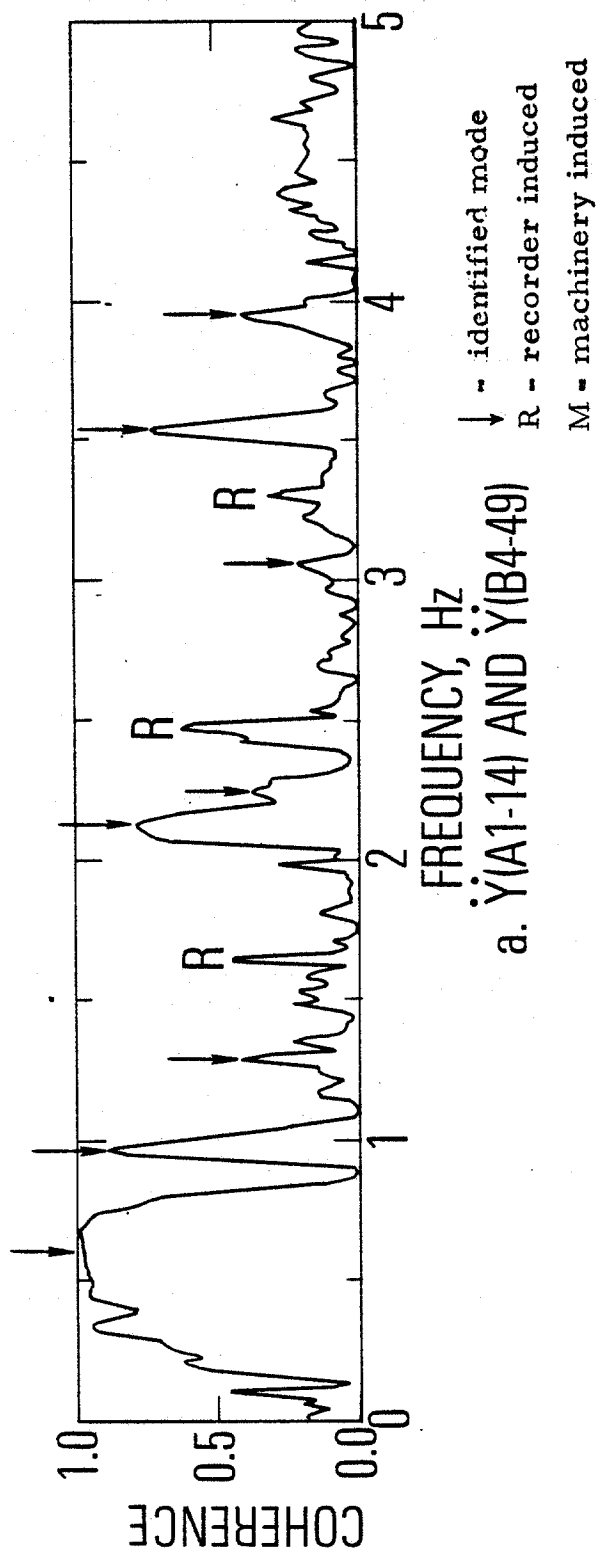


Figure 2-10. Typical Coherences for $B = 0.03$ Hz, $BT = 28.8$

at or above 0.95 (e.g., Figure 2-10). The shapes detected are shown in the upper row of Figure 2-11. Small vertical motions were also detected with amplitudes less than 10% of the maximum lateral amplitude, usually with coherence above 0.75. The accuracy of these motions is somewhat in doubt because the precise angular alignment of these accelerometers with the vertical was not measured. The angle is believed to be in the neighborhood of 3 deg, leading to about a 5% sensitivity to lateral acceleration. Cross-axis sensitivity of the accelerometers ($\leq 1.7\%$ for the accelerometers employed) is also a factor. More care must be taken in the future if it is deemed useful to detect vertical motions of the order of 10% or less of lateral motions.

The region between the fundamental mode peaks and 5 Hz contains evidence of a number of higher modes of the platform. Whereas the fundamental modes are relatively easy to measure, the higher modes are typically more difficult to measure because of poorer signal/noise ratio (Figures 2-7 through 10). Table 2-1 shows in a qualitative fashion the visually observed signal/noise (that is, how high the peak stands out above neighboring spectral values) for modes above the fundamental group for each of the measurement locations. The approach employed to identify higher modes was to look for (a) peaks having the same frequency at several measurement locations and constancy in frequency from one data run to another, (b) coherence in the relationship between measurements at those frequencies, and (c) phase relationships among the measurements that are characteristic of lightly damped natural modes (i.e., essentially in-phase or out-of-phase behavior except near nodal positions). Peaks identified as indicative of platform modes are denoted by arrows in Figures 2-7 through 10.

A summary of the modes identified from the data with comments is contained in Table 2-2. The first column presents the natural frequencies. The second column presents mode shape information in terms of deck center-of-gravity displacement, with the order qualitatively indicative of relative magnitude. The use of a minus sign indicates a negative sense for that displacement. For example, the 3.91 Hz mode has deck motion in order of magnitude (Figure 2-11): minus θ_z , plus Z, and plus X. Miscellaneous comments appear in the last column.

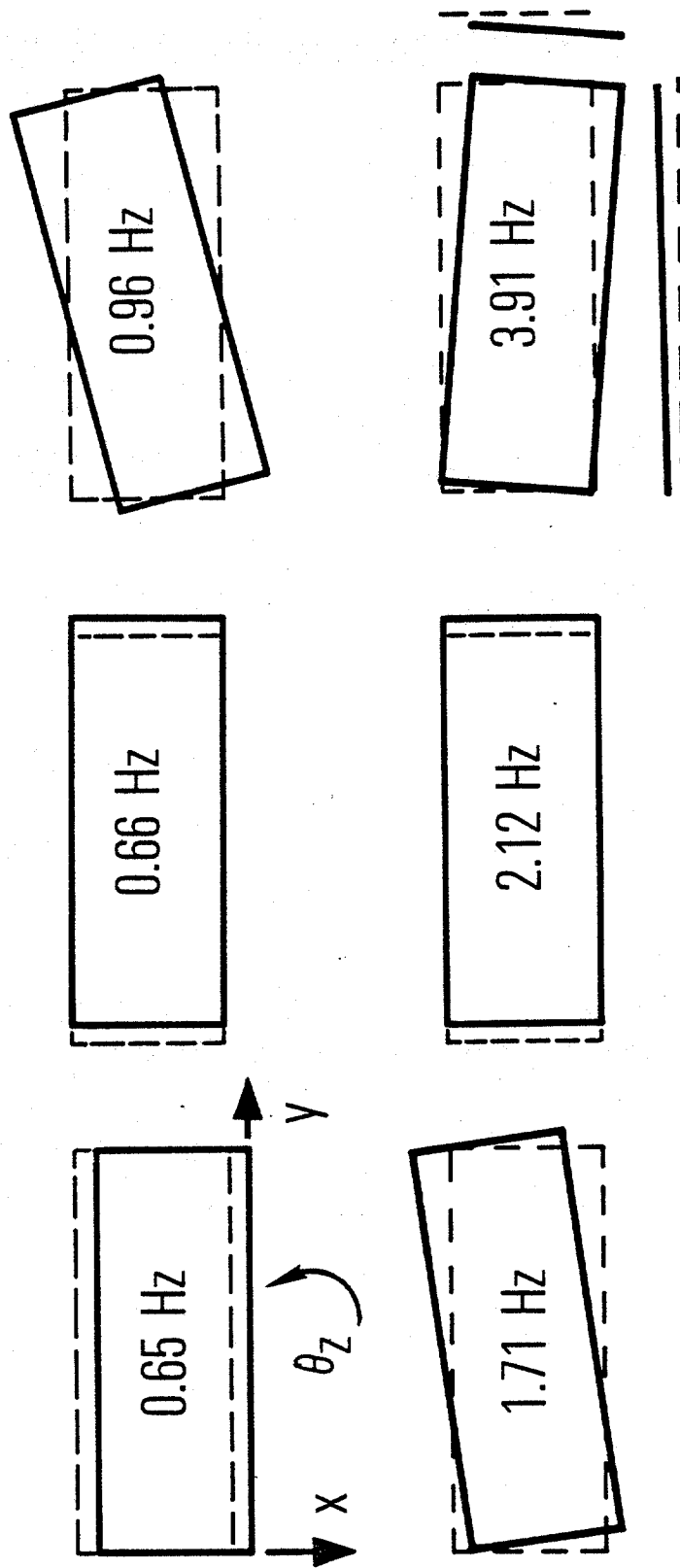


Figure 2-11. Experimentally Detected Deck Motion Shape for Well Identified Modes

Table 2-1. Observed Signal/Noise for Higher Modes¹

FREQUENCY MEASUREMENT	Signal/Noise Ratio															
	1.28	1.35	1.47	1.54	1.71	2.04	2.12	2.21	2.62	2.94	3.01	3.05	3.44	3.50	3.81	4.91
$\bar{X}(A1-49)$	●		●	●	●	●	●	●								●
$\bar{X}(B6-49)$			●	●	●	●	●	●								●
$\bar{X}(A1-14)$			●	●	●	●	●	●								●
$\bar{X}(B3-14)$			●	●	●	●	●	●								●
$\bar{X}(B6-14)$			●	●	●	●	●	●								●
$\bar{Y}(A1-49)$	●		●	●	●	●	●	●								●
$\bar{Y}(B6-49)$	●		●	●	●	●	●	●								●
$\bar{Y}(A1-14)$	●		●	●	●	●	●	●								●
$\bar{Y}(B6-14)$	●		●	●	●	●	●	●								●
$\bar{Z}(A1-49)$		●														
$\bar{Z}(A6-49)$		●														
$\bar{Z}(B6-49)$		●														
$\bar{Z}(B3-14)$		●														
$\bar{\theta}_2(A1-49)$				●												
$\bar{\theta}_2(A1-49)$				●												
$\bar{\theta}_2(A1-14)$				●												
$\bar{\theta}_2(A1-14)$				●												

1 ● high, ● moderate, ● low signal/noise ratio

Table 2-2. Summary of Mode Identification from
Field Data on SP-62C (October 1977)

Frequency, Hz	Shape	Comments
<u>0.646</u> (± 0.005)	X	Fundamental mode group Dominant modal responses Frequencies slightly lower in rough sea
<u>0.658</u> (± 0.005)	Y	
<u>0.965</u> (± 0.005)	θ_z	
<u>1.28</u> (± 0.02)	Y, θ_z , -X	Weakly excited
1.35		Tentatively a mode
1.47	Y, θ_z	1.47 weaker but evidences similar shape
<u>1.54</u> (± 0.03)		
<u>1.71</u> (± 0.02)	θ_z , Y, -X	Mostly second torsion
2.04	Mostly θ_z	Shape uncertain; weakly excited
<u>2.12</u> (± 0.02)	Y	Probably third end-on
2.21		Weakly excited
2.62		Weakly excited; seen in X and Y at B4-14
2.94, 3.01		Most clearly seen vertically
3.05		Seen on Y at A1-14 and B4-14
3.44		May be paired with 3.50 Hz
<u>3.50</u> (± 0.02)	Y, Z, -X, θ_z	Clear Z at A4 and B4
<u>3.81</u> (± 0.02)	Z, Y, θ_z	Predominantly first vertical
<u>3.91</u> (± 0.02)	- θ_z , Z, X	Deck rotates about A1
<u>4.06</u> (± 0.04)	Z, Y, -X, θ_z	Highly coupled
4.23, 4.3, 4.4, 4.5		High broad band response made discernment difficult

The first three frequencies in Table 2-2 (first mode group) are doubly underlined to indicate high accuracy (estimated to be ± 0.005 Hz), with very well identified mode shapes with ratios of lateral deflections estimated to be accurate generally within 10% (top row of Figure 2-11). The frequencies were estimated by hand plotting the spectral points (calculated every 0.015 Hz) and graphically interpolating to find the maximum. The double underline is also used for the 1.71 Hz second torsion, the 2.12 Hz third end-on, and the highly coupled 3.91 Hz mode to denote accurate frequencies and mode shapes, although not quite as accurate as for the fundamentals (lower row of Figure 2-11). Estimated accuracies are ± 0.02 Hz and 20% on modal ratios. The single underline of modal frequencies indicates that a consistent mode shape was determined, although with questionable accuracy. The frequency inaccuracy for this group is estimated to be ± 0.02 to ± 0.04 Hz and the mode shapes are qualitative. Note that the 3.81 Hz predominantly first vertical mode is in this group, and that the neighboring modes (from 3.50 to 4.06 Hz) have important vertical involvement. Finally, a lack of an underline indicates that mode shape was not determined because of insufficient or inconsistent data. The frequency accuracy, however, is believed to be between ± 0.05 to ± 0.1 Hz.

The ranking of the relative utility of the various modes for failure detection requires use of the results of the mathematical model studies. In terms of experimental detectability, the doubly underlined modes are the strongest candidates. Interestingly, simple broadside and end-on second modes are absent from this group. Insofar as the end-on direction goes, we see at least three or possibly four modes between the first and second torsion, at least three of which involve end-on and torsion coupling. The possibility of jacket stiffness or deck mass coupling as the cause seems remote in view of the fact that the first and third end-on modes are quite pure in form. It seems more likely that one or more substructures supported off the decks have a resonance in this range and provide a mechanism for end-on/torsion coupling. It would appear dangerous to rely on these modes for monitoring purposes without knowing the mechanism for the coupling and how variable that mechanism might be. For example, if a fluid tank is involved, a change in the amount of fluid contained could lead to a change to these coupled modes which might then be misinterpreted as due to a structural failure. Moreover, a consequence of such mode splitting is that the responsiveness of each mode is diminished from that which would exist in the absence of splitting. That may well be

the reason why a second end-on mode is not among the stronger of those detected. Typically this seems not to have been the case in the North Sea studies (6).

The absence of a second broadside mode was a mystery until it was learned that a 1.65 Hz second broadside mode was identified for SP-62C during shaker testing subsequent to our experimental work (17). This is exactly the frequency of the second component of the tape recorder discrete noise discussed earlier (Figures 2-7 and 8). This noise in many cases masked the appearance of this mode, and perhaps, in some instances, real modal response was misconstrued as being recorder noise.

Some further observations from the spectral studies follow:

1. As a whole, the ability to detect modes was as good in a calm sea as in a rough sea. That is, the signal/noise ratio for the modal peaks, and corresponding coherences between measurements, were generally comparable for the two sea states.
2. The only nonlinear behavior positively detected was about a 1% downward shift in fundamental lateral natural frequencies, and a 2% downward shift in the fundamental torsion natural frequency, from the calm to the rough sea. No evidence was seen of spurious peaks or "split" peaks (two close peaks stemming from a single mode) as has been reported from North Sea studies, particularly in the region of fundamental modes (5, 11). The cause is stated to be uncertain, but the candidate explanation given is nonlinear interaction owing to indeterminate connection between pile and jacket when grouting is absent or incomplete. As mentioned earlier (Section 2.1), SP-62C has ungrouted main piles, so it would appear to be susceptible to such nonlinearity. Of course it is not known whether such effects would appear in a rougher sea than experienced during the present data acquisition.
3. The greatest dynamic range is required for data acquisition in a calm sea. A clear indication of this is seen in Figures 2-7 and 8 where recorder peaks stand out much more clearly for the calm sea. The recorder peak at 1.65 Hz is a particular standout. It is judged that this peak should be diminished by at least 25 dB to remove it as a significant contaminant of the spectra. This

peak is known to be 43 dB down from full scale. Thus, for the present application, the dynamic range for the recording should ideally have been about 70 dB relative to periodic noise. To come close to achieving this dynamic range with analog recording, it would require: (a) a recording speed high enough to keep periodic noise above the frequency range of interest and (b) filtering to reduce the dynamic range of the signals to be recorded (i.e., pre-whitening.). Such a range can be achieved readily, however, by digital recording of the data.

2.6 FORCED VIBRATION TESTING COMPARISON

In June 1978 platform SP-62C was subjected to forced shaking using a pair of electro-hydraulic actuators to force main legs of the 49 ft deck in horizontal directions (17). Each actuator was connected to a suspended 3000 lb reaction weight (1360 kg mass). Swept sinusoidal tests were conducted using force levels up to 8 kips (36 kN) peak-to-peak total from both actuators, with a slow sweep rate of 0.001 Hz/sec. The two actuators were positioned variously to excite purely in end-on, broadside and torsion directions. Two force-balance accelerometers were located on the A1 leg between decks. Resonances were found by monitoring response amplitude and the phase lag between response and force.

Unfortunately, since only two accelerometers were recorded, it is not possible to make a detailed comparison of frequencies and mode shape parameters with those determined from the ambient testing reported herein. Using the directional information from Reference 17, Table 2-3 contains a tentative comparison of frequencies determined from the forced testing with corresponding ones reported here from the ambient testing. The underlining employed for the ambient frequencies is the same as that used in Table 2-2.

There is no question about the correspondence for the fundamental mode group, the second torsion, and the third end-on. The frequencies listed for the ambient fundamentals are those found in the rough sea; as mentioned previously, these are slightly lower than those found in the calm sea (see Table 2-2). It is not known what additional nonlinear effect may result from the fact that the forced response amplitudes were up to several times larger than the rms ambient responses reached

Table 2-3. Tentative Comparison with Frequencies Determined from Forced Vibration Test (17)

Mode Group	End-on ¹ Forcing	Ambient	Broadside ¹ Forcing	Ambient	Torsion ¹ Forcing	Ambient	Other ² Ambient
Fundamental ³	0.648	0.65	0.642	0.64	0.96	0.95	
Second	1.31, 1.47	1.28, 1.47, 1.54	1.65	⁴	1.72	1.71	1.35
Third	2.15	2.12	(2.6)	2.62	(2.15)	2.04	2.21
Higher	(3.0)	3.05					2.94, 3.01
	3.4	3.44, 3.50					
	(3.9)	3.91					3.81
	4.1	4.06					4.23
							4.3
							4.4
							4.5

¹ Parentheses around frequencies in "forcing" columns indicate a lack of certainty that a mode exists.

² Alignment only by frequency; association to mode groups not implied.

³ Fundamental frequencies from ambient testing are those from the rough sea.

⁴ Masked by recorder noise.

in the rough sea. Moreover, modes above the fundamentals were excited to much higher levels in the forced testing and any nonlinear effect is unknown. Also, difference in deck loading between the two test programs is unknown. Assuming that these nonlinear and deck loading effects are relatively small, the comparison of frequencies for these cases is extremely satisfying.

The remaining comparisons are more or less speculative. Interestingly, of the modes determined from the ambient with at least qualitative shape, only the 3.81 Hz predominantly first vertical does not match a frequency established in the forcing tests. This is, of course, quite reasonable since this mode would tend to be weakly excited in terms of sensed lateral motion due to lateral forcing. All in all, the comparison is most encouraging, lending support to the contention that some modes above the fundamentals can be identified reliably from ambient vibration.

2.7. SUMMARY

Accelerations at 17 locations above water were detected in lateral, vertical, and angular senses using force-balance type transducers, with recording on FM analog tape. Data acquired in both rough and calm sea states provided equally useful data for detecting the lower modes of platform vibration. In the frequency range from 0.65 to 4.5 Hz, a total of 24 modes were detected as to their frequency. Accurate mode shape parameters were identified for six of these frequencies (Figure 2-11) and qualitative shape parameters for an additional five (singly underlined in Table 2-2).

Digital auto- and cross-spectral density analyses were performed. Optimum parameters were determined to be: 16 min of recorded data, a 0.03 Hz raw bandwidth, and a Hanning window. After elimination of discrete noise, spectral peaks indicative of modes were identified by analyst judgment. The criteria were consistency of appearance at various positions and times, relatively high coherences, and phase relationships appropriate for lightly damped normal modes. Mode shape parameters were estimated from calculated frequency response relationships among pairs of measurements.

A summary of the modes found appears in Table 2-2. The first mode group (fundamental in broadside, end-on, and torsion directions) dominated the ambient response. By interpolating the spectral data, their natural frequencies

could be detected to within 0.005 Hz; ratios of lateral motions could be determined to within 10%. The natural frequencies were detectably lower, by about 1% for the laterals and 2% for torsion, in the rough sea than in the calm sea. Even though the two lateral modes were only 0.01 Hz apart, there was no detectable cross-coupling between the two coordinate directions. Vertical motion less than 10% of the magnitude of peak lateral motion was clearly indicated, but its amplitude accuracy is in doubt due primarily to uncertainty in instrument alignment. Frequency comparison with the fundamentals determined from the subsequent forcing tests in Reference 17 is excellent.

Of the second mode group, only the second torsion was accurately identified. The second broadside was masked by a coincident noise peak from the tape recorder. The second end-on mode was split into three or four relatively weak modes, and a mode shape could be identified for only two of them. Of the third mode group, only the end-on could be well identified. Of the still higher modes, shapes could be identified only for a group of four modes between 3.50 and 4.06 Hz, all of which exhibited strong vertical motion. One of these (3.91 Hz) was about as accurately identified as the second torsion and third end-on modes. Vertical accelerometers were particularly useful for this higher mode group.

The comparison in Table 2-3 of frequencies of modes above the fundamentals with those determined by the forcing tests of Reference 17 is quite encouraging. The comparison is partially clouded by the inability to compare mode shapes and so some of the correlation in Table 2-3 is speculative.

The force-balance accelerometers employed were well suited to the needs for frequency response and sensitivity. Vertically oriented accelerometers provided good quality data and have the potential for being useful for monitoring. The angular accelerometer provided good information, but the modal data extracted could have been obtained in its absence. A clear disadvantage of the angular accelerometer is the inapplicability of the simple and highly accurate in situ calibration process possible for translational accelerometers.

Periodic noise from onboard machinery effectively limited the frequency range for detection to below 5 Hz. Broad-band noise below 5 Hz did not appear to have been influenced by the machinery operation. Below 5 Hz, tape recorder-induced periodic noise clearly appeared in the data, and occasionally one component

of equipment noise also appeared. This discrete noise has the potential of masking modal responses, and in the case of the second broadside mode this did happen. Future work to detect modes above the fundamental group should strive for at least 70 dB of dynamic range with regard to periodic noise within the instrumentation system. This could well lead to digital recording of the data. Analog recording preceded by adequate prewhitening (that is, data filtering to reduce dynamic range) is an alternative approach.

3. MATHEMATICAL MODEL OF PLATFORM

3. MATHEMATICAL MODEL OF PLATFORM

3.1 APPROACH

The structural dynamic model developed for the present study is based upon (a) a Shell Oil Company developed finite-element structural dynamic mathematical model used for design, (b) detailed structural drawings of platform decks, (c) detailed structural and equipment mass data and (d) additional detailed information - all obtained from Mr. J. A. Ruhl of the Shell Development Company. The primary goal of this task is to develop a mathematical model for the damage sensitivity studies described in the next section. Primary emphasis is for accurate representation of the first three groups of lateral and torsional modes and the fundamental axial mode as judged by comparisons to the experimentally determined modes. The approach is to begin by refining the Shell Oil Company supplied finite-element model which was developed to characterize the fundamental lateral and torsional mode group only. The extensions consist of a more detailed model of the deck structures and more refined virtual fluid mass matrix for flooded and submerged members. Once the extended model was complete and its vibration modes calculated, a number of adjustments are made to improve correspondence with the experimentally observed modes.

Formulation of the mathematical model was performed principally with the NASTRAN program which exploits sparsity, as well as bandedness of matrix descriptions for computational efficiency. The virtual fluid mass matrix was computed with a specially developed FORTRAN program.

3.2 JACKET/PILE/CONDUCTOR MODEL

The supplied structural dynamic model consists of an assembly of beam elements representing the jacket members, piles, conductors and a greatly simplified deck idealization. A perspective computer plot of this jacket/pile/conductor model (decks absent) is shown in Figure 3-1. Translational and rotational springs are connected to each pile at the mudline to represent equivalent soil stiffness contributions other than for pile axial behavior. The buried pile axial stiffness is represented by an axial member extending 100 feet (30.5 m) below the mudline and constrained to zero displacement at the lower node. (The actual piles extend

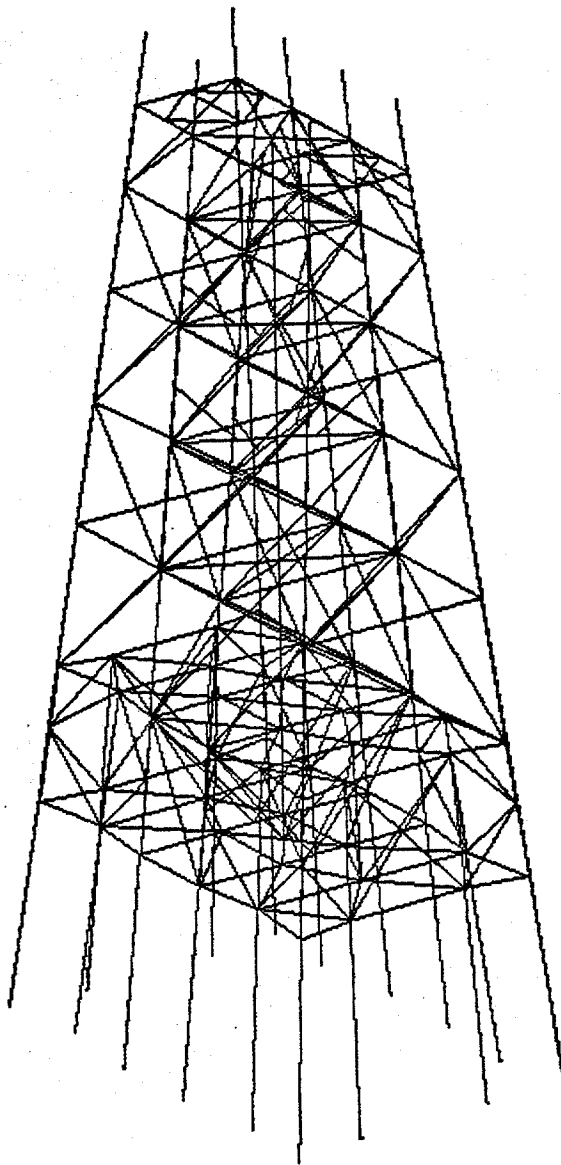


Figure 3-1. Jacket/Pile/Conductor
Model Configuration

150 feet (45.7 m) into the mud.) Fictitious cross-sectional properties are used for the below mudline pile sections to account for soil stiffness contributions to axial stiffness. It was judged necessary to modify the supplied model in the representation of the deck structure and in the fluid virtual mass to extend its applicability to higher modes.

The supplied jacket/pile/conductor model was expressed in terms of 213 structural nodes each having 6 degrees of freedom (dof) for a total of 1314 dof. Member connectivity of the main piles and jacket, welded together 14 ft (4.3 m) above the waterline, causes the stiffness matrix to be sparse but not banded. It was therefore decided, for computational economy, to perform the model assembly and analysis in NASTRAN which exploits the sparsity property. This was a change from the original intention to employ SAP IV which cannot as efficiently handle a nonbanded stiffness matrix.

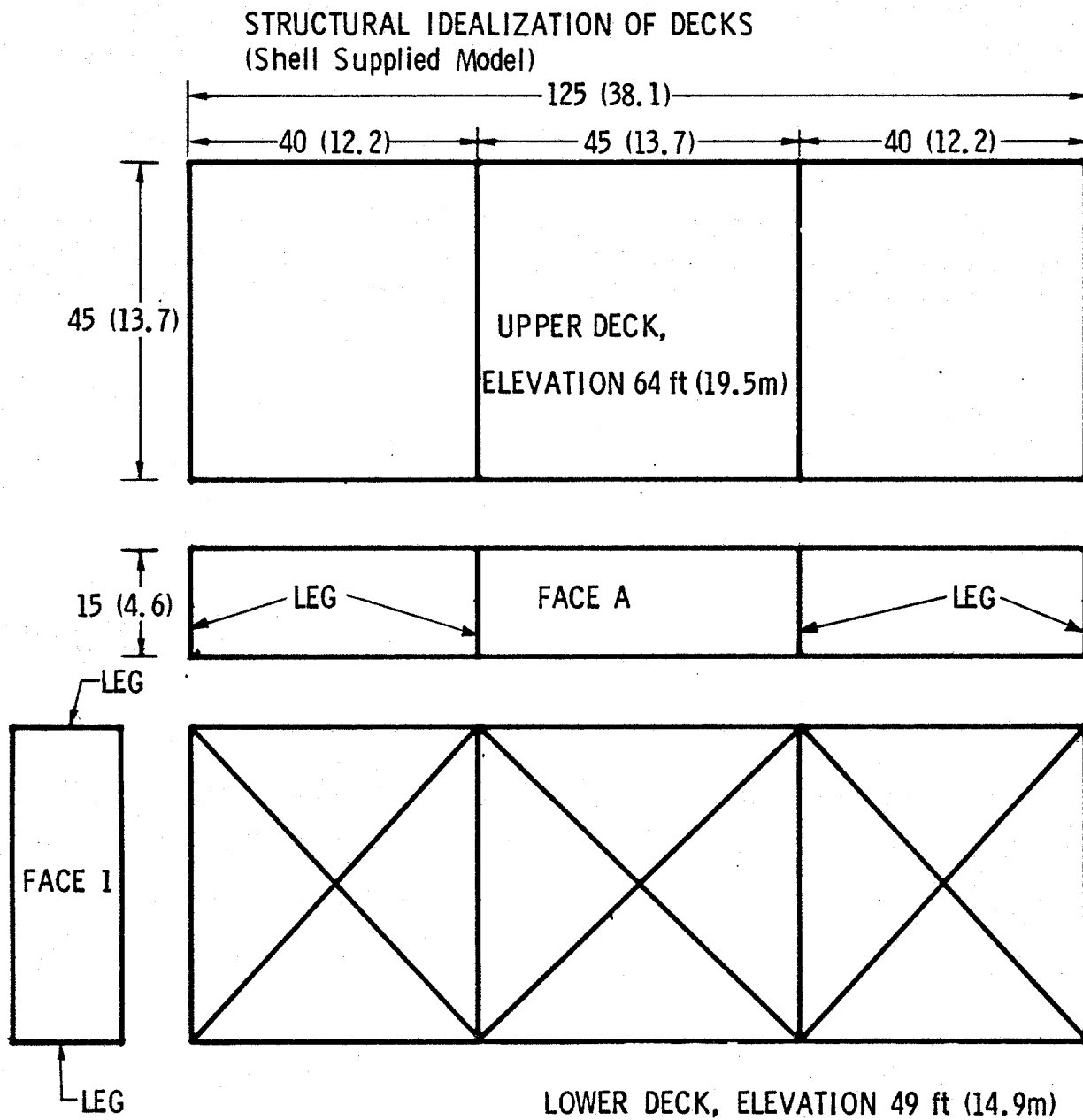
3.3 DECK MODEL

Aspects of the decks which are modeled include structural stiffness, mass distribution, and large tank fluid slosh effects. Some consideration is given to flexible tank modes, but these are not included in the model; it was determined that such modes could be important for behavior above 3 Hz.

3.3.1 Stiffness Model

The supplied structural idealization above the 14 ft (4.3 m) level consists of eight main vertical legs connected to simplified floor models as illustrated in Figure 3-2. The cross-sectional properties of the between deck main leg members do not account for the stiffness of the neglected interdeck truss members shown in Figure 3-3. The significance of truss stiffness in lateral shear was assessed in a simplified strain energy calculation for a single face subjected to horizontal loading. This truss stiffness was found to be more than twice the stiffness contributed by the main legs. The new structural model, therefore, must include a truss representation.

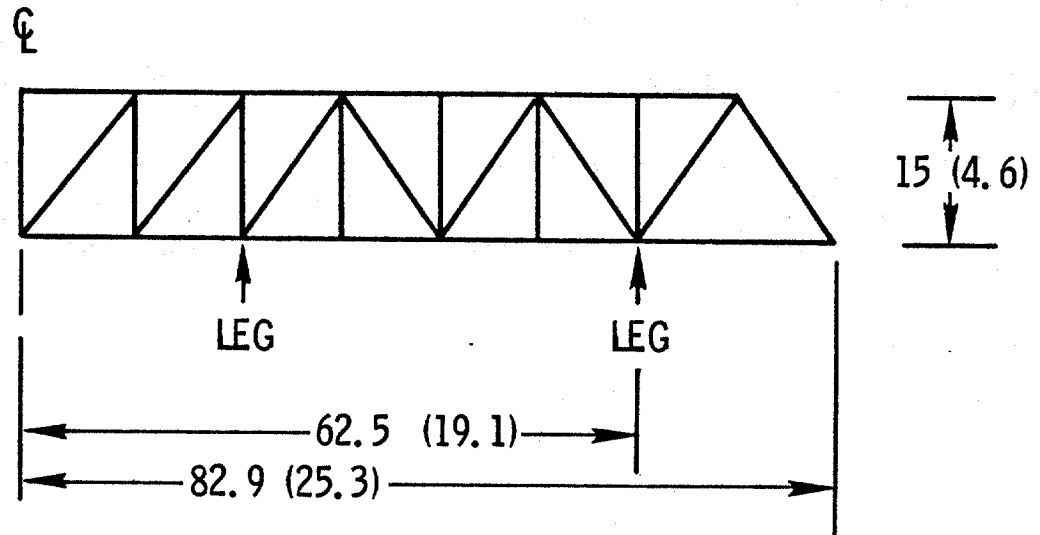
Complexity of the deck flooring rendered a detailed model impractical for the purposes of the present study. A rough estimate of flooring vertical stiffness was, therefore, used to size equivalent cross-member flexural inertias. Axial stiffness of the actual cross-members was employed to provide deck in-plane shear



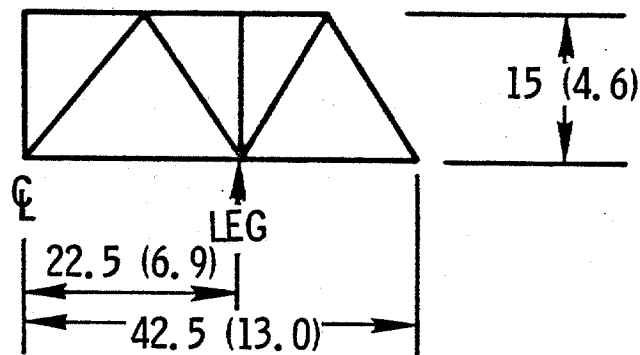
NOTE: Dimensions Shown in ft (m)

Figure 3-2. Structural Idealization of Decks

FACE A&B VERTICAL TRUSSWORK



ROW 1-4 VERTICAL TRUSSWORK CONFIGURATION



NOTE: Dimensions Shown in ft (m)

Figure 3-3. Interdeck Trusswork Member Configurations

stiffness. (In the parameter study described in the next section these axial stiffnesses are increased to preclude unrealistic in-plane distortions of the decks.) To enable a more accurate accounting of deck mass distribution, additional overhang members were included in the deck model. The overhang members were made sufficiently stiff to prevent unrealistic local overhang modes.

A finite element deck model accounting for the above discussed truss and floor details was formulated with 99 nodes (594 dof). The member network for floors is illustrated in Figure 3-4; truss members are illustrated in Figure 3-3.

3.3.2 Deck Mass Distribution

The overall weight of the decks above the 49 ft (14.9 m) level including structure, equipment and fluids was estimated to be 4192 kip (1901 Mg). The breakdown is as follows:

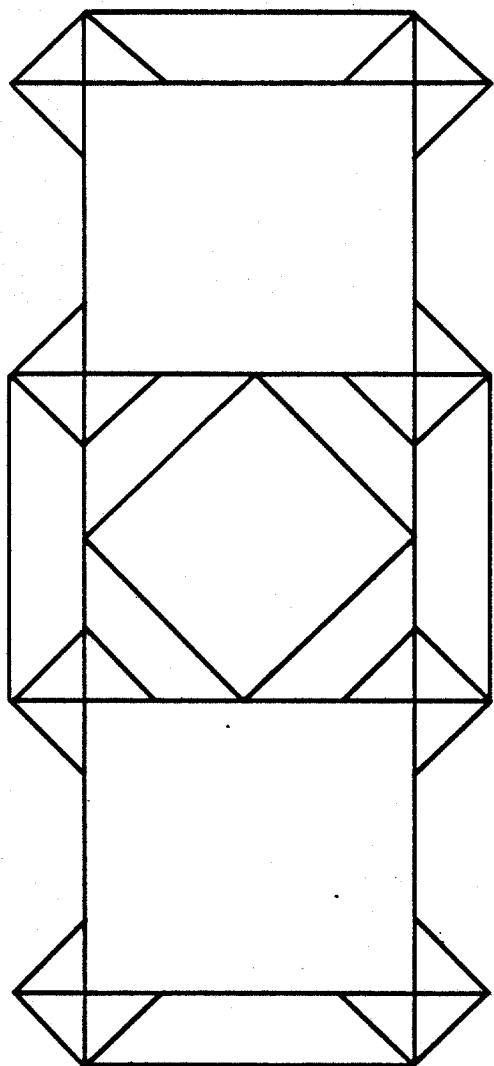
structure	1000 kip (454 Mg)
dry equipment	1903 kip (863 Mg)
fluids	1289 kip (585 Mg)

The finite element model described in Section 3.3.1 accounts for 270 (123 Mg) and 221 kip (100 Mg) for the lower and upper decks, respectively. Lumped masses of 49.1 kip (22.3 Mg) and 14.5 kip (6.6 Mg) were added to each of the respective lower-leg and upper-leg stations for proper accounting of mass to each deck level.

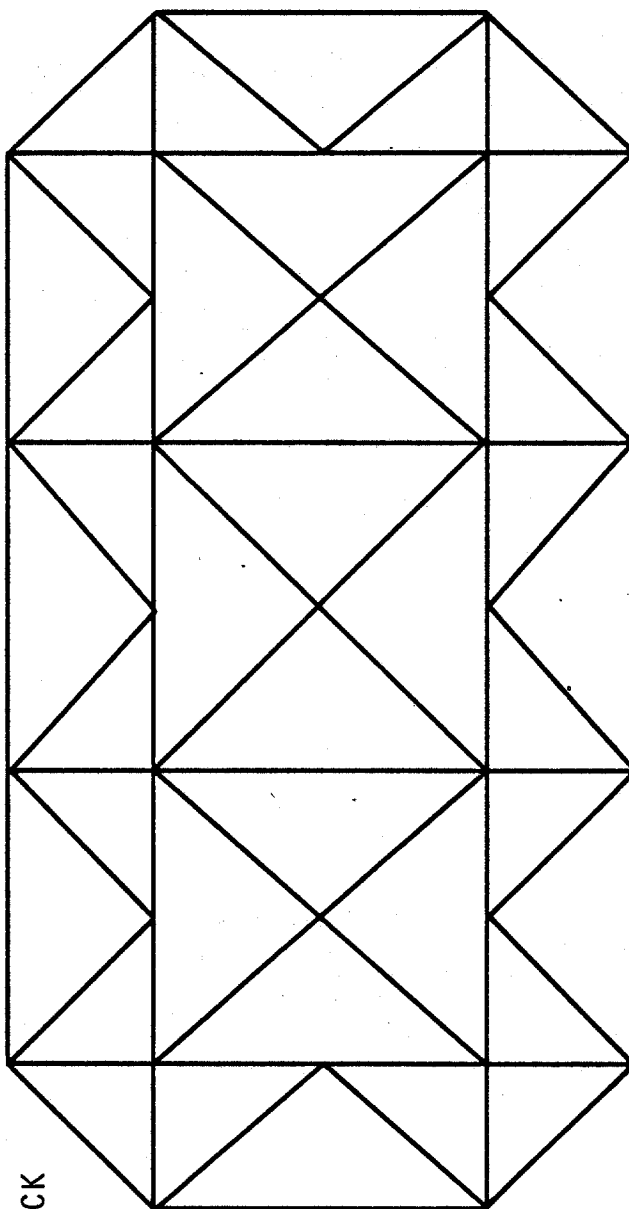
Mass associated with equipment and fluids was allocated to nodes closest to their locations. Special attention was paid to fluids in large tanks. Fundamental slosh frequencies for the 4000 bbl (640 m³) tank and flotation tank are estimated generally below 0.4 Hz. Since platform vibration modes of interest are at frequencies greater than 0.6 Hz, an adequate representation is achieved by simply removing the slosh mass from the tank fluid (slosh masses are estimated from data presented in Reference 1). A tabular listing of equipment and structural masses is presented in Table B-1.

3.3.3 Assembly of Dynamic Model of Decks

The structural stiffness and mass model described in Sections 3.3.1 and 3.3.2, respectively, is assembled in NASTRAN. The 593 dof model is then reduced by Guyan reduction (9) to a 96 dof description associated with the main leg nodes at the lower and upper deck levels (16 nodes, 6 dof each). It should be noted that



UPPER DECK



LOWER DECK

Figure 3-4
Member Network for Floors

the chosen reduction procedure produces coupled mass and stiffness matrices which reflect static deflection shapes and corresponding mass contributions at the nodes which are reduced out. Thus, a degree of consistency is retained in the reduced mass matrix which is not present when a mass relumping approach is employed. This reduced mass and stiffness matrix comprises the deck substructure model to be coupled with the jacket/pile/conductor model

3.4 FLUID VIRTUAL MASS

A new fluid virtual mass matrix was developed to represent inclined members in a more rigorous fashion than in the supplied model. The task consists of derivation of mass matrices in local displacement coordinates for each individual fluid element, followed by assembly of these elemental mass matrices into a global matrix. The latter is identical to that employed for all finite element analysis and is not elaborated upon. Definition of individual fluid mass elements appears not to be well known and so is discussed in detail.

Consider the arbitrarily oriented cylindrical beam illustrated in Figure-3-5. In terms of the beam local coordinate system (X_e, Y_e, Z_e), the virtual mass of surrounding fluid, m_∞ , which moves laterally with beam rigid body motion equals the mass of fluid displaced by the beam

$$m_\infty = \rho_w \pi R_o^2 \ell \quad (3-1)$$

where the beam length is given by

$$\ell = \sqrt{(x_b - x_a)^2 + (y_b - y_a)^2 + (z_b - z_a)^2}$$

The above is deduced from two-dimensional potential flow theory. If the member is flooded, an additional mass, m_f , moves with the beam

$$m_f = \rho_w \pi R_i^2 \ell \quad (3-2)$$

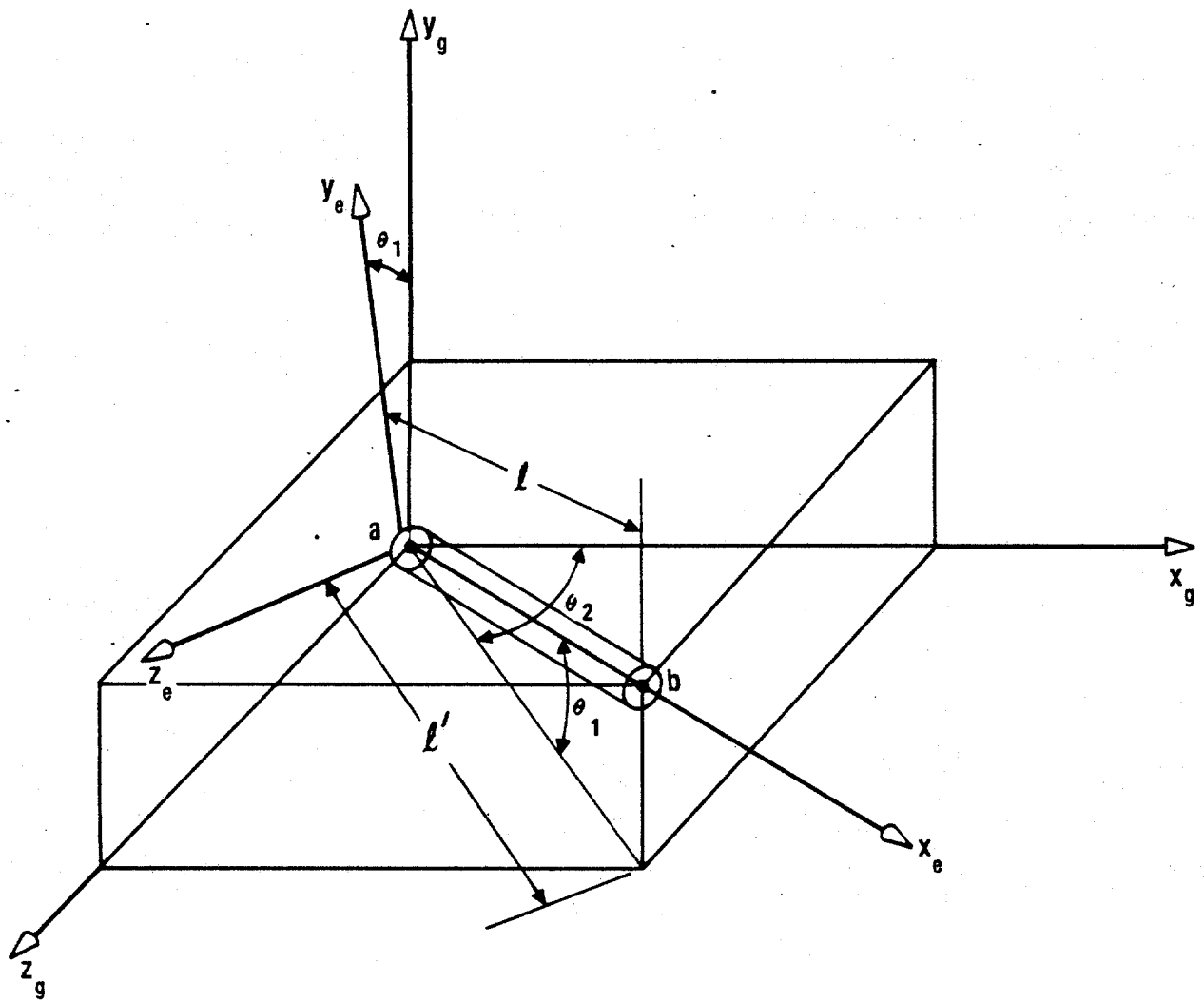


Figure 3-5. Arbitrarily Oriented Cylindrical Beam

The mass, m_f , is active in the two local lateral directions for an uncapped member, and in all three local directions for a capped member. In member local coordinates the added mass associated with surrounding fluid and flooding is

$$m_{xe} = \gamma_f \gamma_c m_f, \quad m_{ye} = m_{ze} = m_\infty + \gamma_f m_f \quad (3-3)$$

where $\gamma_f = 1$ (flooded), 0 (unflooded)

$\gamma_c = 1$ (capped), 0 (uncapped)

Adopting a lumped mass approximation, the fluid virtual mass matrix at end "a" or "b" of a typical beam in local displacement coordinates (X_e, Y_e, Z_e) is

$$M_{fe} = \frac{1}{2} \begin{bmatrix} m_{xe} & 0 & 0 \\ 0 & m_{ye} & 0 \\ 0 & 0 & m_{ze} \end{bmatrix} \quad (3-4)$$

It should be noted that the above expression holds for a fully submerged member. Special consideration is made for partially submerged members, accounting for proportional distribution of fluid mass.

On the basis of geometric data illustrated in Figure 3-5, the following transformation relating local and global displacements is defined:

$$\begin{Bmatrix} X_e \\ Y_e \\ Z_e \end{Bmatrix} = \begin{bmatrix} \cos \theta_1 \cos \theta_2 & \sin \theta_1 & \sin \theta_2 \sin \theta_1 \\ -\cos \theta_2 \sin \theta_1 & \cos \theta_1 & -\sin \theta_2 \sin \theta_1 \\ \sin \theta_2 & 0 & \cos \theta_2 \end{bmatrix} \begin{Bmatrix} X_g \\ Y_g \\ Z_g \end{Bmatrix} \quad (3-5)$$

where

$$\sin \theta_1 = (y_b - y_a)/\ell, \cos \theta_1 = \ell'/\ell$$

$$\sin \theta_2 = \begin{cases} (z_b - z_a)/\ell' & \text{if } \ell' \neq 0 \\ 0 & \text{if } \ell' = 0 \end{cases}$$

$$\cos \theta_2 = \begin{cases} (x_b - x_a)/\ell' & \text{if } \ell' \neq 0 \\ 1 & \text{if } \ell' = 0 \end{cases}$$

where

$$\ell' = \sqrt{(x_b - x_a)^2 + (z_b - z_a)^2}$$

$$\ell = \sqrt{\ell'^2 + (y_b - y_a)^2}$$

Denoting the transformation matrix defined in Equation (3-5) as ψ , the coupled fluid virtual mass matrix at node "a" or "b" in global coordinates is

$$M_f = \psi^T M_{fe} \psi \quad (3-6)$$

3.5 FOUNDATION MODEL

Soil stiffness is accounted for in the supplied model with an effective increase in pile cross-sectional area to account for axial stiffness [equivalent pile length below mudline is 100 ft (30.5 m)] and with a 6 x 6 stiffness matrix for each mudline node on the sixteen main and skirt piles to represent lateral stiffness properties. This matrix in kip, inch, radian units (given in global coordinates) is

$$\begin{matrix}
 & x & y & z & \theta_x & \theta_y & \theta_z \\
 \begin{matrix} x \\ y \\ z \\ \theta_x \\ \theta_y \\ \theta_z \end{matrix} & \begin{bmatrix} 510 & & & & & \\ & 510 & & & & \\ & & 0 & & & \\ & & & 55 \times 10^3 & & \\ & & & & 16.5 \times 10^6 & \\ & & & & & 16.5 \times 10^6 \\ & & & & & & 0 \end{bmatrix}
 \end{matrix} \quad (3-7)$$

The basic mathematical model does not account for any jacket/soil interface. Reference 16 incorporated a jacket mudline pin connection in an attempt to increase fundamental frequencies to agree better with measured data; the results indicated that such a constraint produces an overly high estimate of frequencies. In the present study, soft mudline springs are incorporated to account for the possibility of jacket/mudline contact. Appropriate values of the stiffness constraints are found by iteration as discussed in Section 3.7.

3.6 ASSEMBLY OF THE COMPLETE MATHEMATICAL MODEL

The matrix descriptions (mass and stiffness) for the jacket/pile/conductor, decks, fluid virtual mass and foundation were coupled employing the NASTRAN program. The component matrices are overloaded onto one another as indicated schematically in Figure 3-6. Initially the piles are assumed centered within the main legs; thus, the only pile/jacket connections are at the weld locations 15 ft (4.6 m) above water level. In subsequent parameter studies, intermediate jacket/pile connections were enforced by multi-point constraints in the two lateral displacement directions permitting pile freedom in the axial and rotational directions.

The assembled 1416 degrees of freedom (dof) mathematical model is then contracted by Guyan reduction (9) to a 213 dof representation to minimize computation costs while retaining necessary accuracy. The degrees of freedom retained in the reduced model, illustrated schematically in Figure 3-7, were selected for adequate representation of lateral, torsional, axial and cross-section distortion modes in the frequency range below 5 Hz.

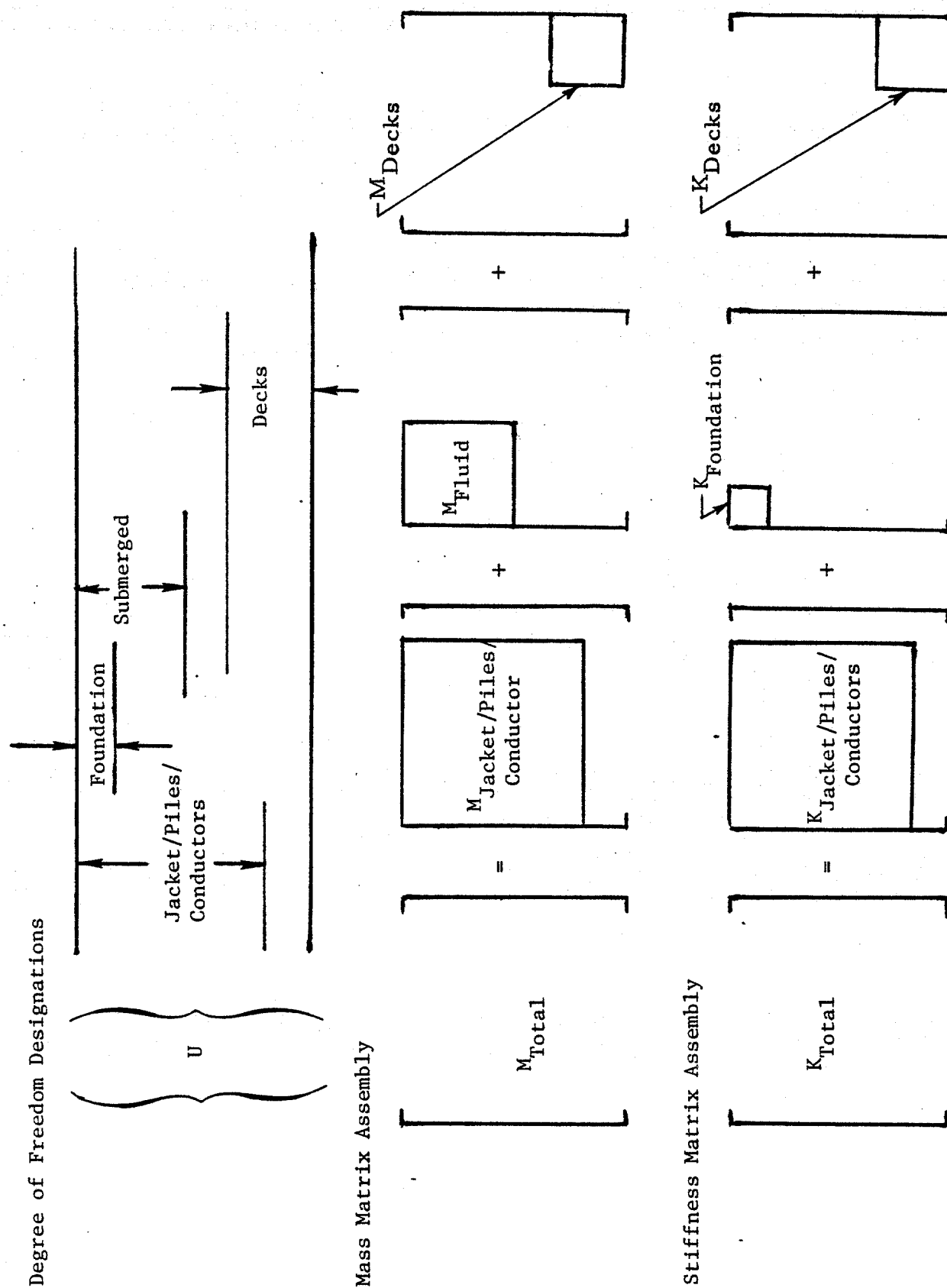


Figure 3-6. Assembly of Mathematical Model

3.7 ADJUSTMENT OF MODEL

A limited parametric study was performed to improve the accuracy of the mathematical model. Table 3-1 contains natural frequencies for the first 24 modes for a number of variations of the present model (Cases A to G), measured frequencies from Section 2, and frequencies from the supplied model (calculated by Shell). We observe that the fundamental model group (first 3 modes) for the supplied model are 12% to 18% lower than the measured frequencies. Our goal was to bring these frequencies into better agreement and at the same time bring the identified higher modes* into reasonable agreement. Our final model, to be used for the failure studies in Section 4, is Case G. It yields fundamental mode group frequencies within 0% to 3% of measured values, a second broadside frequency within 7%, a second torsion frequency within 1%, a third end-on frequency within 15%, and a first vertical within 4%. Except for the third end-on and third torsion modes, these are considerable improvements in accuracy relative to the supplied model as seen in Table 3-1.

The model variations studied in arriving at the final model (Case G) are now reviewed. A brief description of Cases A to G are contained in the legend to Table 3-1. Case A does not include the virtual mass contribution of fluid surrounding the submerged jacket members, nor the mass of fluid within the flooded main legs. In addition, the main piles are taken to be centered within the main legs (that is, no lateral constraint of the piles by the jacket). The consequence of adding virtual and flooded mass contributions is seen by comparison of Cases A and B. It is estimated that 13% to 28% of the effective mass in the fundamental mode group is associated with this added fluid mass. Moreover, it is seen that the added mass effect is significant for modes as high as the 24th. Cases A and B have the identical foundation modeling as does the supplied model. The primary reason for the 10% to 15% higher frequencies for Case B relative to the supplied model is believed to be the presence of the interdeck truss members in the present model. Secondary reasons are the more refined virtual mass representation and the fact that the supplied model has the main piles not centered within the main legs (that is, in contact

*Including the second broadside mode at 1.65 Hz detected by the shaker testing (17) as discussed in Section 2.6.

Table 3-1. Natural Frequencies for Model Adjustments
Referenced to Measured and Supplied Frequencies

No.	A	B	C	D	E	F	G	Description	Measured	Supplied
1	0.677	0.615	0.618	0.704	0.641	0.639	0.639	1st Broadside	0.646	0.56
2	0.721	0.637	0.653	0.731	0.662	0.659	0.659	1st End-On	0.658	0.58
3	0.972	0.913	0.932	0.938	0.937	0.938	0.935	1st Torsion	0.965	0.79
4	1.63	1.42	1.42	1.44	1.42	1.50	1.50	2nd End-On/Broadside		1.16
5	1.69	1.44	1.44	1.50	1.44	1.53	1.53	2nd Broadside/End-On	1.65	1.22
6	1.84	1.58	1.58	1.59	1.58	1.69	1.69	2nd Torsion	1.71	1.59
7	2.16	1.81	1.81	1.81	1.81	1.85	1.85	Conductor Modes		
8	2.47	1.83	1.83	1.84	1.84	1.88	1.88			
9	2.62	1.84	1.84	1.86	1.85	1.89	1.89			
10	3.16	1.85	1.86	1.87	1.86	1.92	1.92			
11	3.22	1.87	1.87	1.93	1.88	2.00	2.00	3rd Torsion	2.04	2.08
12	3.37	2.13	2.24	2.24	2.24	2.43	2.43	3rd End-On	2.12	2.13
13	3.44	2.19	2.38	2.39	2.38	2.66	2.68	3rd Broadside		2.27
14	3.64	2.58	2.58	2.58	2.58	3.07	3.08	Cross-Section Warping		
15	3.75	2.63	2.77	2.77	2.77	3.13	3.13			
16	3.92	2.75	2.84	2.84	2.84	3.13	3.14			
17	4.18	2.96	2.95	2.95	2.95	3.28	3.28			
18	4.30	2.99	3.15	3.16	3.15	3.50	3.53			
19	4.43	3.36	3.33	3.33	3.33	3.64	-			
20	4.59	3.75	3.56	3.56	3.56	3.71	3.71			
21	4.83	3.76	3.76	3.78	3.77	3.81	3.81			
22	4.84	3.79	3.78	3.80	3.78	3.96	3.97	First Vertical	3.81	
23	4.89	3.83	3.81	3.81	3.81	4.04	-			
24	5.29	4.10	3.98	3.99	3.99	4.12	4.13			

Legend:

A	No virtual or flooded mass, centered piles
B	Case A with virtual mass and flooded main legs
C	Case B with jacket/pile lateral pinning
D	Case C with jacket/pile vertical pinning
E	Case C with 500 KIP/in. leg/mud stiffness
F	Case E with piles in contact with leg shims
G	Case F with in-plane stiffening of decks

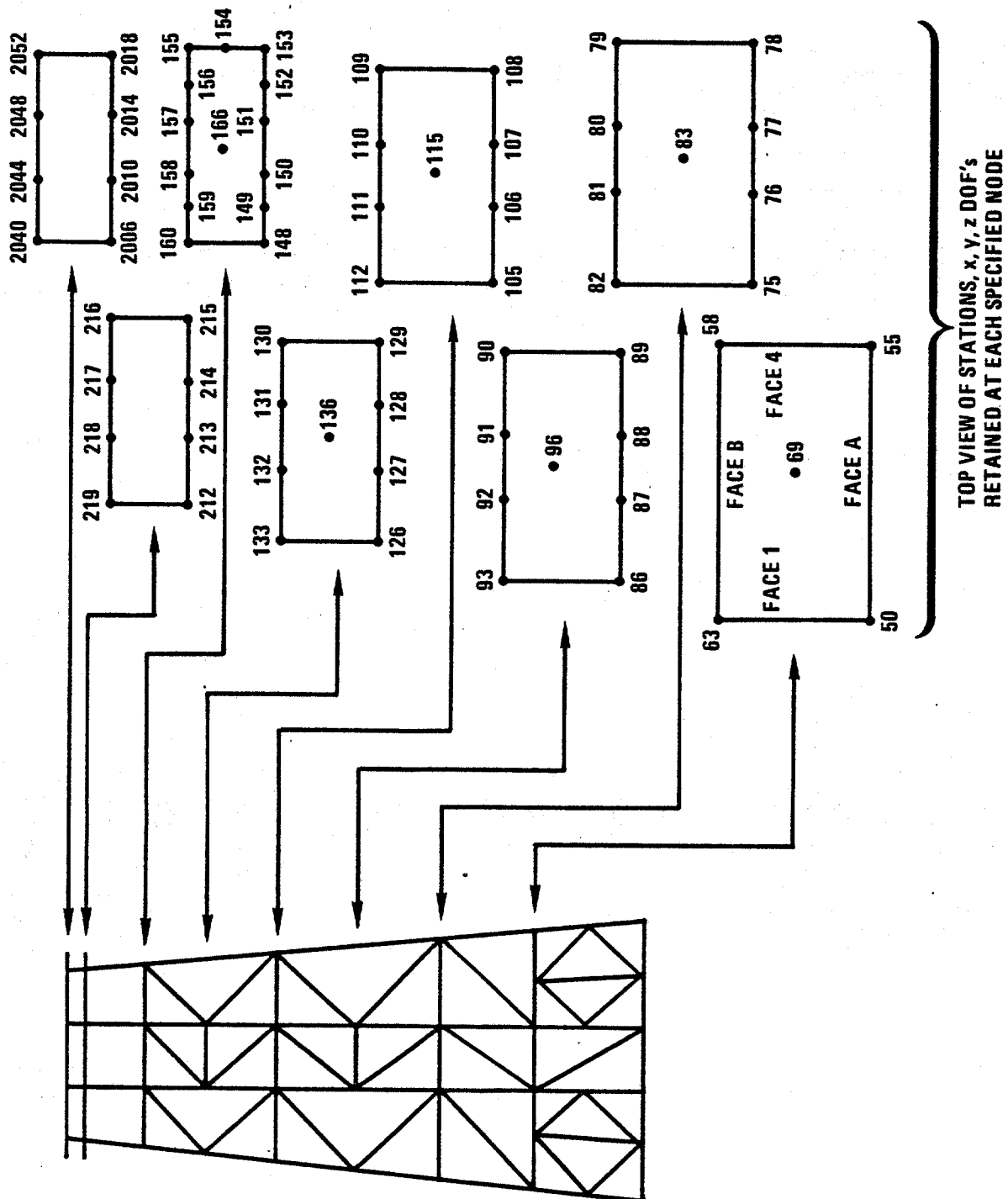


Figure 3-7

Illustration of Reduced Mathematical Model Degrees of Freedom

with the shims). Examination of shapes for modes 1-4 shows that the interdeck truss work causes the two decks to translate almost as a single rigid body. While corresponding shapes for the supplied model are not available, our approximate analysis of interdeck shearing indicates that much larger interdeck shear displacement would be present.

As seen in Table 3-1, the Case B natural frequencies for the first three mode groups are lower than available corresponding measured values. On the basis that foundation aspects are the least certain in the modeling, a series of foundation variations were studied next. First, Case C incorporates a pinned lateral connection between the main piles and the main legs at the mudline to represent shim contact at that position. This produces desired increases in the fundamental end-on and torsion mode frequencies, but has little effect on the fundamental broadside and on the second and third mode groups. It is speculated in Reference 16 that the mud mats may be in contact with the mud and are providing stiffness constraint to the base of the jacket. Pursuing this thought, an extreme case is evaluated to bracket a jacket/mud stiffness contribution. This is Case D in which the jacket is pinned to the main piles in the vertical, as well as in the lateral directions as in Case C. As seen in Table 3-1, this results, as expected, in overly high fundamental lateral mode frequencies, but in little change to the first torsion mode and to the second and third mode groups.

Next a reasonable jacket/mud vertical stiffness is sought. Several values of stiffness were tried before arriving at a value of 500 kip/in. (175 MN/m) per main leg producing Case E. That final value yields fundamental lateral/torsional mode group frequencies in good agreement with measured data as seen in Table 3-1. The higher modes appear relatively insensitive to jacket/mudline stiffness variation as seen by comparison of Cases C through E. It is of interest, however, to note that the difference in frequency between fundamental broadside and end-on modes is strongly affected by the value of jacket mudline stiffness.

The effect of main pile/jacket lateral constraint is next examined by enforcement of lateral displacement compatibility between main legs and piles at shim locations (as in the supplied model) to produce Case F. As anticipated on the basis of results in Reference 16, the effect of uncentered piles on the fundamental mode group is small. Several higher modes, however, are favorably adjusted as

seen for Case F in Table 3-1. In particular, the second and third torsional mode frequencies are brought to within 2% below measured values; those modes were previously close to 8% lower in frequency than measured values.

Examination of several modes in the frequency range above 3.5 Hz reveals significant in-plane deformation of the decks. A reassessment of the deck model led to the conclusion that neglected flooring members account for significant stiffness not in the present deck model. Therefore, the equivalent cross-members should be rigidized in their respective local axial directions. This is accomplished in Case G. As seen in Table 3-1, the result is negligible frequency shifts in all the modes, but modes 20 and 23 involving in-plane deck deformation are eliminated.

At this point, parametric adjustment of the mathematical model is terminated, since it is judged that the adjusted model represents an acceptably good simulation of the actual platform within the scope of the present studies. A set of mode shape plots for the final model are presented in Figures B-1 through B-22 for the structure above the -26 ft (-7.9 m) level and for the entire structure. The first mode group shapes are in good agreement with the available measured data.

More can be done to further improve the model should this be deemed desirable for future studies. Candidate improvements are (a) modeling of heavy deck equipment and superstructure as flexible bodies including support flexibility, (b) employment of a "consistent mass" formulation for the jacket/pile/conductor model, (c) comprehensive review of the conductor idealization with possible remodeling, and (d) refinement of modes by subspace iteration (4). The first, second and third suggestions would tend to improve measurement/analysis fidelity in the higher modal groups. The fourth suggestion would insure against skipping higher modal content inherent in the full (1416 dof) model; moreover, some difficulties encountered in numerics associated with damage analysis to be discussed in the following sections would be avoided.

4. DAMAGE SENSITIVITY STUDIES

4. DAMAGE SENSITIVITY STUDIES

4.1 EFFICIENT ANALYSIS METHOD

During the previous contract (2), an approximate technique was developed for efficient re-analysis of a structure subjected to local alteration. The technique, based on Rayleigh-Ritz considerations, employed a set of trial shapes consisting of a truncated set of original structure modes augmented by a set of vectors associated with applied static loads at the degrees of freedom influenced by the damaged member or altered mass. Unanticipated computational cost penalties, associated with formation of explicit inverses of a large matrix, led to reformulation of the technique during the present study. Recent developments in the application of residual vectors for component mode synthesis (8, 14) provided the basis for the new formulation presented below.

We begin with the description of the free vibration of a structure in the standard matrix form

$$M\ddot{X} + KX = 0 \quad (4-1)$$

where X is the vector of displacements, M is the mass matrix, and K is the stiffness matrix. The modal matrix ϕ_t , corresponding to any truncated set of modal (generalized) displacements q_t , relates the physical displacements, X_t , stemming from the truncated set of modes to the modal displacements

$$X_t = \phi_t q_t \quad (4-2)$$

Applying this transformation to Equation (4-1) produces the uncoupled modal dynamic equation set

$$I_t \ddot{q}_t + \Lambda_t q_t = 0 \quad (4-3)$$

where

$$\phi_t^T M \phi_t = I_t, \quad \phi_t^T K \phi_t = \Lambda_t$$

and I_t is the unit matrix and Λ_t is a diagonal matrix of squared natural frequencies ω_n^2 corresponding with the mode shape vector columns of ϕ_t .

Introduction of stiffness and/or mass alteration to the original structure, and use of the above transformation to express an approximate smaller dynamic problem, has been shown to produce considerable errors in the altered mode shapes and frequencies (8). Augmentation of the original truncated mode set with a small set of static residual vectors provides the desired increased accuracy.

Consider the static response of the original structure to unit loads applied at the degrees of freedom corresponding to nodes of a removed member. The set of unit load vectors is denoted by a matrix, Γ , for which each column corresponds to an individual load vector. For example, for vector column j , if a unit load is applied at X_{ij} , then $X_{ij} = 1$ and all other entries in column j are null. The static displacement vector set, X_s , is therefore

$$X_s = K^{-1} \Gamma \quad (4-4)$$

The approximate static displacement based on the truncated mode set is

$$X_{st} = \phi_t \Lambda_t^{-1} \phi_t^T \Gamma \quad (4-5)$$

and the difference between the exact and truncated static displacements defines the residual displacement, ϕ_ρ , associated with static displacement of modes not included in ϕ_t :

$$\phi_\rho = K^{-1} \Gamma - \phi_t \Lambda_t^{-1} \phi_t^T \Gamma \quad (4-6)$$

The truncated mode set, augmented by residual vectors comprises an exact static response characterization of the original structure subjected to loads at the damage degrees of freedom. The transformation is

$$X = (\phi_t \mid \phi_\rho) \begin{Bmatrix} q_t \\ q_\rho \end{Bmatrix} \quad (4-7)$$

Application of this transformation to the Equation (4-1) in the same manner as Equation (4-3) yields

$$\begin{bmatrix} I_t & 0 \\ 0 & \phi_\rho^T M \phi_\rho \end{bmatrix} \begin{Bmatrix} \ddot{q}_t \\ \ddot{q}_\rho \end{Bmatrix} + \begin{bmatrix} \Lambda_t & 0 \\ 0 & \phi_\rho^T K \phi_\rho \end{bmatrix} \begin{Bmatrix} q_t \\ q_\rho \end{Bmatrix} = \begin{Bmatrix} 0 \\ 0 \end{Bmatrix} \quad (4-8)$$

where the off diagonal partitions are null due to the orthogonality of the truncated and residual mode sets. That is

$$\phi_t^T K \phi_\rho = 0, \quad \phi_t^T M \phi_\rho = 0$$

The first of the above expressions is easily proven by direct substitution of Equation (4-6) for ϕ_ρ , while proof of the second expression is a bit more involved (8).

Consider now removal of the stiffness associated with a severed element which connects to the degrees of freedom denoted in Γ . The displacements associated with the particular element (a set of 12 for a beam), X_e , are selected as

$$\begin{aligned} X_e &= \Gamma^T X = (\Gamma^T \phi_t | \Gamma^T \phi_\rho) \begin{Bmatrix} q_t \\ q_\rho \end{Bmatrix} \\ &= (\phi_{te} | \phi_{\rho e}) \begin{Bmatrix} q_t \\ q_\rho \end{Bmatrix} \end{aligned} \quad (4-9)$$

The strain energy associated with the removed member is

$$U_e = \frac{1}{2} X_e^T K_e X_e \quad (4-10)$$

where K_e is the stiffness matrix for the element. Substituting for X_e the last form of Equation (4-9), the change in generalized stiffness is

$$\Delta K_q = \begin{bmatrix} \phi_{te}^T & K_e \phi_{te} & \phi_{te}^T & K_e \phi_{\rho e} \\ \phi_{\rho e}^T & K_e \phi_{te} & \phi_{\rho e}^T & K_e \phi_{\rho e} \end{bmatrix} \quad (4-11)$$

Finally, the approximate equation of motion for the damaged structure is

$$\begin{bmatrix} I_t & 0 \\ 0 & \phi_{\rho}^T M \phi_{\rho} \end{bmatrix} \begin{Bmatrix} \ddot{q}_t \\ \ddot{q}_{\rho} \end{Bmatrix} + \begin{bmatrix} \Lambda_t & 0 \\ 0 & \phi_{\rho}^T K \phi_{\rho} \end{bmatrix} \begin{Bmatrix} q_t \\ q_{\rho} \end{Bmatrix} - \Delta K_q \begin{Bmatrix} q_t \\ q_{\rho} \end{Bmatrix} = \begin{Bmatrix} 0 \\ 0 \end{Bmatrix} \quad (4-12)$$

It is noted here that the reduced stiffness matrix exactly represents the static behavior of the damaged structure when subjected to loads at the damage degrees of freedom. Moreover, if we are interested in determining the first 30 modes of the damaged structure, we need consider 30 original structure modes, ϕ_t , plus the appropriate 12 residual modes due to removal of a single beam element stiffness*. The reduced eigenvalue problem consists of 42 equations compared to 213 equations utilized in the untruncated structural analysis. Since the computational cost of a modal eigenvalue analysis is proportional to the square of the order, the cost of damage mode calculation is roughly 4% of that associated with the untruncated model. The one extra computer run incurred in calculation of residual vectors is greatly offset by the savings associated with approximate analysis of a large number of damage cases.

Accuracy of the efficient analysis method is demonstrated in an example for which a Face 4 diagonal member (4530) has been severed. Location of the subject member is illustrated in Figure 4-3 (to be discussed in Section 4.5). Vibration mode data were calculated by analysis of the complete model in NASTRAN and by the efficient technique. The first 30 modal frequencies of the baseline structure (undamaged), damaged structure (NASTRAN) and damaged structure (efficient technique) are provided in Table 4-1. It is noted first that the frequency shifts

*The use of 12 residual modes per member removal was done for simplicity in computer programming. Six per removal, one for each of six self equilibrating load sets is sufficient. In fact, in most cases the predominant member loading is axial so that only one corresponding residual mode may have been sufficient.

Table 4-1 Comparison of Modal Frequencies from NASTRAN and Efficient Method (Member 4530 Failure)

	<u>Baseline</u>	<u>Damaged</u>	
		<u>NASTRAN</u>	<u>(Efficient)</u>
1	0.6391 Hz	0.6165 Hz	0.6162 Hz
2	0.6592	0.6593	0.6592
3	0.9351	0.8730	0.8724
4	1.495	1.487	1.486
5	1.532	1.519	1.518
6	1.686	1.628	1.626
7	1.852	1.852	1.852
8	1.881	1.875	1.875
9	1.894	1.889	1.889
10	1.921	1.915	1.915
11	2.002	1.948	1.947
12	2.434	2.421	2.420
13	2.678	2.493	2.490
14	3.079	2.841	2.839
15	3.133	3.084	3.084
16	3.135	3.138	3.134
17	3.282	3.282	3.282
18	3.529	3.529	3.529
19	3.711	3.635	3.633
20	3.810	3.713	3.712
21	3.974	3.815	3.811
22	4.128	3.996	3.996
23	4.183	4.129	4.128
24	4.366	4.344	4.343
25	4.547	4.410	4.412
26	4.569	4.552	4.550
27	4.721	4.593	4.584
28	4.929	4.930	4.926
29	4.976	4.969	4.968
30	5.155	5.160	5.155

due to damage are not numerically negligible in general. Moreover, the results of complete NASTRAN analysis and the efficient technique are extremely close to one another (within 0.2%).

4.2 INTERPRETATION OF ANALYTICAL SENSITIVITY DATA

The form of the approximate equations of motion for the damaged structure in Equation (4-12) provides an identification of the modes as a superposition of the truncated modes of the undamaged structure and the residual vectors. As will be seen, this form is most useful for tracking changed modes and for easily spotting important mode shape changes.

The modes from Equation (4-12) are expressed in terms of a modal transformation ϕ_d :

$$\begin{Bmatrix} q_t \\ q_\rho \end{Bmatrix} = \phi_d q_d \quad (4-13)$$

where the q_d are the generalized coordinates for the damaged structure. Note from Equation (4-12) that if there is no change in generalized stiffness ($\Delta K_q = 0$), then

$$\phi_d = \begin{bmatrix} I_t & | & 0 \\ \hline 0 & | & \psi_\rho \end{bmatrix} \quad (4-14)$$

The left column shows that the original mode shapes are preserved. The right column represents a "modal" transformation for the residual vectors which remain orthogonal to the unaltered truncated mode set. Also, the natural frequencies of the lower truncated set are necessarily identical to these of the undamaged structure in this limiting case.

The case of change in generalized stiffness, ΔK_q , is now considered. Calculation of the mode shapes from Equation (4-12) with the vectors normalized to unit modal mass will produce generally full columns in ϕ_d . The extent of alteration in mode shape can be assessed by the deviation of ϕ_d from the limiting undamaged case in Equation (4-14). An interpretive example case is presented next as an illustration.

Consider column j of ϕ_d along with the associated natural frequency,

ω_{dj} ,

$$\phi_{dj} = \begin{pmatrix} \epsilon_{1j} \\ \epsilon_{2j} \\ \vdots \\ 1 + \epsilon_{kj} \\ \vdots \\ \epsilon_{Nj} \end{pmatrix} \quad (4-15)$$

where N is the order of the approximate equation set (number of truncated original modes plus residual degrees of freedom). The ϵ 's are typically much less than one. It is assumed that the normalization process will require that ϵ_{kj} be negative to insure unit modal mass. The largest entry in Equation (4-15), namely the $1 + \epsilon_{kj}$ in row k , indicates that the mode j of the altered structure corresponds most closely with mode k of the undamaged structure. Moreover, the smaller entries, ϵ_{ij} ($i \neq k$), indicate the extent to which the original mode shape is altered by combination with other original modes. In particular, if Equation (4-13) is combined with the modal transformation for the undamaged structure, Equation (4-7), the physical displacements in mode j of the damaged structure is

$$X_{dj} = \left(\phi_t \mid \phi_\rho \right) \phi_{dj} q_{dj} \quad (4-16)$$

It becomes clear that this product of modal vectors represents the combination of original modes producing the deflections in the damaged case. That is,

$$X_{dj}/q_{dj} = \phi_{1j} \epsilon_{1j} + \phi_{2j} \epsilon_{2j} + \dots + \phi_{kj} (1 + \epsilon_{kj}) + \dots + \phi_{Nj} \epsilon_{Nj} \quad (4-17)$$

where the ϕ_{ij} are the elements of the j th row of the original modal transformation $(\phi_t \mid \phi_\rho)$. The ϵ_{ij} entries are thus the fractional contributions of original modes comprising the damaged structure mode.

It is emphasized that the sequencing of damaged structure modes may change (e.g., original sequence is broadside 1, end-on 1, torsion 1, . . . while the

altered sequence may be "end-on 1", "broadside 1", "torsion 1", . . .). The largest elements of ϕ_d show the correspondence of the modes of the damaged structure to the modes of the original structure. In the example posed by Equation (4-15), the fractional change in the "kth" original structure modal frequency is

$$\frac{\Delta \omega_k}{\omega_k} = \frac{\omega_{dj} - \omega_k}{\omega_k} \quad (4-18)$$

Usually a damaged structure mode is predominantly a combination of original modes closest in frequency to that of the subject mode. In some cases, however, entirely new modes are introduced which are well within the frequency range of the truncated original mode set. Such modes are characterized by large contributions associated with the residual vectors. In order to facilitate the assessment of the residual contributions, the residual modal coordinates in Equation (4-12) are scaled so that the residual mass matrix becomes the unit matrix I_ρ . This is accomplished by employing the Cholesky factor decomposition (10) of the residual mass matrix

$$\phi_\rho^T M \phi_\rho = L_\rho L_\rho^T \quad (4-19)$$

where L_ρ is a lower triangular form, and introducing the transformation

$$q_\rho = L_\rho^{-T} q'_\rho \quad (4-20)$$

Application of this transformation to Equation (4-12) in the usual symmetric manner produces the mass balanced approximate equation set

$$\begin{bmatrix} I_t & 0 \\ 0 & I_\rho \end{bmatrix} \begin{Bmatrix} \ddot{q}_t \\ \ddot{q}_\rho \end{Bmatrix} + \begin{bmatrix} K'_d \end{bmatrix} \begin{Bmatrix} q_t \\ q_\rho \end{Bmatrix} = \begin{Bmatrix} 0 \\ 0 \end{Bmatrix} \quad (4-21)$$

where

$$K'_d = \begin{bmatrix} \Lambda_t & 0 \\ 0 & L_\rho^{-1} (\phi_\rho^T K \phi_\rho) L_\rho^{-T} \end{bmatrix} - \begin{bmatrix} I_t & 0 \\ 0 & L_\rho^{-1} \end{bmatrix} \begin{bmatrix} \Delta K_q \end{bmatrix} \begin{bmatrix} I_t & 0 \\ 0 & L_\rho^{-T} \end{bmatrix}$$

The only difficulty noted in this form is the possibility of a singular (or poorly conditioned) residual mass matrix which may occur due to use of a singular lumped mass matrix for the mathematical model (i.e., rotational inertial terms are null for beam members). Calculation of damaged structure modes with the balanced equation set has been found to alleviate interpretive difficulties for several damage configurations; however, singularities in residual mass were noted in two exceptional cases to be discussed in a later section.

Observable changes in mode shapes can be identified by evaluation of the interrelationships among mode shape physical displacements as defined in Equation (4-16) (e.g., the ratio of two corner lateral displacements). The degree of excitation of a mode from wind and waves may be roughly assessed by noting physical displacements in the vibration modes near the ocean surface (where wave excitation occurs) as well as deck physical displacements (where wind excitation occurs). Relatively low modal displacements on the deck and ocean surface vicinities indicates that a mode is not likely to be observable with ambient vibration monitoring.

In summary, the procedure for evaluation of analytical sensitivity data is as follows:

- o Classify altered structure modal data with respect to original structure modal data on the basis of dominant original mode contributions in the vectors ϕ_d .
- o Calculate frequency alteration on the basis of corresponding damaged and undamaged structure modes; see Equation (4-18).
- o Quantify overall mode shape sensitivity on the basis of the relative original mode contributions in ϕ_d ; see Equation (4-17).
- o Assess observability and alteration of mode shapes on the basis of physical mode shape displacements; see Equation (4-16).

4.3 CRITERIA FOR FAILURE DETECTION

Before proceeding to the matter of the predicted frequency and mode shape changes resulting from failures, we address the question of how reliably such changes can be detected from monitoring data. We are faced with measurement uncertainty as well as uncertainty due to nonfailure causes. Because the prediction of sensitivity to nonfailure causes was beyond the scope of this study, the failure detection criteria developed will necessarily be somewhat speculative.

First we deal with the matter of the detectability of changes in modal frequencies. We assume that all known reasons for shifts of natural frequencies (that is, all nonfailure bias causes) have been estimated and taken into account. For example, a complete inventory of deck mass has been made, the extent of marine growth has been estimated, and the modal frequencies adjusted on the basis of sensitivity analyses regarding such effects. In the absence of structural failure, we assume that there is a zero-mean, normally distributed, random uncertainty in each natural frequency. This random uncertainty results from errors in measurement and in accounting for the various nonfailure effects.

The following question is now asked: In a remeasure of the natural frequencies of a platform, what magnitudes of change would have to be detected to conclude reliably that structural failure has occurred? We approach the answer by first hypothesizing that no failure has in fact occurred. It follows that there is no difference between the mean value of a natural frequency (adjusted for bias

effects) and its prior mean value. Further we assume that the standard deviation, σ , for the two measurements (new and previous) are the same. Since the two measurements are independent of one another, basic statistical theory tells us that the random difference between them has a standard deviation of $\sqrt{2} \sigma$. We can conclude, that with a chance of being wrong 5% of the time, a difference in a natural frequency of more than $2 \sqrt{2} \sigma$ is cause for rejection of the original hypothesis that no failure has occurred. This will be the basis of our threshold estimate.

It remains to estimate the value of the standard deviation. For the well identified modes of SP-62C, four categories of random error are estimated and their 2σ values (95% likelihood) listed in Table 4-2. These are measurement errors, sea state nonlinear effects, errors in estimating deck mass, and a miscellaneous category. The values in the "measurement" column reflect the judgement that the uncertainties given in Table 2-2 are 2σ values. The "sea state" column shows 1/3 of the shifts seen in the natural frequencies of the fundamental mode group from a calm to a moderately heavy sea condition as a judgement of the uncertainty in the ability to bias these frequencies for the observed sea state. The next two columns are based upon pure guesses in the absence of any study for SP-62C. The "deck mass" column reflects the roughly estimated frequency effects of a 5% uncertainty in the mass of contained fluids, which for SP-62C accounts for 31% of the total deck mass. The "miscellaneous" column is an optimistically low "crystal ball" guess at everything else (such as soil stiffness properties, mudline movement, marine growth, corrosion). The modes above the fundamental group are given a higher frequency uncertainty based upon tendencies noted in the sensitivity studies of Reference 20. Based upon the independence of the errors in the four categories, the "net" column is their root-sum-square combination. The "detection threshold" values in the last column of Table 4-2, given by $\sqrt{2}$ times the net 2σ errors as derived in the previous paragraph, are interpreted to be the minimum changes in natural frequency for reliable indication of structural failure. As an overall judgement these results are viewed as probably being optimistic. Since the results are at best qualitative, for ease of following discussions, a 1% frequency change for the fundamentals and a 2% change for the higher modes will be employed as an optimistic threshold of failure detectability.

Table 4-2. Estimates of Thresholds for Detectability of Frequency Changes

Mode	2 σ Error %				Detection Threshold ²
	Measurement	Sea State	Deck Mass	Miscellaneous	Net ¹
First Broadside	0.77	0.33	0.38	0.5	0.88
First End-On	0.76	0.33	0.38	0.5	0.88
First Torsion	0.52	0.66	0.38	0.5	0.63
Second Torsion	1.17	0	0.3	1.0	1.57
Third End-On	0.94	0	0.3	1.0	1.40
First Vertical	0.51	0	0.8	1.0	1.38

¹ Root sum square of component errors

² Net 2 σ error times $\sqrt{2}$

The estimation of a detection threshold for mode shape is even more nebulous than for frequency. For one thing, no information at all is available for nonfailure causes even in the literature. One positive point is that no uncertainties are expected to result from sea state nonlinear effects since the symmetry properties of the platform should not be influenced. The measurement uncertainties stated in Section 2.5 are 10% for ratios of major deflections for the fundamental modes and 20% for the higher well identified modes. Let us assume, as was done for the frequency uncertainties, that these are 2σ values. For want of anything more sensible, we further assume that the ratio between frequency detection thresholds and 2σ measurement errors in Table 4-2 applies roughly as well to the mode shape detection thresholds. A round number for this ratio is 2. So the thresholds become 20% and 40% in major modal ratios for the fundamental and higher well identified modes, respectively.

A caution about high coherency is in order. The uncertainties in measurement of an amplitude ratio (and phase) decrease as the coherency increases (7). So these thresholds apply only if the coherencies are comparable to those measured on SP-62C (discussed in Section 2.5). A situation where such high coherency may not be possible to attain is when the broadside and end-on modes couple together in shape but are still very close in frequency. If this becomes an important consideration for reliable failure detection, special study will be needed.

4.4 MODE OBSERVABILITY

The ability to detect natural frequencies and mode shapes from field data is essential to the monitoring method. Here we deal with the matter of the relative likelihood of good observability of the modes in a field test on the basis of the analytically predicted modes.

The structural response in a mode is proportional to the product of the modal amplitudes at the measurement and excitation locations, as well as to the level of the excitation at the modal frequency. Predicted modal amplitudes along a corner leg are presented in Figure 4-1 for modes 1-6 and 11-16 in the directions indicated.* Figure 4-2 contains plots of the largest of the two lateral modal amplitudes at the A4 or B1 legs versus mode number (1-15) for three platform levels: -26 ft (-7.9 m), 14 ft (4.3 m) and the decks.

*Conductor modes 7-10 are not useful for monitoring and are ignored.

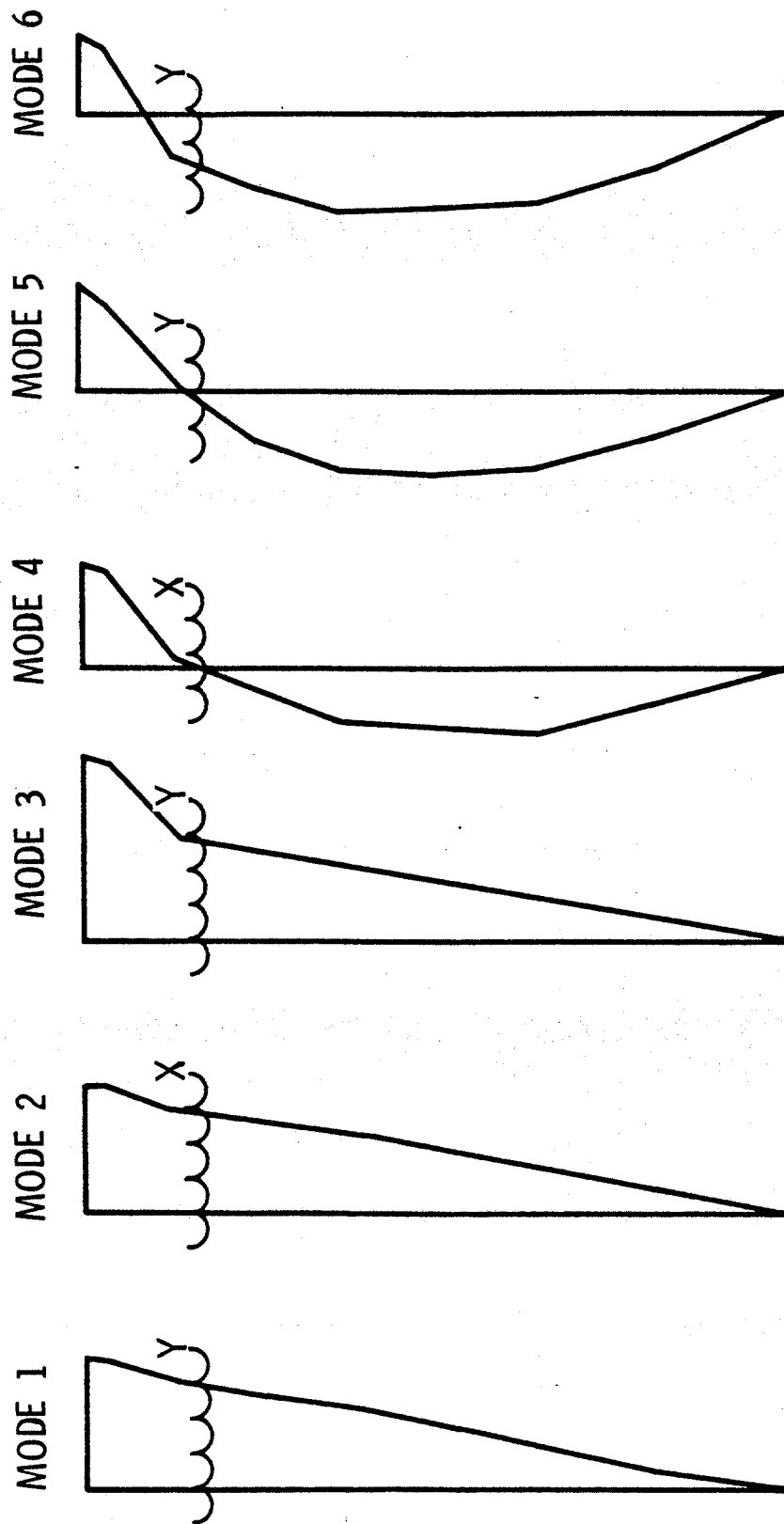


Figure 4-1. Lateral Modal Deflection Patterns in a Corner Leg

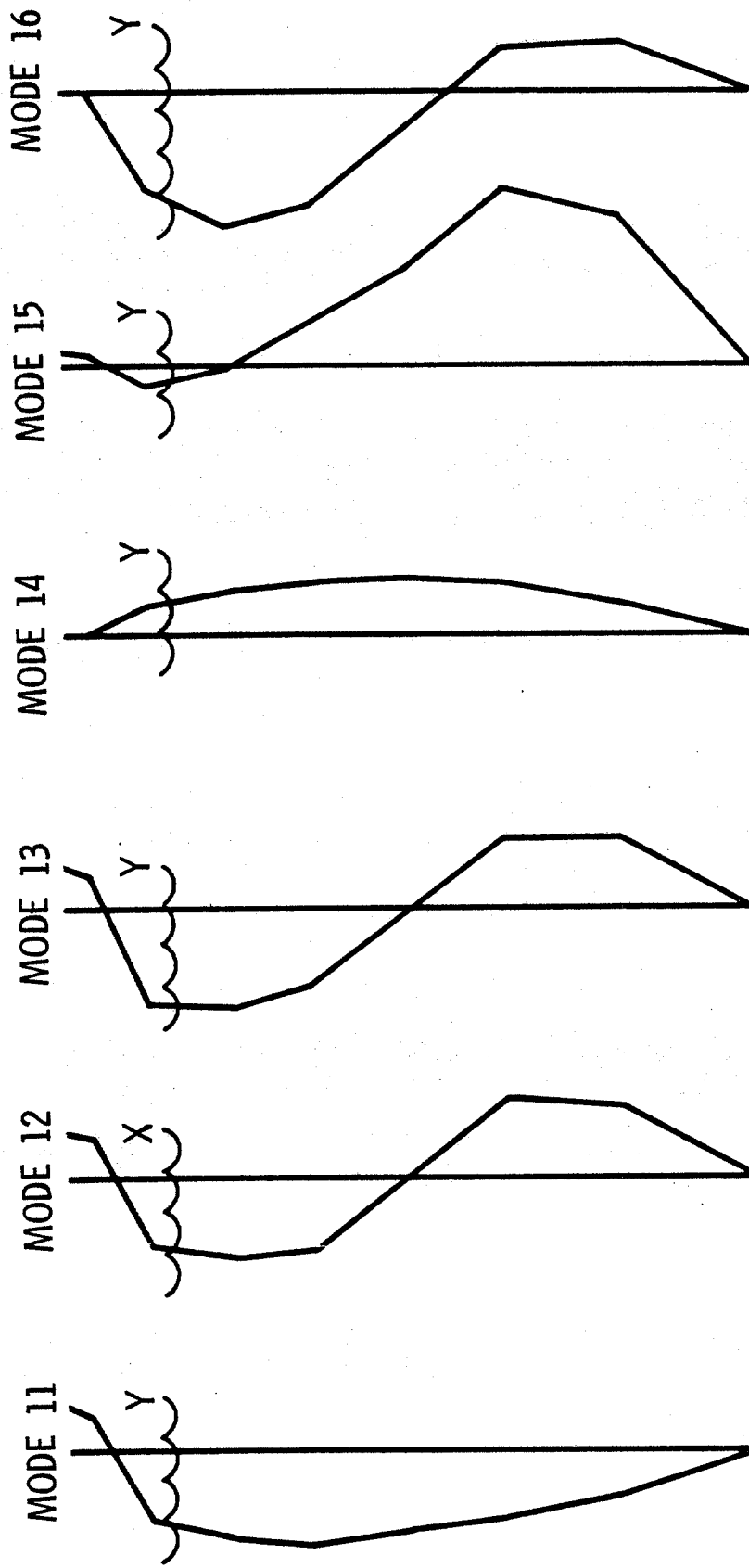


Figure 4-1 (cont'd). Lateral Model Deflection Patterns in a Corner Leg

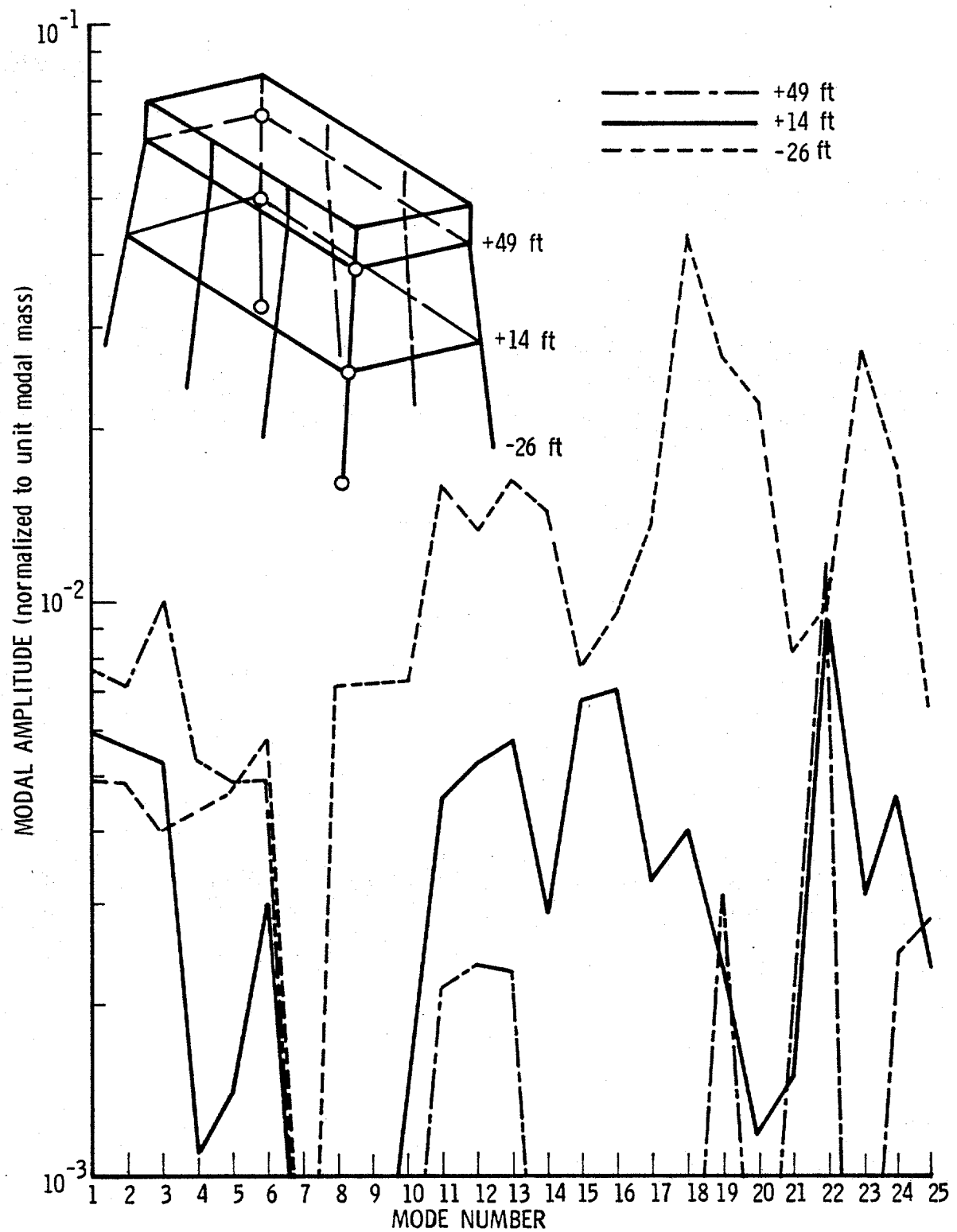


Figure 4-2. Modal Amplitudes at Various Upper Platform Stations

On the assumption that the predominant ambient excitation exists near the sea surface, Figure 4-1 shows that modes 4, 5 and 15 would tend to be poorly excited and hence poorly observable. Moreover, it is seen that the most advantageous measurement locations in the first two fundamental mode groups (modes 1-6) are at the deck level. Higher modes are more appropriately measured at the 14 ft (4.3 m) level, and even better measured at the -26 ft (-7.9 m) level, as indicated in Figure 4-2. High modal amplitudes at this below water level are attributed to the long unsupported column sections on the A4 and B1 legs (see the Appendix B modal plots). Increased difficulties and cost will clearly result from below water accelerometers. Such locations, however, should at least be considered if improved modal sensitivity in higher modes were found to be highly useful. It is noteworthy that conduits enabling below water placement of accelerometers from topside have been installed on legs of Cognac and are or will be installed on several other Shell platforms.

4.5 FAILURE SENSITIVITIES FOR FIRST THREE MODE GROUPS

A representative set of 31 single member failure configurations was selected to evaluate vibration mode sensitivity to encompass various member types (diagonal, vertical, horizontal), degrees of redundancy of member groups, and various member locations. The selected members are noted and numbered in Figure 4-3; their location within bays I-IV are sometimes referenced. In addition, a single main pile failure condition in the A4 leg was selected to assess sensitivity of that member type. Sensitivity of the lower three lateral and torsional mode groups to member failures is covered in the following discussion. Failure sensitivities of higher modes are covered in Section 4.7.

4.5.1 Face 4 Diagonal Member Failures

The frequency and mode shape sensitivity associated with Face 4 diagonal member failures is summarized in Table 4-3. Generally, it is noted that a 2.8 to 3.6% reduction in the fundamental broadside frequency (f_{bl}) occurs and a more pronounced 4.8 to 6.7% reduction in the fundamental torsional frequency (f_{tl}) occurs. The fundamental end-on frequency (f_{el}) and mode shape (ϕ_{el}) are virtually unaffected by Face 4 diagonal failures since those members contribute negligible strain energy in such a mode. In contrast, the fundamental broadside and

*Conductor modes 7-10 are not useful for monitoring and are ignored.

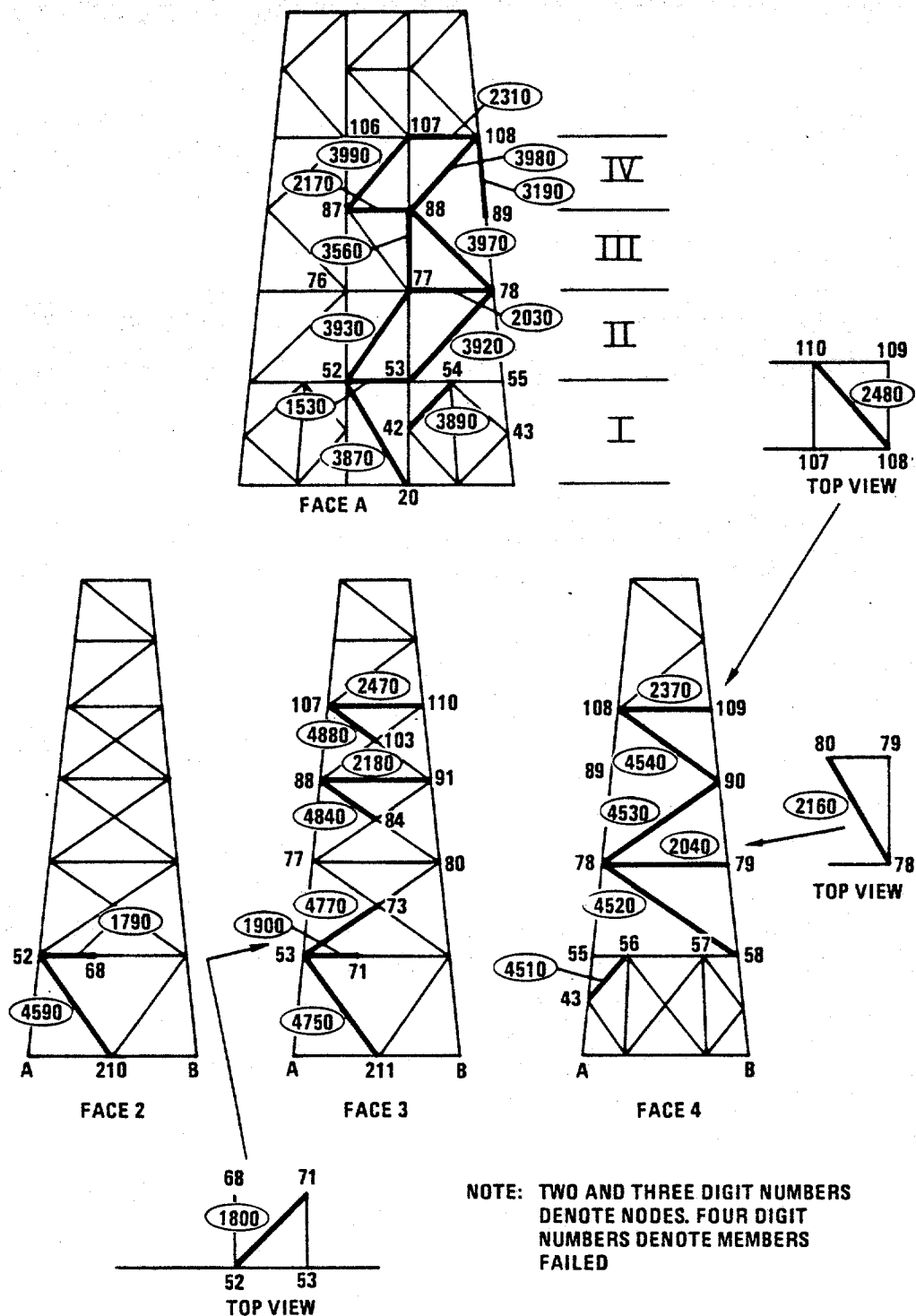


Figure 4-3. Identification of Member Failure Cases

Table 4-3. Face 4 Diagonal Member Failure Modal Sensitivity¹

Group 1 Modes					
Member	² % Δf_{bl}	% Δf_{el}	% Δf_{tl}	ϕ_{el}	ϕ_{tl}
4520(II) ³	-2.8	-	-4.8	-	0.11b ₁ , 0.99t ₁
4530(III)	-3.6	-	-6.7	-	0.14b ₁ , 0.98t ₁
4540(IV)	-3.0	-	-5.7	-	0.12b ₁ , 0.99t ₁
Group 2 Modes					
Member	% Δf_{l2}	% $\Delta f_{l2'}$	% Δf_{t2}	$\phi_{l2'}$	ϕ_{t2}
4520	-2.7	-1.8	-4.7	0.79l ₂ , 0.59l _{2'} , 0.17t ₂	0.15l ₂ , 0.47l _{2'} , 0.86t ₂
4530	-0.6	-0.9	-3.6	0.35l ₂ , 0.91l _{2'} , 0.17t ₂	0.12l ₂ , 0.25l _{2'} , 0.93t ₂
4540	-	-	-1.4	0.07l ₂ , 1.0l _{2'} , 0.05t ₂	0.04l ₂ , 0.06l _{2'} , 0.99t ₂
Group 3 Modes					
Member	% Δf_{t3}	% Δf_{e3}	% Δf_{b3}	ϕ_{t3}	ϕ_{b3}
4520	-0.9	-	-	0.99t ₃ , 0.11t ₂	-
4530	-2.7	-0.6	-7.0	highly coupled group	
4540	-1.8	-0.6	-7.7	highly coupled group	

¹ No entry for a Δf indicates <0.5% change;
No entry for ϕ indicates <0.05 contribution of other shapes.

² Box around Δf indicates mode well identified by test.

³ Bays denoted in parentheses.

torsional mode shapes (ϕ_{b1} and ϕ_{t1}) are affected in that the altered broadside mode consists of 10 to 13% (undamaged structure) torsion and the altered torsional mode consists of 11 to 14% (undamaged structure) broadside. The alteration in fundamental broadside shape tends to "point" to Face 4 as the weaker face. For example, failure of member 4530 produces a ratio of Face 4 broadside to Face 1 broadside motion at the deck level of $X_4/X_1 = 1.26$ compared to a value of 0.93 for the undamaged structure.

Alteration of the second and third groups of lateral modes is less consistent among the three selected failure cases than for the fundamental group. The mixed nature of the closely spaced second lateral modes ($f_{l2} = 1.495$ Hz, $f'_{l2} = 1.532$ Hz for the undamaged structure) persists with member failures. Substantial shifts occur in the second torsional mode (f_{t2}) for failures in members 4520 and 4530, with corresponding significant mode shape alteration (ϕ_{t2}). Very pronounced frequency shifts greater than 7% occur in the third broadside mode (f_{b3}) for failures in members 4530 and 4540, while negligible change in that mode occurs for failure of member 4520.

The frequency sensitivity to Face 4 diagonal member failures is well into the measurable sensitivity level (well above the 1% threshold for group 1 in two modes and well above the 2% threshold in at least one higher mode). Moreover, mode shape changes in the fundamental broadside mode appear to "point" in the direction of the face having the failure.

4.5.2 Face A Diagonal Member Failures

The frequency and mode shape sensitivity associated with Face A diagonal member failures, summarized in Table 4-4, is substantially less than that associated with Face 4 diagonal member failures. The fundamental mode group experiences frequency reductions between 0.8 and 2.0% for the end-on and torsional modes. The fundamental broadside mode is virtually insensitive to Face A diagonal member failures since those members contribute negligible strain energy under overall broadside deformation. Fundamental mode shape changes for Face A diagonal in general are not pronounced with the exception of two cases of failures in members 3920 and 3970; the altered fundamental broadside mode includes 42% and 30% end-on motion, respectively, and the altered fundamental end-on mode includes 42% and

Table 4-4. Face A Diagonal Member Failure Modal Sensitivity¹

GROUP 1 MODES

Member	Δf_{b1}	Δf_{e1}	Δf_{t1}	ϕ_{b1}	ϕ_{e1}	ϕ_{t1}
3870 (I) ³	---	-1.0	-0.8	1.00b ₁ , 0.07e ₁	0.07b ₁ , 1.00e ₁	---
3930 (II)	---	-1.7	-1.5	0.99b ₁ , 0.08e ₁	0.08b ₁ , 0.99e ₁	1.00t ₁ , 0.05e ₁
3920 (II)	---	-2.0	-1.9	0.91b ₁ , 0.42e ₁	0.42b ₁ , 0.91e ₁	1.00t ₁ , 0.06e ₁
3970 (III)	---	-2.0	-1.4	0.95b ₁ , 0.30e ₁	0.30b ₁ , 0.95e ₁	1.00t ₁ , 0.05e ₁
3980 (III)	---	-1.2	-1.4	1.00b ₁ , 0.10e ₁	0.10b ₁ , 0.99e ₁	---
3990 (IV)	---	-1.2	-1.1	---	---	---

GROUP 2 MODES

Member	Δf_{l2}	$\Delta f_{l2}'$	Δf_{t2}	ϕ_{l2}	ϕ_{l2}'	ϕ_{b2}
3870 (I)	-1.2	---	-0.5	0.98l ₂ , 0.20l ₂ '	0.20l ₂ , 0.98l ₂ '	0.99t ₂ , 0.06l ₂ , 0.05l ₂ '
3930 (II)	-1.1	---	-0.7	0.96l ₂ , 0.25l ₂ '	0.25l ₂ , 0.97l ₂ '	0.99t ₂ , 0.07l ₂ , 0.07l ₂ '
3920 (II)	-2.2	-0.6	-1.2	0.92l ₂ , 0.35l ₂ '	0.37l ₂ , 0.93l ₂ '	0.98t ₂ , 0.11l ₂ , 0.11l ₂ '
3970 (III)	---	---	---	0.99l ₂ , 0.08l ₂ '	0.08l ₂ , 0.99l ₂ '	---
3980 (III)	---	---	---	---	---	---
3990 (IV)	---	---	---	---	---	---

¹ No entry for a Δf indicates $< 0.5\%$ change; No entry for ϕ indicates < 0.05 contribution of other shapes.

² Box around Δf indicates mode well identified by test.

³ Bays denoted in parentheses.

Table 4-4. Face A Diagonal Member Failure Sensitivity (Cont'd)

GROUP 3 MODES	Member.					
		$\% \Delta f_{t3}$	$\% \Delta f_{e3}$	$\% \Delta f_{b3}$	ϕ_{t3}	ϕ_{e3}
	3870 (I)	---	-0.8	---	---	---
	3930 (II)	---	---	---	---	---
	3920 (II)	-0.6	---	---	---	---
	3970 (III)	-0.5	-2.2	---	---	0.99e ₃ , 0.05t ₃
	3980 (III)	---	-3.2	---	---	---
	3990 (IV)	---	-2.1	---	---	---

30% broadside motion, respectively, for failures in members 3920 and 3970. The fundamental torsional mode shape experiences small change compared to changes associated with Face 4 diagonal failures; the greatest contribution to the torsional stiffness of the platform is associated with Faces 1 and 4 due to their large distances from the center of twist of the overall platform as a beam.

The second mode group experiences frequency sensitivity ranging from 1.1 to 2.2% reduction in the lower lateral mode for failures in members in bays I and II. Shape sensitivity also is present in the closely spaced second lateral mode group pair; however, it is doubtful that such mode shape changes could be exploited for detection since these modes were not well identified from the field data. Failures in members in bays III and IV produce negligible alteration in the second lateral-torsional mode group. The third mode group, in contrast, is relatively insensitive to failures in members in bays I and II, but the third end-on is more sensitive to failures (2.1 - 3.2% frequency reduction, negligible shape sensitivity) for members in bays III and IV.

4.5.3 Face 3 Diagonal Member Failures

Face 3 diagonal member construction differs from that of Faces 4 and A in that an "X" configuration is employed rather than a single diagonal connecting cell corners. The first, second and third mode groups are relatively insensitive to Face 3 diagonal member failures as indicated in Table 4-5 with one exceptional case (member 4800 failure with 2.0% reduction in third broadside mode frequency).

4.5.4 Horizontal Member Failures

With the exception of horizontal member failures in Face 4, the first through third mode group is very insensitive to such failures. In the case of Face 4, the first mode group is virtually insensitive while the second and third mode groups exhibit relatively significant frequency and mode shape sensitivity as indicated in Table 4-6. The second and third torsional modes exhibit the greatest sensitivity in those mode groups. The second torsional mode is lowered in frequency by 6.8% for member 2040 and the third torsional mode by 2.4% for member 2320.

Table 4-5. Face 3 Diagonal Member Failure Modal Sensitivity¹

GROUP 1 MODES - Virtually Insensitive

GROUP 2 MODES

Member	$\% \Delta f_{l_2}$	$\% \Delta f_{l_2}'$	$\% \Delta f_{t_2}^2$	ϕ_{l_2}	ϕ_{l_2}'	ϕ_{t_2}
4770 (II) ³	-0.8	-0.8	---	$0.93l_2, 0.35l_2''$	$0.35l_2, 0.94l_2'$	---
4840 (III)	---	-0.5	---	---	---	---
4880 (IV)	---	---	---	---	---	---

GROUP 3 MODES

Member	$\% \Delta f_{t_3}$	$\% \Delta f_{e_3}$	$\% \Delta f_{b_3}$	ϕ_{t_3}	ϕ_{e_3}	ϕ_{b_3}
4770	---	---	-0.9	---	---	---
4840	---	---	-0.6	---	---	---
4880	---	---	-2.0	---	---	---

¹ No entry for Δf indicates $< 0.5\%$ change;

No entry for ϕ indicates < 0.05 contribution of other shapes.

² Box around Δf indicates well identified by test.

³ Bay denoted in parentheses.

Table 4-6. Face 4 Horizontal Member Failure Modal Sensitivity¹

GROUP 1 MODES - Virtually Insensitive

GROUP 2 MODES

Member	2			
	$\% \Delta f_{l2}$	$\% \Delta f_{l2}'$	$\% \Delta f_{t2}$	ϕ_{t2}
2040	-1.6	-1.9	-6.8	$0.57l_2, 0.52l_2', 0.29t_2$ $0.80l_2, 0.51l_2', 0.16t_2$ $0.16l_2, 0.68l_2', 0.48t_2$
2320	---	---	-1.0	---

GROUP 3 MODES

Member				
	$\% \Delta f_{t3}$	$\% \Delta f_{e3}$	$\% \Delta f_{b3}$	ϕ_{b3}
2040	---	---	---	---
2320	-2.4	---	---	---

¹ No entry for Δf indicates $< 0.5\%$ change;

No entry for ϕ indicates < 0.05 contribution of other shapes.

² Box around Δf indicates mode well identified by test.

4.5.5 Skirt Pile Diagonal Support Member Failures

Failures in two types of skirt pile support member groups are examined. Members 4510 and 3890 serve as diagonal braces on Faces 4 and A, respectively, and members 4750 and 4590 serve as diagonal braces in the planes of Faces 3 and 2, respectively. Failure sensitivities for the above members are indicated in Table 4-7. The Face 4 and A diagonal braces failures produce frequency reductions of 1.8% (first end-on mode) and 2.0% (first broadside mode), respectively. In each case, the respective mode shapes are altered such that greater than 30% of the revised shapes include lateral motion in the orthogonal plane (i.e., member 4510, revised first broadside is 95% original broadside plus 31% original end-on). The Face 2 and 3 failures exhibit significant frequency sensitivity, without mode shape alteration, in the third broadside mode. Unfortunately, the third broadside mode was not identified during the field test of SP-62C.

4.5.6 Vertical Member and Main Pile Failures

Difficulties were encountered in calculation of modal changes with the efficient analytical technique due to poor conditioning of the residual mass matrix, Equation (4-12). It was therefore decided that, for the vertical member failure cases (members 3190, 3560) and for the main pile failure case, revised modal data due to the above failures would be calculated with NASTRAN on the full dynamic model. Classification of modal sensitivities is not as clear nor as quantitative a task as with the efficient technique (Section 4.2).

Lateral and torsional mode sensitivities in the first three lateral mode groups are summarized in Figure 4-4 in terms of deck lateral motions. Failure of member 3190 on the A4 corner produces a dramatic change in the first mode group. Two extra modes are introduced due to the failure and appear to be readily excitable by the wind, wave environment. The frequencies of the new first group modes are 0.622, 0.632, 0.660, 0.674 Hz, and 0.938 Hz. The last mode, fundamental torsion, is virtually identical to the corresponding undamaged structure mode. Additional significant sensitivity is evident in the second and third torsional mode frequencies, which increase by 3% and decrease by 2%, respectively, relative to the undamaged case. Failure of member 3560 results in generally minor changes in frequencies and mode shapes; the largest change occurs in the second lateral mode group with the mode originally at 1.532 Hz reducing to 1.507 Hz (-1.6%).

Table 4-7. Skirt Pile Diagonal Support Member Failure Modal Sensitivity¹

GROUP 1 MODES		2			
MEMBER		$\% \Delta f_{b1}$	$\% \Delta f_{e1}$	$\% \Delta f_{t1}$	
4510 (4) ³		---	-1.8	---	ϕ_{b1}
3890 (A)		-2.0	-0.8	---	ϕ_{e1}
4750 (3)		---	---	---	ϕ_{b1}
4590 (2)		---	---	---	ϕ_{e1}
GROUP 2 MODES		$\% \Delta f_{\rho_2}$	$\% \Delta f_{\rho_2'}$	$\% \Delta f_{t2}$	
MEMBER					ϕ_{t2}
4510		---	---	---	---
3890		---	-0.6	---	$0.18\rho_2, 0.98\rho_2'$
4750		-0.7	-1.1	---	$0.91\rho_2, 0.41\rho_2'$
4590		-0.7	-1.0	---	$0.93\rho_2, 0.36\rho_2'$
GROUP 3 MODES		$\% \Delta f_{t3}$	$\% \Delta f_{e3}$	$\% \Delta f_{b3}$	
MEMBER					ϕ_{b3}
4510		---	---	---	---
3890		---	---	---	---
4750		---	---	-3.5	---
4590		---	---	-2.8	---

¹ No entry for Δf indicates $< 0.5\%$ change; no entry for ρ indicates < 0.05 contribution of other shapes.

² Box around Δf indicates mode well identified by test.

³ Face denoted in parentheses.

DESCRIPTION	UNDAMAGED	MEMBER 3190 FAILURE	MEMBER 3560 FAILURE	A4 MAIN PILE FAILURE
		0.622		
		0.632		
FIRST BROADSIDE	0.639 Hz	0.660	0.638	0.609 (-4.7%)
FIRST END-ON	0.659 Hz	0.674	0.657	0.651 (-1.2%)
FIRST TORSION	0.935 Hz	0.938	0.928	0.930
SECOND LATERAL	1.495 Hz	1.480 (-1.0%)	1.496	1.493
SECOND LATERAL	1.532	1.518 (-1.0%)	1.507 (-1.6%)	1.525
SECOND TORSION	1.686	1.739 (+3.0%)	1.687	1.686
THIRD TORSION	2.002	1.961 (-2.0%)	2.002	2.002
THIRD END-ON	2.434	2.420	2.420	2.43
THIRD BROADSIDE	2.678	2.656 (-0.8%)	2.658	2.677

Figure 4-4. Vertical Member Failure Modal Sensitivity

Failure of the A4 main pile results in significant changes in the fundamental broadside and end-on modes as illustrated in Figure 4-4. The 4.7% reduction in the fundamental broadside mode is the most major change. The second and third lateral-torsion mode groups are virtually unchanged due to the subject pile failure.

4.5.7 Summary of Sensitivities and Detectability Judgments

The frequency sensitivity results are summarized by member category in Table 4-8 showing minimum-maximum percentage changes in the modes of first three groups. Judgments of detectability (from likely to impossible) are shown at the bottom of the table based upon the relationship of the magnitudes of the changes in modes well identified in field test to the 1% and 2% thresholds, giving credit to the existence of multiple modes with detectable frequency change.

4.6 MODAL SENSITIVITY AND LOAD PATH ALTERATION

The evaluation of changes in the first three mode groups resulting from single member failures produces a mixed set of sensitivities dependent on member redundancy, orientation and location. Correlation of mode sensitivity levels with structural configuration and correlation of mode sensitivity levels with member load redistribution are two fundamental issues which must be addressed to place results from SP-62C in proper perspective. Moreover, categorization of SP-62C with respect to simpler platform designs typical of North Sea structures as well as larger, more redundant platforms is quite desirable. In order to effectively accomplish the above correlations, simplified models are employed to establish trends.

4.6.1 Frequency Sensitivity of the Fundamental Mode Group

The fundamental mode group behavior of a typical platform is assumed to be that of a multi-bay shear beam with mass concentrated at the upper end, as illustrated in Figure 4-5. The lateral flexibility of such a structure is due to flexibility of the trusswork, the foundation, and the relatively soft section immediately below the deck level. Assuming a rectangular configuration (batter neglected), the shear flexibility of a typical bay is estimated to be

$$C = \frac{1}{nk} \quad \text{-(4-22)}$$

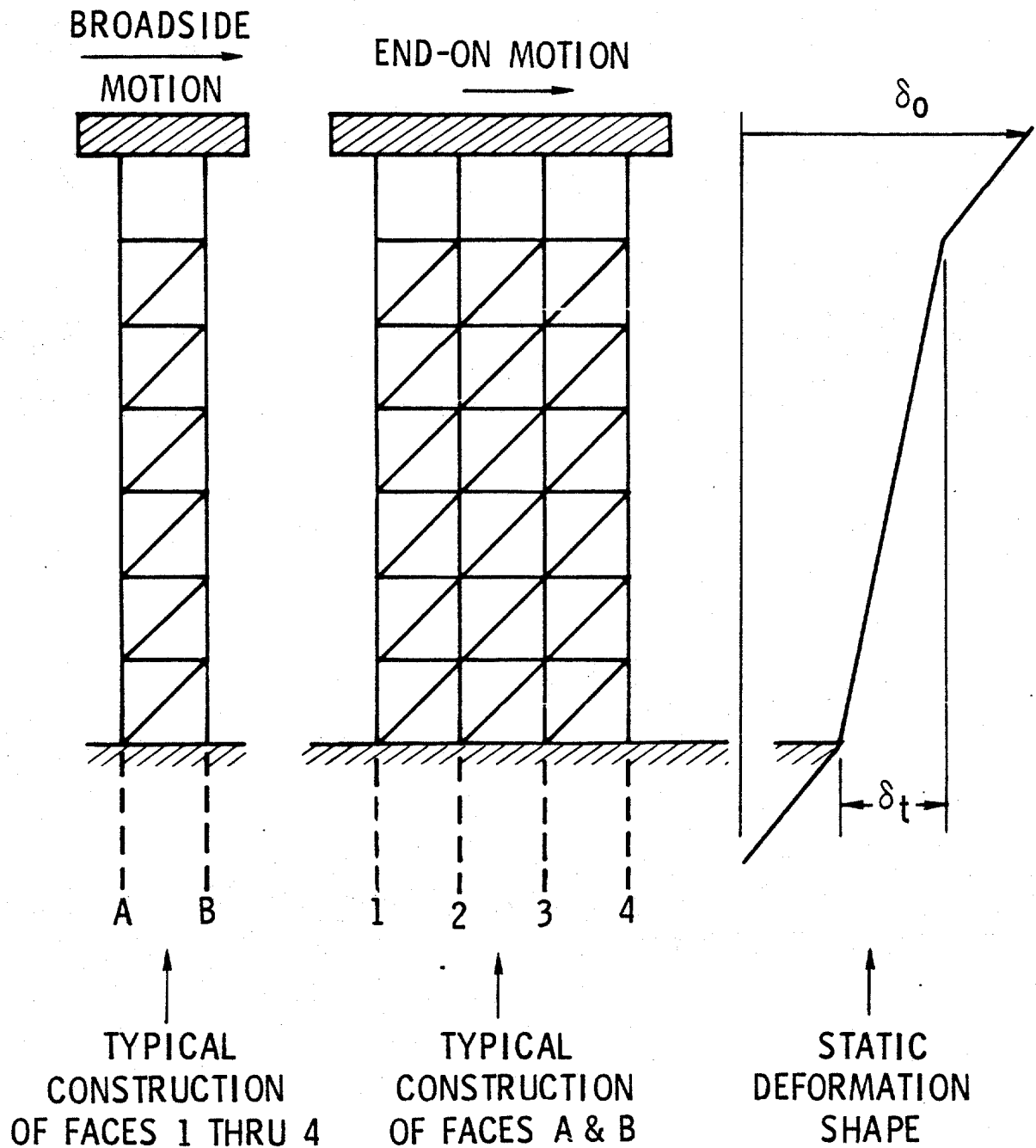
Table 4-8. First Three Mode Groups: Summary of Frequency Changes
by Failure Class and Judgment of Detectability

Mode	Freq (Hz)	Vertical Diagonal Members					Main		Horizontal		
		Face 4	Face A Bays I, II	Face A Bays III, IV	Face 3	Skirt Pile Support Face 4, A Face 2, 3	A4	A3	Main Pile A4	Face 4	Others
1 (b1)	0.639	-2.8/-3.6	-1.0/-2.0	-1.2/-2.0		/-2.0			-4.7		
2 (e1)	0.659		-0.8/-1.9	-1.1/-1.4		/-1.8			-1.2		
3 (t1)	0.935	-4.8/-6.7	-1.2/-2.2		/-0.8						
4	1.50	/-2.7			/-0.8						
5	1.53	/-1.8	/-0.6					-1.0			
6 (t2)	1.69	-1.4/-4.7	-0.5/-1.2					-1.0			
11 (t3)	2.00	-0.9/-2.7	/-0.6					+3.0		-1.0/-6.8	
12 (e3)	2.43	/-0.6	/-0.8	-2.1/-3.2				-2.0		0/-2.4	
13 (b3)	2.68	/-7.7			-0.6/-2.0			-0.8			
Detectability Judgment		Likely	Marginal/ Probable	Probable	Unlikely	Likely	Unlikely	Pro- bable	Unli- kely	Marginal/ Likely	Impossible

¹Entry -2.8/-3.6 indicates range from 2.8% to 3.6% reduction in frequency. No entry indicates less than 0.5% change.

²Arrows indicate modes well identified from field test.

³Two additional modes at 0.622 and 0.632 Hz may aid detection.



$n = 6$ (end-on), 4 (broadside), $\sim 2 +$ (torsion)

$$(1+\gamma) = \delta_o / \delta_t, \quad p = 6, \quad p_e = 6(1+\gamma)$$

Figure 4-5. Typical Idealized Platform for Mode/Load Sensitivity Evaluation

where k is the stiffness associated with each diagonal member and n is the number of effective diagonal members in the bay. Vertical members corresponding to main legs are assumed axially rigid and the stiffness contribution of horizontal members is neglected. The total lateral flexibility for "p" bays,

$$C_t = \frac{p}{nk} \quad (4-23)$$

The additional flexibility due to foundation and shear compliance of the upper section is expressed as a factor, γ , times the compliance of the p bays,

$$C_s = \gamma C_t \quad (4-24)$$

The estimated overall lateral flexibility is, therefore

$$C_o = C_t + C_s = \frac{(1 + \gamma)p}{nk} \quad (4-25)$$

where the constant, $1 + \gamma$, is readily estimated as the ratio of total deck displacement to the shear deflection of all truss bays (Figure 4-5). It is convenient to refer to the numerator quantity $(1 + \gamma)p$ as an "effective" number of bays, p_e . Denoting the total mass of the decks as M , the fundamental lateral frequency estimate of this equivalent structure is

$$f_o = \frac{1}{2\pi} \sqrt{\frac{nk}{Mp_e}} \quad (4-26)$$

It should be noted that for a fundamental torsional mode, M would correspond to mass moment of inertia and the constant n would correspond to the effective number of members deforming under torsional motion.

If a single diagonal member in any bay is severed, the overall flexibility may be expressed as

$$C_o' = \frac{p_e - 1}{nk} + \frac{1}{(n-1)k} \quad (4-27)$$

resulting in a damaged structure frequency estimate of

$$f_d = \frac{1}{2\pi} \sqrt{\frac{n(n-1)k}{M [1 + (n-1)p_e]}} \quad (4-28)$$

The fractional change in fundamental frequency is, therefore

$$\begin{aligned} \frac{\Delta f}{f_o} &= \frac{f_d - f_o}{f_o} = \sqrt{\frac{1}{1 + \frac{1}{(n-1)p_e}}} - 1 \\ &\approx -\frac{1}{2(n-1)p_e} \text{ for } (n-1)p_e \gg 1 \end{aligned} \quad (4-29)$$

Where the term $1/(n-1)p_e$ expresses the fractional increase in overall compliance produced by the failure. The result implies the following:

- (a) frequency sensitivity is inversely proportional to the number of effective members remaining in a bay after damage.
- (b) although the total shear load due to deck acceleration is carried equally by all bays, frequency sensitivity is inversely proportional to the number of the effective stories, p_e .
- (c) soft foundation and below deck shear flexibilities tend to increase the effective number of stories and thereby decrease frequency sensitivity.

It is finally noted that the above observations apply to diagonal member failures which are believed to be the most significant in practice. Horizontal members are assumed in general to be less significant than diagonals. Vertical members are assumed to be less likely to fail.

4.6.2 Sensitivity of Simplified Platform Structures

The above discussion addresses the general question of fundamental mode frequency sensitivity for a wide class of shear beam structures. While a simple approximate relationship between frequency sensitivity, structural redundancy and effective number of stories is established, Equation (4-29), frequency sensitivity associated with mode shape alteration (end-on, broadside, torsion coupling due to damage) and member load sensitivity remain to be examined. This section deals with finding trends for these matters by analyzing simple models of platform type structures.

Consider shear beam structures typically configured as that illustrated in Figure 4-5. Let each "floor" composed of horizontal members be considered rigid and massless. All lateral and torsional compliance is assumed to be due to diagonal members only. Since the structural mass is assumed concentrated at the deck level, each typical structure is described dynamically with three degrees of freedom, namely two lateral displacements and one torsional rotation. In order to establish the distribution of member load, static lateral loadings are applied at the top.

The procedure employed is as follows:

- (a) Define the inter-deck shear and torsional stiffness of a typical bay configuration (Figure 4-6):

$$\begin{bmatrix} k_{xx} & k_{xy} & k_{x\theta} \\ k_{yx} & k_{yy} & k_{y\theta} \\ k_{\theta x} & k_{\theta y} & k_{\theta\theta} \end{bmatrix} \begin{Bmatrix} \delta_x \\ \delta_y \\ \delta_\theta \end{Bmatrix} = \begin{Bmatrix} F_x \\ F_y \\ M_\theta \end{Bmatrix} \quad (4-30a)$$

or in matrix shorthand

$$K_{\text{bay}} \delta_{\text{bay}} = F \quad (4-30b)$$

where K_{bay} is diagonal for a symmetric structure (assumed so in the absence of damage).

- (b) Define the total lateral-torsional flexibility of the structure as

$$C_t = \sum_{i=1}^{P_e} (K_{\text{bay}})_i^{-1} \quad (4-31)$$

- (c) With the assumption of a symmetric deck mass distribution, calculate the fundamental modes of

$$\begin{bmatrix} C_t \end{bmatrix} \begin{bmatrix} M & & \\ & M & \\ & & MR^2 \end{bmatrix} \begin{Bmatrix} \ddot{X} \\ \ddot{Y} \\ \ddot{\theta} \end{Bmatrix} + \begin{Bmatrix} X \\ Y \\ \theta \end{Bmatrix} = \begin{Bmatrix} 0 \\ 0 \\ 0 \end{Bmatrix} \quad (4-32)$$

where R is the deck radius of gyration.

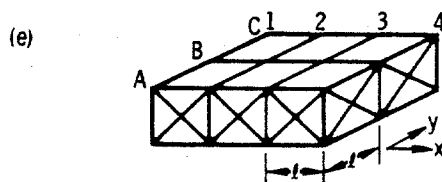
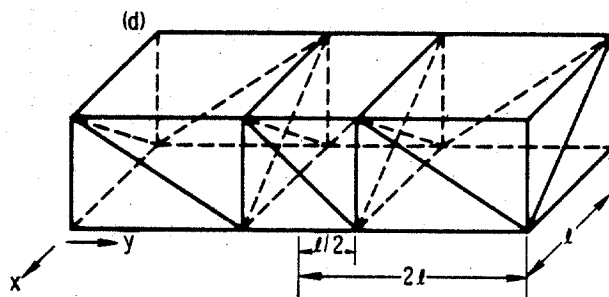
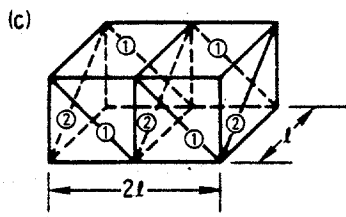
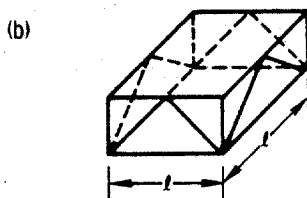
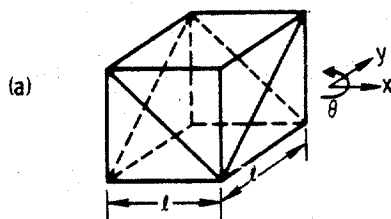
- (d) Perform steps (a) through (c) for the undamaged and damaged structure for all damage configurations of interest and establish frequency sensitivity.
- (e) Noting that lateral loading is equally transmitted to all bays, calculate the undamaged bay static deformations δ_x , δ_y , δ_θ due to unit loads F_x and F_y separately. Establish individual member loads associated with the deformation pattern.
- (f) Repeat step (e) for the bay which has sustained damage and establish the greatest member loading change with respect to the undamaged condition.

The series of structures illustrated in Figure 4-6 have been evaluated by the above technique. The chosen configurations range in complexity from relatively simple ones (North Sea, and Buzzard's Bay (19) and Ambrose (20) types) to the SP-62C and Cognac types. The results of the general evaluation are: (a) Figure 4-7 which illustrates a relationship between frequency sensitivity and fractional compliance increase parameter $1/(n-1)p_e$ and (b) Figure 4-8 which illustrates a general relationship between normalized load sensitivity for elastic behavior and frequency sensitivity. In both cases scattering of data (relative to at least squares linear fit) occurs since the sensitivities are dependent on geometry of the subject bays as well as the compliance parameter $1/(n-1)p_e$. The result of applying Equation (4-29) is shown on Figure 4-7 and labeled "simple model."

The frequency versus compliance parameter relationship presented in Figure 4-7 includes actual complete mathematical model results for the present SP-62C, Buzzard's Bay Tower (19), and Ambrose Tower (20). It should be noted that the soft mud stiffness and long sections of non-braced legs for the Ambrose Tower produce a relatively large number of effective stories ($p_e \approx 20$) determined on the basis of a modal deflection curve presented in Reference 20.

On the assumption that 1.0% frequency sensitivity is an optimistic detection threshold for the fundamental mode group, it appears unlikely that most member failures would be detectable for the Cognac class of platforms on the basis of fundamental frequency data (Figure 4-7 shows $<1\%$ change for the "Cognac type" model structure). On the other extreme, much less redundant platforms (such as typical North Sea structures) appear to be generally more sensitive (above 2% frequency

BAY CONFIGURATION



STRUCTURE CHARACTERISTICS

MODEL A

LATERAL STIFFNESS, k FOR ALL MEMBERS

$$n_x = 2, n_y = 2, n_\theta = 4$$

ANALYSIS OF $p_e = 2, 3, 4$ BAY STRUCTURES

$$R^2 = 0.667$$

MODEL B

LATERAL STIFFNESS, k FOR ALL MEMBERS

$$n_x = 4, n_y = 4, n_\theta = 8$$

ANALYSIS OF $p_e = 2, 4$ BAY STRUCTURES

$$R^2 = 0.667$$

MODEL C

LATERAL STIFFNESS, $0.667 k$ FOR MEMBERS ①

LATERAL STIFFNESS, k FOR MEMBERS ②

$$n_x = 4, n_y = 3, n_\theta \approx 3$$

$$p_e = 4$$

$$R^2 = 0.917$$

"SP-62C TYPE"

LATERAL STIFFNESS, k FOR ALL MEMBERS
(crossed face 2, 3 members total to $2k$ each)

$$n_x = 6, n_y = 6, n_\theta \approx 3$$

$$p_e = 6$$

$$R^2 = 0.819$$

"COGNAC TYPE"

LATERAL STIFFNESS, k FOR ALL MEMBERS
FACE A, C ALIKE, FACES 1-4 IDENTICAL

$$n_x = 12, n_y = 16, n_\theta \approx 12$$

ANALYSIS OF $p_e = 12, 20$ BAY STRUCTURES

$$R^2 = 0.819$$

Figure 4-6. Description of Structural Configurations Used for Sensitivity Studies

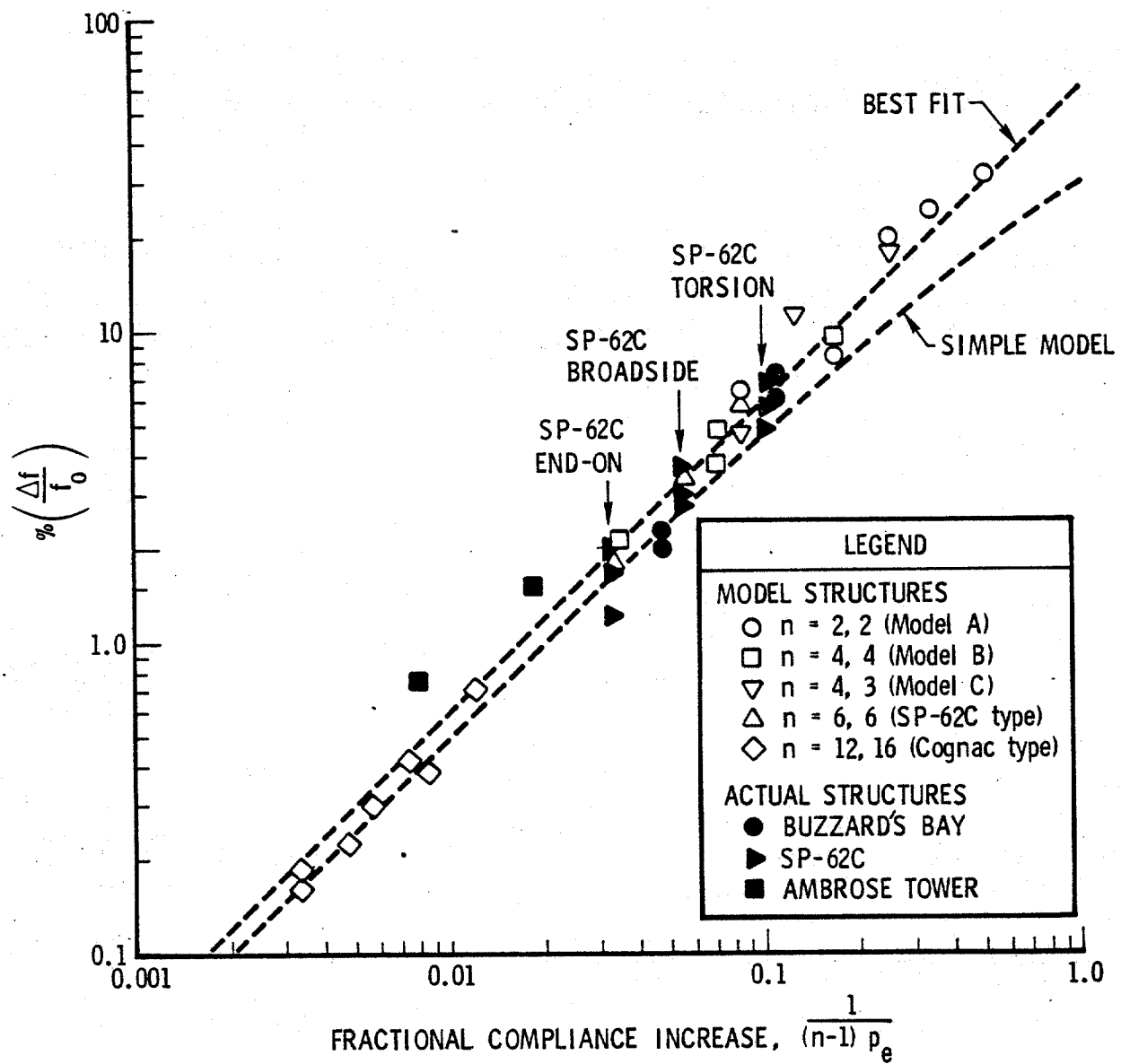


Figure 4-7. Frequency Sensitivity of Fundamental Mode Group for Failure of a Single Diagonal Member

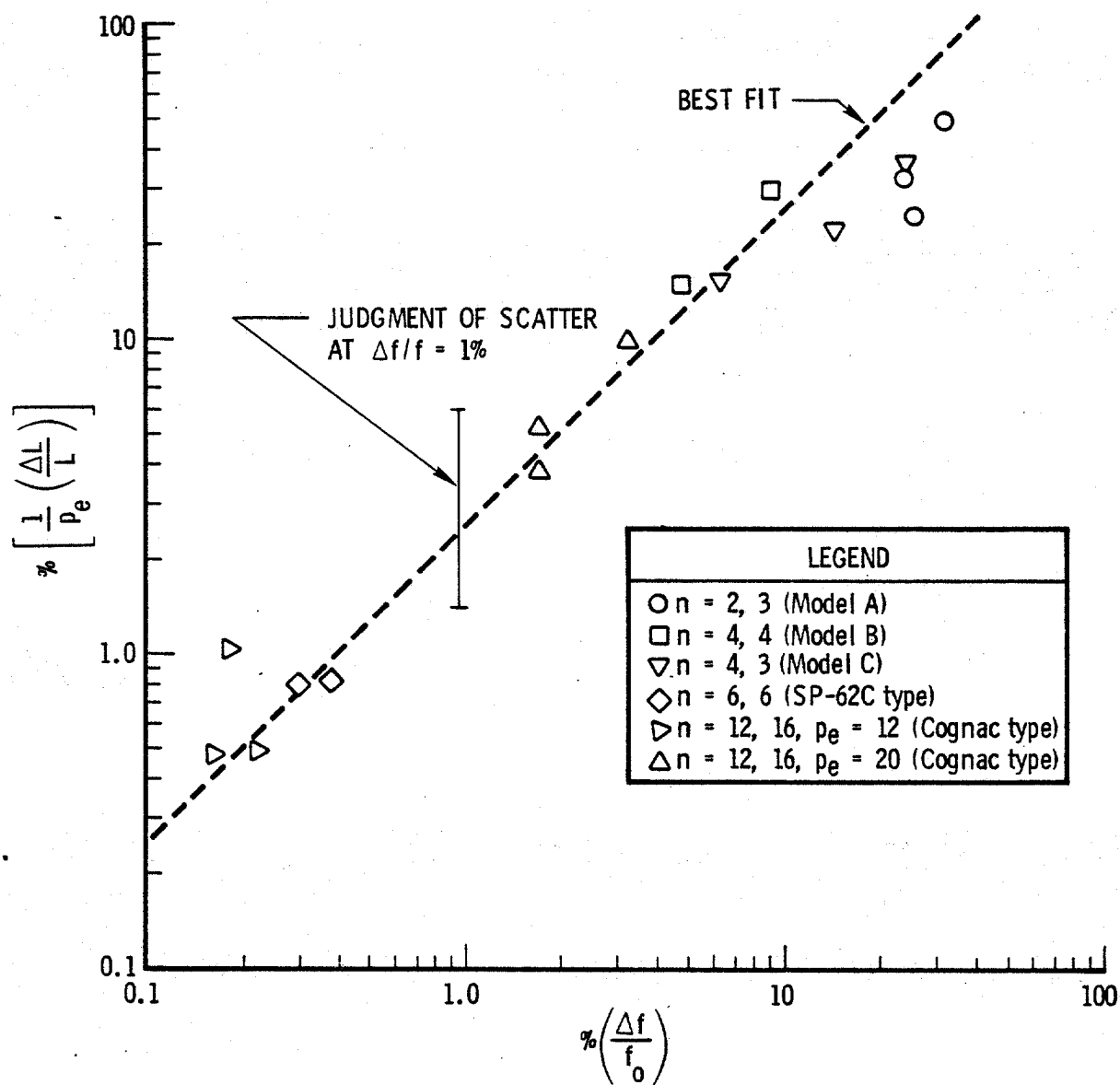


Figure 4-8. Simplified Model Load Sensitivity for Failure of a Single Diagonal Member

shifts), in agreement with reports for North Sea structures (6). Finally, it is of interest to note that results for the simplified platform resembling SP-62C fall close to the sensitivity levels associated with the complete model. This fact adds confidence to the estimated trends indicated above.

The normalized load versus frequency sensitivity relationship indicated in Figure 4-8 must be carefully interpreted since the number of effective stories is employed as a normalizing factor. For example, the point $(\Delta L/L)p_e = 1\%$ for the Cognac type of structure with $p_e = 20$ translates to a 20% load sensitivity associated with about a 0.2% frequency change. As intuitively expected from shear beam behavior, load sensitivity is principally a function of individual bay redundancy and is relatively insensitive to the number of stories since total lateral loads are transmitted equally to all bays. Frequency sensitivity, however, is strongly influenced by both number of bays and individual bay redundancy. Employing the best fit load versus frequency sensitivity line, one may estimate relative structural significance/frequency sensitivity levels for various structures. Definite judgments on structural significance thresholds are not appropriate here since design safety factors are unknown and safety philosophy is established by the operator.

The relationships developed for frequency sensitivity versus member participation (Figure 4-7) and normalized load sensitivity versus frequency sensitivity (Figure 4-8) can be extended to apply to multiple member failure configurations. Multiple member failure participation may be expressed in terms of the compliance participation parameter $m/(n-m)p_e$, where m denotes the number of failed members in a particular bay; it is presently assumed that the general relationship in Figure 4-7 is valid when the abscissa is interpreted as $m/(n-m)p_e$ rather than indicated in the graph for $m = 1$. If 1% frequency change is taken as the threshold for detection, failures contributing 1.2 to 2.5% or more to the overall compliance are detectable.

For the SP-62C class of platform, $p_e \approx 6$ and $n = 6$, yielding the result that one failure should be detectable (for diagonals not in an "x" configuration). This agrees with the results on SP-62C. For the Cognac class of platform, $p_e = 12$ to 20 and $n = 12$ or 16, yielding the result that 2 to 5 members must fail in a bay to be detectable.

The normalized member load increase $(\Delta L/L)/p_e$ is assumed to bear the approximate relationship with frequency sensitivity indicated in Figure 4-8. A 1% threshold for detectable frequency change corresponds to a normalized load sensitivity range of $0.013 \leq (\Delta L/L)/p_e \leq 0.06$ based upon an engineering judgment of the scatter of results on Figure 4-8. For SP-62C with $p_e \approx 6$ bays, the marginal frequency change threshold implies critical member load changes roughly between 8% and 36%. For the Cognac class of platform with $p_e = 12$ to 20, the marginal frequency change threshold implies critical member load changes roughly between 26% and 120%, which are quite large relative to SP-62C.

Gulf of Mexico platforms are subject only to winter storms as the worst environment while manned. It has been stated (12) that winter storm loads provide no more than 40% of the hurricane design loads. Thus, for SP-62C, the fact that the frequency threshold permits detection of failures producing no more than a 36% load increase (implies maximum load reaches 0.4 times 1.36 or 0.54 of design load) is significant and encouraging for the monitoring concept for this structure. Similarly, the fact that load changes up to 120% may occur in a marginally detectable situation for Cognac type platforms leads to a possible reaching of 0.88 of design load. While there is some hope for useful monitoring of a Cognac type platform, the task is evidently considerably more demanding than for a smaller platform.

It should be restated, at this point, that all of the above sensitivity and structural significance observations are limited to the fundamental mode group and to diagonal brace members. One may speculate, however, that the trends will also hold for horizontal and vertical member failures.

4.7 HIGHER MODE SENSITIVITY

The sensitivity of analytical vibration modes beyond the first three fundamental mode groups is now examined. It should initially be emphasized that the calculated higher modes do not necessarily correspond to measured data. However, study of analytical data is believed to provide some insight into the potential utility of higher mode sensitivity to member failures.

A summary of wide frequency range modal frequency sensitivity is presented in Table 4-9 for typical member failure configurations; frequency changes in excess of 0.5% are noted for modes 1 through 25. In general it is seen that while frequency sensitivity is prominent for several failure categories, a frequency sensitivity in the higher modes covering all types of failures is not present. Pronounced

Table 4-9. Wide Frequency Range Modal Frequency Sensitivity

No.	Nom. Freq. (Hz)	VERTICAL DIAGONAL MEMBERS				VERTICAL MEMBERS		HORIZONTAL MEMBERS			
		Face 4	Face A	Face 3	Skirt Pile Support	Face A	A4 Main Pile	Face 4	Face A	Face 3	Face 3-4
		4530	3980	4840	4510	3560	7	2320	2030	2180	2160
1	.639	-3.6					-4.7	-1.2			
2	.659	-1.2			-1.8	-0.6					
3	.935	-6.7	-1.4								
4	1.495										
5	1.532	-0.9				-1.6		-1.0			
6	1.686	-3.6									
7	1.852										
8	1.881										
9	1.895										
10	1.922										
11	2.002	-2.7						-2.4*			
12	2.434	-3.2				-0.6					
13	2.678	-6.9				-0.7					
14	3.079	-7.7	-2.2	-2.9		-0.6		+1.5	-1.4	-0.7	-6.7
15	3.133	-1.6									
16	3.135		-0.8								
17	3.282										
18	3.529										
19	3.711										
20	3.810	-2.0		-1.1		-0.8					
21	3.973	-2.5									
22	4.128										
23	4.183										
24	4.366					-0.6		+1.2	-1.0		-1.2**
25	4.547					-0.6			-2.3		-6.8**

* ADDITIONAL MODE AT 2.196 Hz

** GROUP IS COUPLED COMBINATION OF NOMINAL MODES 18, 19, 20

frequency sensitivity in the higher modes does not necessarily indicate greater significance of specific member failures, principally because an evaluation of that point has not been made in this study.

A summary of wide frequency mode shape sensitivity is presented in Table 4-10 for the same failure categories denoted in Table 4-9. The criterion for denoting a mode shape as sensitive is a greater than 10% participation of undamaged neighboring modes in the damaged structure shape in question (see Section 4.3). It is noted that shape alteration appears more abundant than frequency alteration in the higher modes. In view of considerations discussed in Section 4.4, mode shape sensitivity measurement may require reliance on accelerometers very close to or slightly below the water line.

One theoretical mode stands out as being shape sensitive to all failure classes, namely mode 14 which is the first truss cross-section warping mode. This mode illustrated in Figure 4-9 and in Appendix B (Figure B-14) is of particular interest since the decks are relatively motionless rendering the mode insensitive to deck mass loading changes. A summary of sensitivities for this mode is presented in Table 4-11. The selected shape parameter is the ratio of the broadside lateral deflection between the A4 and A1 legs at the 14 ft (4.3 m) level. Note that only two cases, both horizontal member failures, produce under a 20% change in this shape parameter. Recall that the 20% change is the value for a detection threshold assumed in Section 4.3. Note also the lack of correspondence between frequency and shape changes. Further, it is emphasized that an ability to detect this mode from ambient vibration has not been established.

Table 4-10. Wide Frequency Range Mode Shape Sensitivity
(Greater than 10% participation of other modes denoted)

No.		Nom. Freq. (Hz)	VERTICAL DIAGONAL MEMBERS					VERTICAL MEMBERS		HORIZONTAL MEMBERS				
			Face 4	Face A	Face 3	Skirt Pile Support	Face A	A4 Main Pile	Face 4	Face A	Face 3	Face 3-4		
			4530	3980	4840	4510	3560*	7		2320	2030	2180	2160	
1		.639	x	x		x		x						
2		.659		x		x		x						
3		.935	x											
4		1.495	x											
5		1.532	x											
6		1.686	x											
7		1.852												
8		1.881	x	x							x	x	x	
9		1.895	x	x							x	x	x	
10		1.922	x	x						x				
11		2.002	x											
12		2.434	x							x	x			
13		2.678	x							x				
14		3.079	x	x				x		x	x	x	x	
15		3.133	x	x				x		x				
16		3.135	x	x				x		x				
17		3.282		x				x						
18		3.529		x				x						
19		3.711						x						
20		3.810						x						
21		3.973						x						
22		4.128	x					x						
23		4.183		x				x						
24		4.366	x	x							x			
25		4.547	x	x				x			x			

* ADDITIONAL MODE AT 2.196 Hz

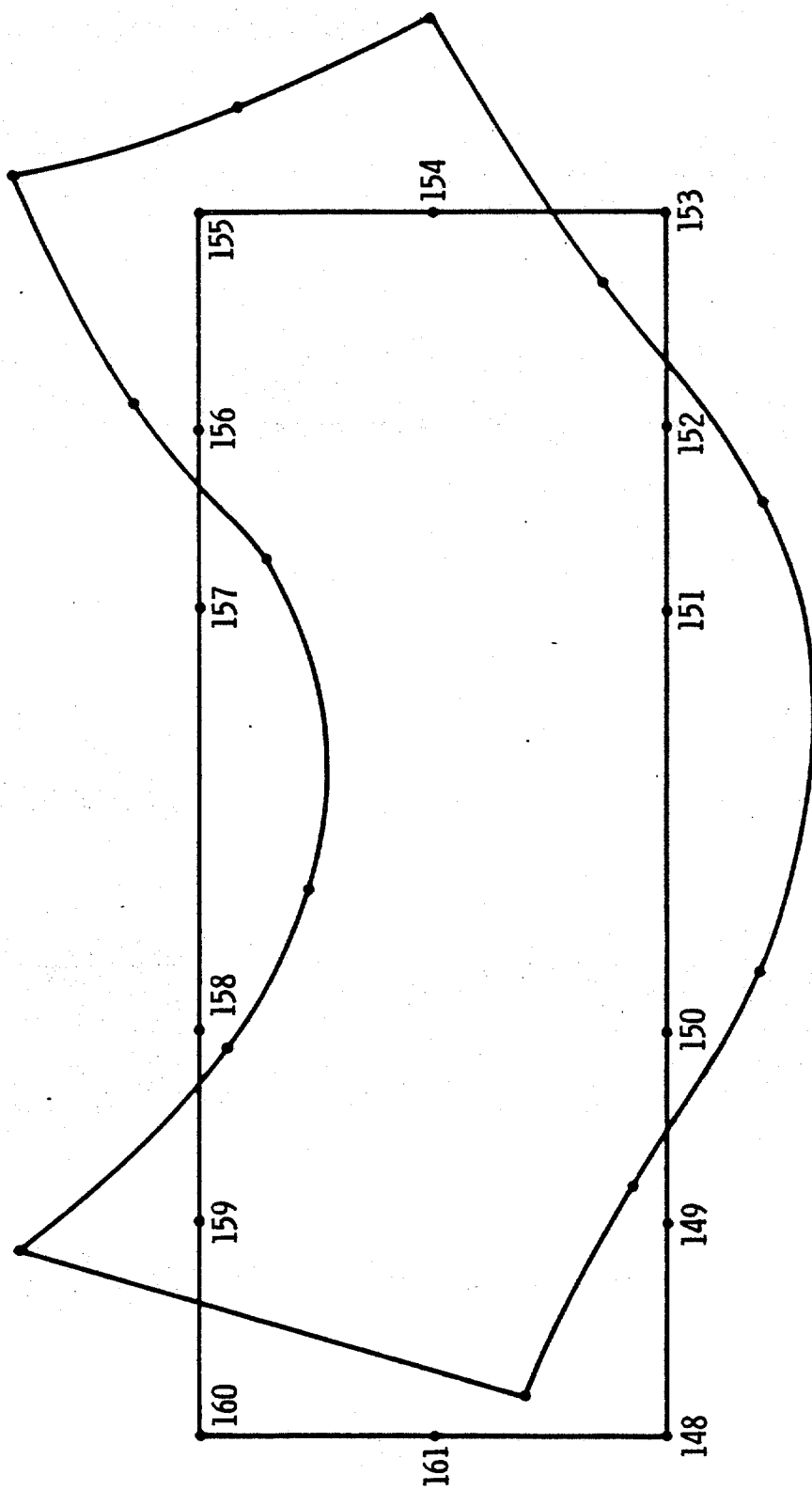


Figure 4-9. Illustration of Cross-Sectional Shape
of Warping Mode at 14 Feet (4.3 m) Level

Table 4-11. Summary of Cross Section Warping Mode Sensitivity

FAILURE CLASS	FAILED MEMBER	SHAPE PARAMETER*	%CHANGE IN SHAPE PARAMETER	% CHANGE IN f
VERTICAL DIAGONALS	4530	0.16	- 88	-7.7
	3980	3.79	+191	-2.2
	4840	0.86	- 34	-2.9
	4510	0.69	- 47	0
VERTICALS	3560	1.85	+ 42	0
	7	0.98	- 25	0
HORIZONTALS	2320	0.65	- 50	0
	2030	0.00	-100	0
	2180	1.12	- 16	-0.7
	2160	1.46	+ 12	0

* Broadside lateral deflection ratio (X_4/X_1) at corners, 14 ft (4.3 m) level

Nominal value = 1.30

5. EVALUATION OF PROTOTYPE SYSTEM

5. EVALUATION OF PROTOTYPE SYSTEM

The system is intended to implement the conventional approach of ambient vibration monitoring. By this is meant the detection of the frequencies and shapes of the fundamental mode group, and of as many of the second and third group modes as can readily be extracted from the data. A series of field tests of a prototype system is recommended to provide the operational experience necessary to optimize the data acquisition and interpretation for an efficient operational capability. In general terms an instrumentation system is described, a method for analyzing the data is recommended, and requirements for field testing are outlined.

5.1 DESCRIPTION OF INSTRUMENTATION SYSTEM

This section contains a general description of the elements of a prototype system. Examples of candidate equipment are listed in Table 5-1. The detailed design of an actual system has not been carried out.

Six accelerometers (plus spares) are required. At this time it appears that accelerometers of the force balance type (also called servo rebalanced) are most suitable. However, the suitability of low g, high gain piezoelectric accelerometers having integral preamplifiers deserves investigation. The specific accelerometer and cable for a prototype system should be selected after detailed evaluation of their operating specifications, including laboratory or field evaluation. A partial listing of operating specifications for the accelerometer/cable combination is

Full-scale range:	$\geq 0.1 \text{ g}$
Scale factor:	$\geq 2 \text{ v/g}$ stable within 1%
Frequency range (3db):	0.2 to 5 Hz minimum
Noise (0.2 to 5Hz):	$\leq 0.1 \mu\text{g}^2/\text{Hz}$
Cross-axis sensitivity:	≤ 0.01

Insensitivity to temperature fluctuations and to electromagnetic disturbances, mechanical ruggedness, and water tightness are also important characteristics. The outline of a candidate accelerometer for this application is shown in Figure

TABLE 5-1. Examples Of Candidate Equipment for Prototype System

EQUIPMENT	NUMBER REQUIRED	SIZE (each) in. (cm)	WEIGHT (each) lb (kg)
Accelerometer: Sunstrand QA 1300	6	1.2 X 1.2 X 1.5 (2.9 X 2.9 X 3.8)	0.2 (0.1)
Signal Conditioner: Kinometrics SC-1 (4 channel)	2	16 X 10 X 11 ½ (41 X 25 X 29)	20 (9)
Analog FM Tape Recorder: HP 3968A (8 track, ¼ in.)	1	17½ X 16.8 X 10.1 (44.5 X 42.7 X 25.6)	69 (31.3)
Digital Data Acquisition System: ¹ Kinometrics DDS-1103			
Data Module	1	19 X 12½ X 21 (48 X 32 X 54)	50 (23)
Tape Transport Reel - 7 in. (18cm)	1	19 X 8 ¾ X 7½ (48 X 22 X 19)	25 (11)
FFT Spectrum Analyzer: HP 5420A (dual channel) ²	1	25¼ X 16 ¾ X 16 (64 X 43½ X 40½)	115 (52)

¹ Alternative to analog recorder.

² Subdivided into 3 chassis.

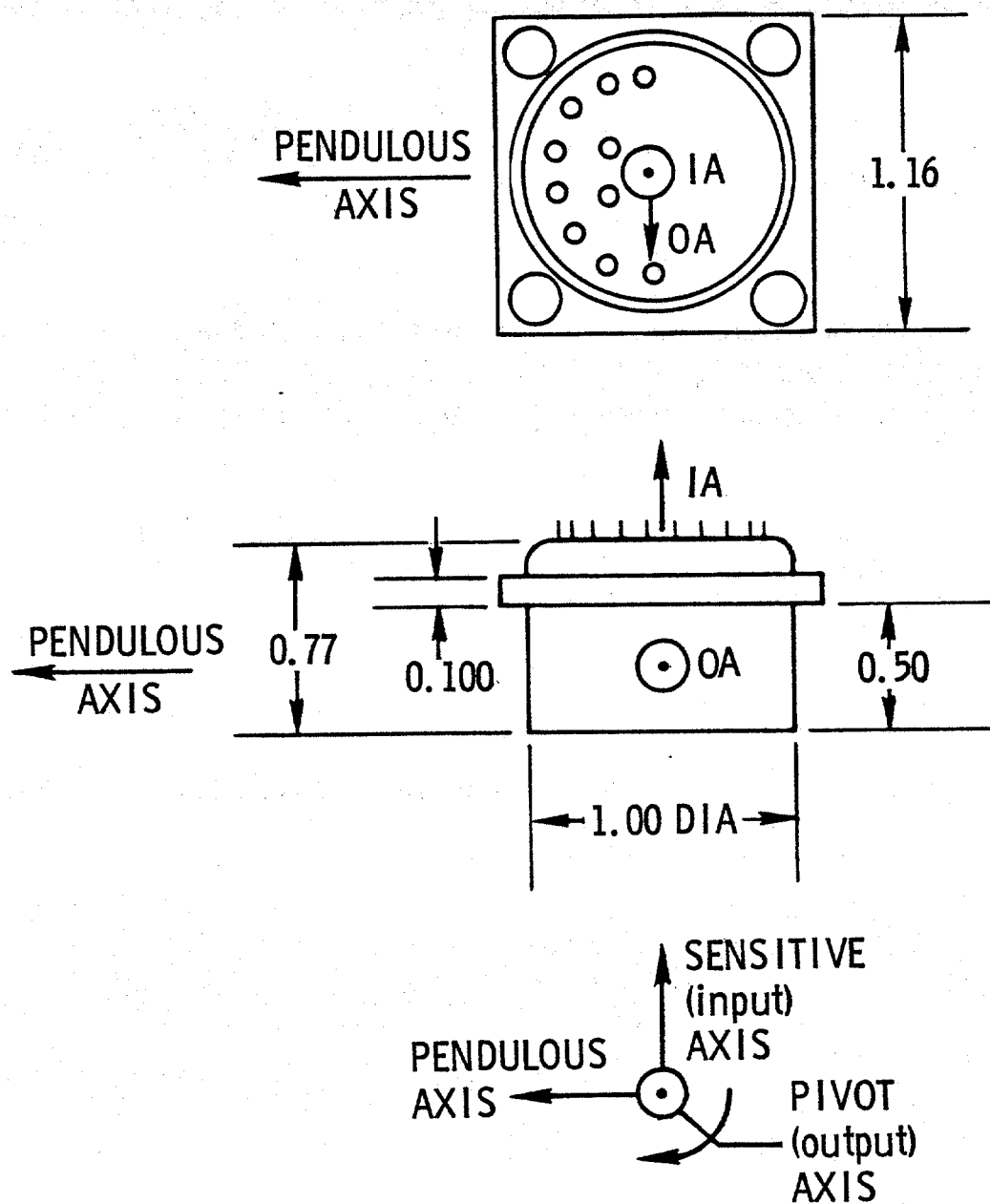


Figure 5-1. Sunstrand QA 1300 Accelerometer

5-1. A somewhat larger version having an integral connector would be required.

Six fixtures for mounting of the accelerometers should be available. Each fixture should have the capability to carry three accelerometers, one along each of three mutually perpendicular axes. The fixtures should have provision to permit mechanical clamping to the circumference of a main leg. A possibility for the clamping is by means of a circumferential strap, wire or chain and an adjustable spring tensioning device. No adhesive bond at the fixture/leg interface is needed. The fixture should have provision for three-point contact with a leg, with adjustability to permit angular alignment with the three principal directions of the platform. As a goal, the alignment should be made to within 0.5 deg or less.

The accelerometer signal conditioning should provide for low-noise amplification, DC rejection (if necessary), and low-pass filtering. The amplification should be adjustable in increments of 6 db or less to enable effective utilization of the full recording range. The cutoff of the low-pass filtering should be adjustable in at least 1 Hz increments from 1 to 5 Hz and the roll off should be 18 db/octave or higher.

At least six channels of FM analog tape recording should be available in addition to a channel for the carrier signal to be used for tape speed control on playback. The signal/noise ratio (S/N) for discrete (periodic) noise should be at least 60 db over the frequency range within which the modes exist, typically from 0.2 to 4 Hz. In the absence of sufficient prewhitening of the data (that is, filtering to reduce its dynamic range), the S/N requirement may be met by operation of the recorder at a sufficiently high speed to avoid capstan induced or other periodic noise in the frequency range (see Figure 2-5).

Alternatively, a digital data acquisition system with a least six-channel input capability can be employed. At least 12 bit analog-to-digital conversion is required. The minimum data rate should be at least 600 samples per second. Digital-to-analog playback of data from the system is required.

A dual-channel FFT spectrum analyzer is required. It should be capable of analyzing with a least a 256-line resolution over a frequency range from zero up to a variable upper frequency between 1 and 100 Hz. Provision for storage of the spectra is required, either by use of a digital data recorder, or a digital plotter. The analyzer identified in Table 5-1 has a built-in cassette recorder for storage of up to 120 records (any measured or computed function) on each tape cartridge.

5.2

DATA ANALYSIS METHOD

The acceleration data are to be analyzed by computing autospectra to identify modal frequencies and by computing the transfer function between one measurement and another, for as many pairs of measurements as are necessary, to define mode shapes (Section 2.5). The transfer function gives the amplitude and phase relationship as a function of frequency between the two signals. The transfer function is defined as the ratio of cross-power spectrum and the auto-spectrum of the reference. The coherence function, a figure of merit for the transfer function measurement, is also determined.

An FFT spectrum analyzer is recommended for obtaining transfer functions in real time during the data collection process. Such an analyzer provides a digital implementation of the Fast Fourier Transform. By sufficient averaging of transforms of individual random data records, statistically meaningful transfer functions are determined.

Additional analysis can be conducted onshore later using the recorded data. This analysis can be conducted either by using a real time analyzer or by using a digital computer software program. The program may implement the FFT computational scheme or the Blackman-Tukey scheme of Fourier transforming correlation functions (13).

The Hanning window (or equivalent) should be employed for all spectral analysis. A suitable raw bandwidth will probably be between 0.01 and 0.03 Hz. The value selected will be a compromise between seeking fine frequency resolution on one hand and, on the other hand, small statistical uncertainty using a reasonably short data duration. The smaller the bandwidth, the larger is the duration of the data required. Tentatively, the bandwidth-time product (same as number of independent averages) should be at least 25 for bandwidths between 0.02 and 0.03 Hz. Smaller bandwidths may require additional averaging. Table 5-2 contains some combinations of bandwidth and number of averages, and the lengths of data record which result. It is expected that onboard spectral analysis, for the most part, would be conducted with $0.02 \leq B \leq 0.03$ Hz so that the record lengths are reasonably short (roughly 15 to 20 min). Overlap processing (non-independent averaging) is recommended and may permit a modest reduction in the length of data processed.

Table 5-2. Examples of Record Lengths Required for
Given Bandwidth and Number of Averages

BANDWIDTH, B (Hz)	NUMBER OF AVERAGES, BT	RECORD LENGTH, T (min)
0.03	25	13.9
0.02	25	20.8
0.01	25	41.7
0.01	50	83.3

The goal should be to determine the resonant frequencies to within one-half percent or better. Interpolation to locate the spectral peaks will be necessary to achieve the desired accuracy. The HP 5420A analyzer (see Table 5-1) can provide estimates of a natural frequency which is valid as long as the local frequency region is dominated by a single mode.

5.3 REQUIREMENTS FOR FIELD TESTING

5.3.1 Program for Field Evaluation

A preliminary step to field evaluation should be to investigate the characteristics and capabilities of various equipments to decide upon the specifics of the prototype system (that is, the types of equipment identified in Table 5-1).

One matter would be to determine the best technique for mass storage of raw data. Recorder noise of contending analog tape recorders operated at various record speeds should be measured to determine if acceptably low noise operation can be achieved. If the noise is not sufficiently low, the dual approaches of pre-whitening (using adjustable analog filters) followed by analog recording versus digital recording should be examined to decide upon the best approach for field use.

A logical first step for field testing a prototype system would involve a return to Shell platform SP-62C. Comparison of results with those of the past measurement program should permit the following questions to be answered:

1. Can onboard spectral analysis significantly improve the quality of the spectra and transfer functions, and thus, the accuracy of the modal parameters extracted?
2. Have the signal/noise problems with mass data storage been resolved in a way that is operationally practical?
3. Is it helpful to have better regulated power for operation of the recorder and FFT analyzer? If smoother power is helpful, should battery supply be employed or can adequate regulation of platform power be practically implemented?
4. Can the warping mode predicted by the mathematical model of SP-62C be detected and its mode shape at the 14 ft (4.3 m) level be measured to provide a more sensitive basis for failure detection (Section 4.7)?

Following the reassessment of SP-62C, it would be well to firm up a program plan for field tests on a number of platforms. The plan should address the testing of different types of structures (size, redundancy, design type) and different operating states (drilling, production). Corresponding mathematical modeling and analysis should be performed to address capability for failure detection.

5.3.2 Generalized Procedures for Installation, Calibration and Measurement Operations

On the basis of the SP-62C experience, certain procedures are now identified for future field measurement operations. In effect the following is a first iteration of a test plan. It is assumed that onboard analyses are performed using a dual-channel FFT analyzer and that all results are recorded on digital tape. All transfer function measurements are assumed to include coherence measurement. It is also assumed that analog tape recording is employed for mass data storage and that any necessary prewhitening filters are employed. The following steps are recommended.

A. Relative Calibration and System Noise

1. Arrange all accelerometers to measure the same motion.
A special fixture for installation to a main leg would be desirable for this purpose. Measure autospectra of each channel of acceleration at the signal conditioner outputs. Assess for adequate matching of spectra.
2. Disconnect accelerometers and place equivalent impedance at cable inputs. Repeat step 1 and compare to prior spectra to see if acceptable signal/noise ratio (S/N) exists.
3. Repeat step 1 and 2 by analyzing signals played back from analog tape recorder to insure the quality of taped signal is acceptable.
4. Reconnect accelerometers and measure transfer functions (using one accelerometer as a reference) to obtain quantitative calibration data.

B. Platform Equipment Noise

1. Locate two accelerometers in mutually perpendicular lateral directions adjacent to each major equipment noise source.

2. Measure autospectra to identify any periodic noise within the frequency range of platform modes to be identified.
- C. Data Acquisition and Analysis
1. Deploy accelerometers to measure lateral translation and rotation of the decks and several accelerations as close to sea level as practical and measure autospectra. A recommended arrangement of six accelerometers is shown in Figure 5-2a assuming that the conventional monitoring approach is being employed.
 2. Disconnect accelerometers from cables, provide proper input impedance to cables, measure autospectra and check to see that S/N is acceptable in deployed configuration.
 3. Reconnect accelerometers, measure transfer functions, and compare with results from any previous measurements on that platform to determine if significant changes have occurred. If the possibility exists that significant change has occurred, consider the desirability of reconfirming key results. Other deployments of accelerometers can be made to obtain additional data for investigating possible failure (e.g., Figure 5-2b).
- D. Special Test for SP-62C Retest
- Conduct the items in Step C except deploy the six accelerometers as shown in Figure 5-2c in an attempt to detect the warping mode.
- E. Post Test Relative Calibration
- Repeat determination of relative calibration data in Step A to insure that no change has occurred to the data acquisition system during the test.

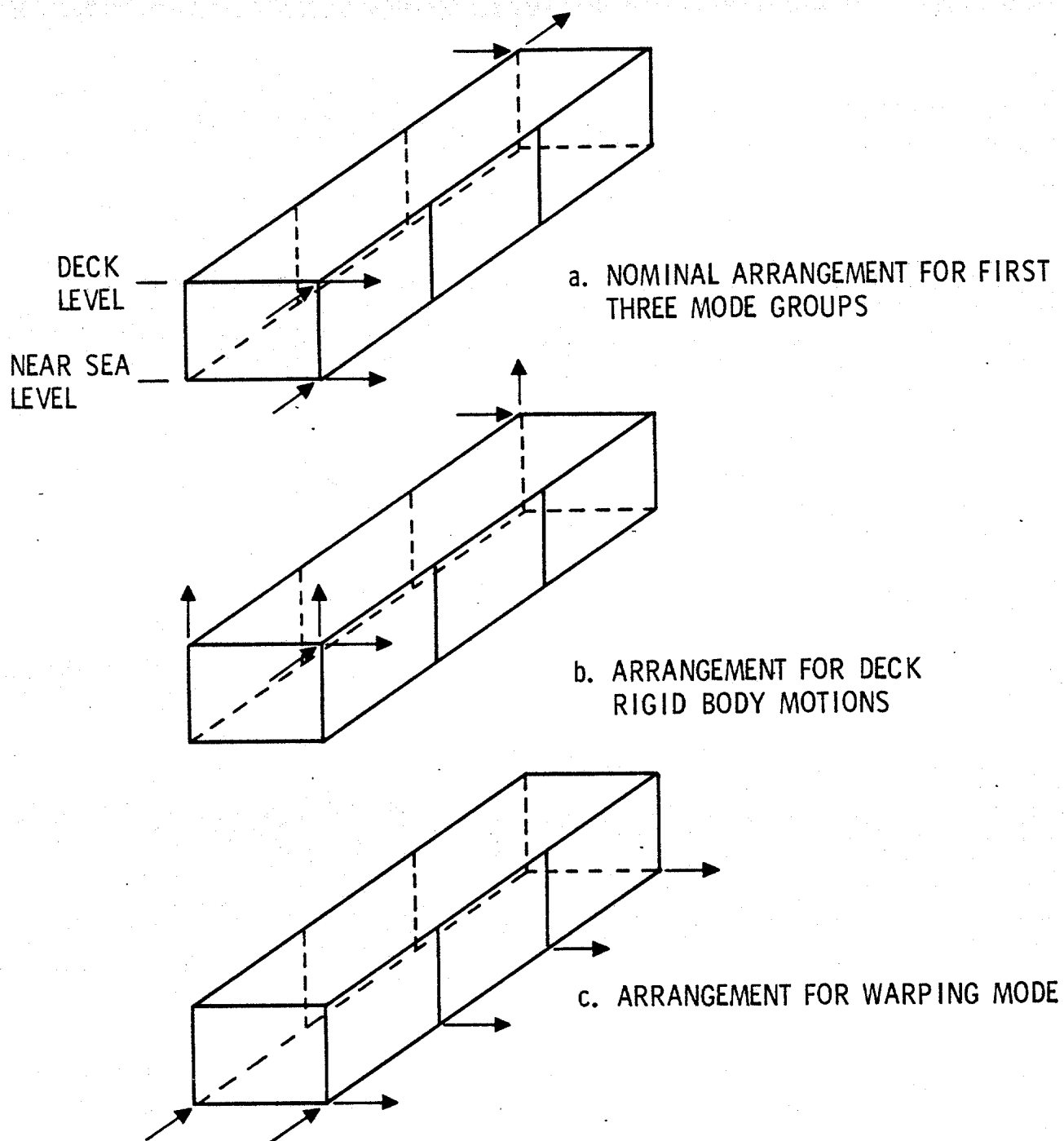


Figure 5-2. Arrangements of Accelerometers

6. CONCLUSIONS

6. CONCLUSIONS

In essence, the feasibility of vibration monitoring as a Non-Destructive Evaluation (NDE) technique has been evaluated analytically under a limited number of conditions (e.g., essentially a single class of platforms and minimal consideration of nonfailure induced modal changes). Within these constraints, the concept exhibits the capability to discern a number of significant structural failures. Nonetheless, the ability of the approach to do so in a realistic operational environment--for a variety of platforms--requires considerable, expanded examination of many other factors before questions on overall feasibility could be specifically answered. Analytically, the technique still shows promise, and the evaluations performed have identified further work which could improve that promise.

For the case of the SP-62C platform, the study indicates potential feasibility in that all aspects of the method were proven to be practical using available hardware and software (i.e., for instrumentation, data analysis, and mathematical modeling). For this class of platform, the remaining issue is the sensitivity of the concept as limited by the ability to discriminate or correct for nonfailure effects.

Detailed conclusions related to various study areas are presented below:

- Frequencies and shapes of the fundamental group of modes (broadside, end-on, torsion) are clearly identifiable from ambient data (in both calm and rough seas) with excellent accuracy. Frequencies for these in rough seas are 1 to 2% lower than those measured in calm seas. All fundamental frequencies showed excellent agreement (within 1%) with forced vibration results by Shell Oil Co.
- Certain modes above the fundamental modes can be clearly identified, namely second torsion, third end-on, and a group of four modes involving significant vertical motion. Frequencies of a number of other higher modes can be detected; however, mode shapes could not be determined. Higher modes were not affected by sea state. Detection of higher modes was limited to frequency regimes free of discrete machinery noise.

- State-of-art force balance accelerometers completely met all necessary requirements for evaluation of ambient vibration monitoring. Horizontal and vertically oriented accelerometers provided all information necessary for analysis, while angular accelerometers contributed little and are not needed.
- Both digital and analog recording methods of data acquisition are acceptable, however, care must be exercised for the latter to preclude masking of modal information by discrete recorder noise.
- A satisfactory mathematical model can be constructed by adjusting selected model parameters (particularly soil/pile, soil/jacket and pile/jacket interactions) to obtain a reasonable frequency match with experimentally detected modes.
- The efficient analysis method (employed by Aerospace) provides large reduction in cost for computing the modes of a locally altered structure. A valuable plus from the method is the expression of altered modes in terms of original modes.
- The analytical evaluation of failure detection for SP-62C, based upon frequency thresholds of 1% for fundamental modes and 2% for higher modes (values derived with minimal consideration of nonfailure uncertainties), yielded the following relative detectability for single member failures.

Detectable

- / major diagonals on extreme end-on faces
- / skirt/pile support diagonals on both extreme and end-on faces
- / main piles
- / diagonals in lower bays of broadside faces
- / corner main legs

Marginally Detectable

- / diagonals in upper bays of broadside faces
- / horizontals in extreme end-on faces

Not Detectable

- / skirt/pile support diagonals in interior end-on planes
- / diagonals (x-brace configured) in interior end-on planes
- / non-corner main legs
- / horizontals not in extreme end-on faces

- The accurate detection of shape parameters of the cross-section warping mode on the SP-62C class of platform would enable the detection of failure in all types of members.
- A degree of localization of failures is possible, but more work is needed to quantify the capability.
- Frequency sensitivity of fundamental modes for failure of vertical diagonal members can be well correlated with redundancy and flexibility parameters for a wide range of platform configurations (see Figure 4-7). Associated member load sensitivity under elastic conditions tends to be proportional to the product of the frequency sensitivity and the number of effective bays (see Figure 4-8).
- A 1% change in a fundamental frequency for an SP-62C type platform due to failure of vertical diagonal members is associated with a tolerable degradation of platform strength for Gulf of Mexico structures when manned and/or operating, since members would still see no more than 54% of design load. Even for the extreme of 20 effective bays (e.g., a Cognac type platform) there is hope for useful monitoring since member loads do not exceed 88% of design load.
- A prototype vibration monitoring system was identified which can be utilized for additional field evaluations aimed toward a possible operational definition for end-use application. This system could be employed in a portable, semi-portable or fixed configuration (as previously defined in the earlier Aerospace Report No. ATR-77(7627-02)-01).

Not Detectable

- / skirt/pile support diagonals in interior end-on planes
- / diagonals (x-brace configured) in interior end-on planes
- / non-corner main legs
- / horizontals not in extreme end-on faces

- The accurate detection of shape parameters of the cross-section warping mode on the SP-62C class of platform would enable the detection of failure in all types of members.
- A degree of localization of failures is possible, but more work is needed to quantify the capability.
- Frequency sensitivity of fundamental modes for failure of vertical diagonal members can be well correlated with redundancy and flexibility parameters for a wide range of platform configurations (see Figure 4-7). Associated member load sensitivity under elastic conditions tends to be proportional to the product of the frequency sensitivity and the number of effective bays (see Figure 4-8).
- A 1% change in a fundamental frequency for an SP-62C type platform due to failure of vertical diagonal members is associated with a tolerable degradation of platform strength for Gulf of Mexico structures when manned and/or operating, since members would still see no more than 54% of design load. Even for the extreme of 20 effective bays (e.g., a Cognac type platform) there is hope for useful monitoring since member loads do not exceed 88% of design load.
- A prototype vibration monitoring system was identified which can be utilized for additional field evaluations aimed toward a possible operational definition for end-use application. This system could be employed in a portable, semi-portable or fixed configuration (as previously defined in the earlier Aerospace Report No. ATR-77(7627-02)-01).

7. RECOMMENDATION

7. RECOMMENDATIONS

The principal areas recommended for additional effort relative to the vibration monitoring concept fall into two categories, namely (1) further analysis and test of the SP-62C platform and the currently conceived instrumentation system and (2) work that should be executed in respect to other platform types and structures to test general feasibility of the technique. Specifically, these are:

- Using the detailed mathematical model for SP-62C, study both nonfailure and multiple failure causes of modal change, including their consequences relative to the ability to locate the failure regions.
- Conduct another field test on SP-62C to (a) determine if warping mode can be detected, (b) assess deck structure interactions with global platform modes (e.g., effects of fluids in tanks), and (c) further develop the overall approach for optimizing the instrumentation system for possible operational applications. For example, establish requirements for various levels of monitoring. In particular, consider a simple resident "first level" monitoring system (2 accelerometers) to provide a historical record of the frequencies of the three fundamental modes. This would provide a "moving baseline" for long term nonfailure changes (e.g., marine growth, foundation changes), as well as a basis for correcting for short term nonfailure changes (e.g., sea state, deck loading).
- Conduct tests, to establish baseline measurements and then assess credibility of vibration monitoring technique to determine effects of controlled platform changes--on a variety of platform classes. Subscale (laboratory type) tests would be a useful first step. Nonetheless, full scale baseline measurements, at least, on various platform types would be essential in determining the broad capability for modal extraction from these structures.
- Upon determination of feasibility of the concept (to a broad range of structures) develop the goals, objectives, procedures, hardware and software configurations, etc. for possible operational applications.

REFERENCES

REFERENCES

1. Abramson, H.N., ed., "The Dynamic Behavior of Liquids in Moving Containers," NASA SP-106, 1966, Chap. 6.
2. The Aerospace Corporation, "Instrumentation of Fixed OCS Platforms," Report No. ATR-77(7627-02)-01, El Segundo, California, Oct. 1977.
3. Archer, J.S., "Consistent Matrix Formulation for Structural Analysis Using Finite-Element Techniques," Journal of American Institute of Aeronautics and Astronautics, Vol. 3, 1965, pp. 1910-1918.
4. Bathe, K.J. and Wilson, E.L., "Solution Methods for Eigenvalue Problems in Structural Mechanics," International Journal of Numerical Methods in Engineering, Vol. 6, 1973, pp. 213-226.
5. Begg, R.D., et al., "Structural Integrity Monitoring Using Digital Processing of Vibration Signals," Proceedings of the Offshore Technology Conference, Vol. 2, May 1976, pp. 305-311 (Paper OTC 2549).
6. Begg, R.D., and Mackenzie, A.C., "Monitoring of Offshore Structures Using Vibration Analysis," Proceedings of IES Symposium--Integrity of Offshore Structures, Glasgow, Scotland, April 1978.
7. Bendat, J.S., and Piersol, A.G., Random Data: Analysis and Measurement Procedures, John Wiley and Sons, Inc., New York, 1971.
8. Coppolino, R.N., "Employment of Residual Mode Effects in Vehicle/Payload Dynamic Load Analysis," Government/Industry Workshop on Payload Loads Technology, NASA CP-2075, November 1978, pp. 323-346.
9. Guyan, R.J., "Reduction of Stiffness and Mass Matrices," Journal of American Institute of Aeronautics and Astronautics, Vol. 3, No. 2, July 1971, pp. 1255-1261.
10. Isaacson, E., and Keller, H.E., Analysis of Numerical Methods, John Wiley and Sons, New York (1966), pp. 54-55.
11. Loland, O., and Dodds, C.J., "Experiences in Developing and Operating Integrity Monitoring Systems in the North Sea," Proceedings of Offshore Technology Conference, Vol. 2, May 1976, pp. 313-319 (Paper OTC 2551).
12. Marshall, P.W., "Strategy for Monitoring, Inspection and Repair for Fixed Offshore Platforms," ASME Publication Structural Integrity Technology, May 1979, pp. 97-109.

REFERENCES (CONT'D)

13. Otnes, R.K., and Enochson, L., Digital Time Series Analysis, John Wiley and Sons, New York (1972), pp. 254-278.
14. Rubin, S., "Improved Component-Mode Representation for Structural Dynamic Analysis," Journal of American Institute of Aeronautics and Astronautics, Vol. 13, No. 8, August 1975, pp. 995-1006.
15. Rubin, S., "Mode Extraction from Ambient Vibrations of an Offshore Platform," presented at the April 2-6, 1979 ASCE Spring Convention and Exhibit.
16. Ruhl, J.A., "Offshore Platforms: Observed Behavior and Comparisons with Theory," Proceedings of Offshore Technology Conference, Vol. 2, May 1976, pp. 333-352 (OTC Paper 2553).
17. Ruhl, J.A., and Berdahl, R.M., "Forced Vibration Tests of a Deepwater Platform," presented at the April 30-May 3, 1979, Offshore Technology Conference, held at Houston, Texas (Preprint OTC 3514).
18. Stevenson, A.E., and Rubin, S., "Ambient Vibration Monitoring for Assessing the Structural Health of Offshore Production Platforms," presented at the November 5-9, 1978 ASME Energy Technology Conference and Exhibition, Houston, Texas (Preprint 78-Pet-71).
19. Vandiver, J.K., "Detection of Structural Failure on Fixed Platforms by Measurement of Dynamic Response," Proceedings of Offshore Technology Conference, Vol. 2, May 1975, pp. 243-252 (OTC Paper 2267).
20. Wojnarowski, M.E., Stiansen, S.G., and Reddy, N.E., "Structural Integrity Evaluation of a Fixed Platform Using Vibration Criteria," Proceedings of Offshore Technology Conference, Vol. 3, May 1977, pp. 247-256 (OTC Paper 2909).

NOMENCLATURE

NOMENCLATURE

B	bandwidth
C	flexibility; flexibility matrix
f	frequency (Hz)
F	force
g	acceleration of gravity
i,j,k	indices
I	unit matrix
K	stiffness matrix
l, l'	length; length of projection of X_g, Z_g , plane (Fig. 3-5)
L	load; lower triangular matrix form
m_f	mass of fluid within flooded member
m_∞	virtual mass of surrounding fluid
M	mass; mass matrix
n	number of effective vertical diagonal members, Eq. (4-22)
N	number of truncated plus residual modes
P, P_e	number of bays, number of equivalent bays
q	generalized displacement vector
R	radius of gyration
R_i, R_o	inner, outer radius
T	analysis time
U_e	strain energy of removed member, Eq. (4-10)
X	displacement vector
X,Y,Z	cartesian coordinates
γ	increased flexibility factor, Eq. (4-24)
Γ	matrix of unit load vectors
δ	bay displacement vector
Δ	prefix denoting change
ϵ	changes in mode shape elements, Eq. (4-15)
θ	rotation

θ_1, θ_2	angles defined in Fig. 3-5
Λ	diagonal matrix of squared natural frequencies
ρ_w	density of water
σ	standard deviation
ϕ	mode shape vector; modal transformation
ψ_ρ	submatrix of modal transformation ϕ_d , Eq. (4-14)
ω_n	natural frequency (rad/s)

Subscripts

b	broadside direction
d	damaged structure
e	element; end on direction
f	fluid
g	global
l	lateral direction
q	generalized coordinate
s	static
t	set of truncated modes
θ	torsion
ρ	set of residual modes

Abbreviations

dB	decibel
dof	degree of freedom
Hz	hertz (cycle per second)
ips	inches per second
kip	1000 pounds dead weight load

APPENDIX A

AMBIENT VIBRATION DATA

Table A-1. Data Acquisition Runs

RUN NO.	RUN TYPE	START TIME	DURATION	SEA CONDITION	MEASUREMENTS ¹								TAPE ² NO.	LOW-PASS CUTOFF (Hz)	IRIG TIME ³ (IRIG B SLO CODE)	COMMENTS
					TK 1	TK 2	TK 3	TK 4	TK 5	TK 6	TK 7	TK 8				
1	Overall Cal	9:55AM (10/12/77)	28 min	Rough	$\bar{X}(A1-49)$								1	2	1716.50 -1720.20 (Day 295)	TK 1 Filtered at 20 Hz
2	Polarity Check	10:30AM	1 min										1	-	1720.50-1720.57	T in Accels in Succession TRS 1 to 7
3-8	Recorder Cal	10:52AM	16 min										1	-	1721.00-5-1723.00	0.5, 1.2, 7.5, 15, 20, 35 Hz at 2.5 v 0-P
9-13	SC-1 Cal	12:47AM	12 min										1	-	1723.00-1724.45	0.5, 1.2, 7.5, 20, 15 Hz at 3.1 mv rms
14	Data Run	7:00PM	5.1 hr	Rough	$\bar{X}(A1-14)$	$\bar{Y}(A1-14)$	$\bar{Z}(A1-14)$	$\bar{X}(B3-14)$	$\bar{Y}(B4-14)$	$\bar{Z}(B4-14)$	$\bar{X}(B4-14)$	$\bar{Y}(A1-14)$	1	20	1726.40-1804.40	
15	Data Run	11:10AM (10/13/77)	2.2 hr	Rough	"	"	"	"	"	"	"	"	2	5	1758.40-1815.15 (Day 296)	Repeat of Run 14 with Low-Pass Filter Change
16	Overall Cal	3:17PM	19 min	Rough	$\bar{X}(A1-49)$								2	5	1815.30-1817.50	
17	Data Run	5:45PM	6.4 hr	Rough	$\bar{X}(A1-14)$	$\bar{Y}(A1-14)$	$\bar{Z}(A1-14)$	$\bar{X}(A1-49)$	$\bar{Y}(A1-14)$	$\bar{Z}(A1-14)$	$\bar{X}(B4-49)$	$\bar{Y}(B3-14)$	3	5	1825.00-1913.00	Pumps Off Until About 7:45PM
18	Data Run	8:24AM (10/14/77)	2.9 hr	Calm	$\bar{X}(A1-14)$	$\bar{Y}(A1-14)$	$\bar{Z}(A1-14)$	$\bar{X}(A1-49)$	$\bar{Y}(A1-49)$	$\bar{Z}(A1-49)$	$\bar{X}(B4-49)$	Rover	4	20	1921.40-1944.30	Rover Moved to Equipments
19	Overall Cal	12:34PM	21 min	Calm	$\bar{X}(A1-49)$								4	20	1945.30-1948.10	
20	High-Pass Filter Cal	2:00PM	12 min										5	5	1952.30-1954.02	0.5, 0.7, 0.9, 1.1, 1.3, 1.5, 2.0, 2.5, 3, 4, 5 Hz at 18 mv 0-P, High-Pass Cutoff at 1 Hz
21	Data Run	2:46PM	2.0 hr	Calm	$\bar{X}(A1-14)$	$\bar{Y}(A1-14)$	$\bar{Z}(A1-14)$	$\bar{Y}(B4-49)$	$\bar{X}(B4-49)$	$\bar{Z}(A1-49)$	$\bar{X}(B4-49)$	$\bar{Y}(A1-49)$	5	5	1954.20-2009.10	High-Pass Filters in
22	Data Run	5:24PM	6.6 hr	Calm	"	"	"	"	"	"	"	"	6	20	2016.50-2100.40	Same as Run 21 Without High-Pass Filters
23	SC-1 Cal	5:00PM	2 min										6	5	2016.12-2016.28	0.5, 1, 2, 3, 4, 5, 10, 20, 35, 50, 100 Hz

¹ TK 2 contains FM carrier signal for reference.

² 1/2 in., 8-channel recorded at 15/16 ips.

³ Time code added to 1 in. dub tape at 8 times record speed.

Table A-2 Data Analysis Runs

ANALYSIS RUN NO.	DATA RUN NO.	SAMPLING RATE (SPS)	IRIG INTERVAL	RAW BAND- WIDTH, B	BT	WINDOW	DESCRIPTION
1	18	100	1921.35-1928.30 1932.30-1934.30	0.1		Hamming	Digitize Using 40-Hz Low-Pass Analog Filter (Constant Amplitude); Decimate to 100 SPS Using 50-Hz Low-Pass Digital Filters; PSD TKs 1, 3, 5, 8. Evaluate Equipment Signatures and Antialiasing Requirements
2	all	60	all			-	Digitize Using 25-Hz Low-Pass Analog Filter (Constant Amplitude). All Data Digitized.
3	18	60	1925.10-1925.18	0.06	8.64	Several	XPSDs Ref. TK 3 for TKs 1 and 5 Using No Window, Hanning, Hanning Twice. Window Evaluation.
4	14	15	1728.30-1729.53.3 1729.53.3-1731.16.6	0.015 0.015	10 10	Hanning	Decimate Tape 1 to 15 SPS. XPSDs Ref. TK 8 (Both Times)
5	14	5	1728.30-1732.40 1732.40-1736.50	0.005 "	10 10	"	Decimate Tape 1 to 5 SPS. XPSDs Ref. TK 8 (Both Times)
6	14	15	1730.00-1732.47	0.045	60	"	XPSDs Ref. TK 8
7	14	15	1741.40-1743.30	0.03	26.4	"	XPSDs Ref. TK 3
8	15	15	1758.40-1802.40	0.03	57.6	"	XPSDs Ref. TK 1
9	16	15	1815.30-1817.30	0.03	28.8	"	XPSDs Ref. TK 1
10	17	15	1825.00-1827.00	0.03	28.8	"	XPSDs Ref. TK 3
11	18	15	1929.20-1931.20	0.03	28.8	"	XPSDs Ref. TK 5 (TK 8 deleted)
12	21	15	1956.30-1958.30	0.03	28.8	"	XPSDs Ref. TK 5

Table A-2. Data Analysis Runs (Cont'd)

ANALYSIS RUN NO.	DATA RUN NO.	SAMPLING RATE (SPS)	IRIG INTERVAL	RAW BAND- WIDTH, B	BT	WINDOW	DESCRIPTION
13	22	15	2018.30-2020.30	0.03	28.8	Hanning	XPSDs Ref. TK 5
14	18	15	1929.20-1931.20	0.03	28.8	"	XPSDs Ref. TK 1
15	21	15	1956.30-1958.30	0.03	28.8	"	XPSDs Ref. TK 3
16	17	15	1825.00-1827.00	0.03	28.8	"	XPSDs Ref. TK 7
17	18	15	1929.20-1931.20	0.03	28.8	"	XPSDs Ref. TK 7 (TK 8 deleted)
18	17	15	1909.50-1911.50	0.03	28.8	"	XPSDs Ref. TK 6
19	19	15	1945.40-1947.40	0.03	28.8	"	XPSDs Ref. TK 1
20	18	15	1942.10-1944.10	0.03	28.8	"	XPSDs Ref. TK 4
21	18	15	1921.40-1922.40	0.03	14.4	"	XPSDs Ref. TK 7
22	1	15	1716.50-1720.20	0.03	50.4	"	XPSD TK 1 vs. TK 4
23	18	60	1942.10-1944.10	0.06	57.6	"	XPSD TK 8 vs. TK 4
24	18	15	1925.43-1926.03	0.03	4.8	"	XPSDs Ref. TK 4 (TK 8 deleted) (Air Compressor Off)
25	18	15	1926.02-1926.22	0.03	4.8	"	XPSDs Ref. TK 4 (TK 8 deleted) (Air Compressor On)
26	18	15	1934.05-1934.25	0.03	4.8	"	XPSDs Ref. TK 4 (TK 8 deleted) (During Generator Monitoring)
27	17	15	1907.50-1911.50	0.015	14.4	"	XPSDs Ref. TK 4: TKs 6 and 7
28	18	15	1940.40-1944.40	0.015	14.4	"	XPSDs Ref. TK 4: TKs 6 and 7
29	17	15	1859.50-1911.50	0.03	172.8	"	XPSD TK 1 vs. TK 6

Table A-3. Mode Shape Parameters

FREQUENCY (Hz)	FUNCTION ¹	AMPLITUDE ²	PHASE ² (deg.)	COHERENCE	DATA RUN	ANALYSIS RUN
0.65	X (B3-14)/X (A1-14)	0.95	14	0.98	15	8
	X (B4-14)/X (A1-14)	0.96	14	0.98	15	8
	X (A1-49)/X (A1-14)	1.30	0	0.99	17	10
	X (B4-49)/X (A1-14)	1.20	0	0.93	17	10
	X (A1-49)/Z (A4-49)	-17.00	0	0.43	21	15
	Z (A1-49)/X (A1-14)	0.04	-160	0.74	15	8
	Z (B3-14)/X (A1-14)		5	0.96	17	10
	Z (B4-49)/Z (A4-49)	2.40	176	0.89	21	15
	θ_y (A1-14)/X (A1-14)			0.98	15	8
0.66	Y (A1-14)/Y (B4-49)	0.80	5	0.98	22	13
	" "	0.77	0	0.98	21	12
	Y (B4-14)/Y (A1-14)	0.96	1	0.99	14	7
	Y (A1-49)/Y (A1-14)	1.16	0	0.98	18	14
	Z (A1-49)/Y (B4-49)	0.024	-5	0.75	22	13
	Z (B4-49)/Y (B4-49)	0.077	172	0.83	22	13
	Z (A1-49)/Y (A1-14)	0.039	-5	0.48	14	7
	Y (A1-14)/Z (A1-49)	33.00	0	0.84	21	15
	Z (A1-49)/Z (A4-49)	0.76	180	0.75	21	15
	Z (B4-49)/Z (A4-49)	2.40	0	0.89	21	15
	Z (A4-49)/Y (B4-49)	0.032	177	0.92	22	13
	Y (B4-49)/Z (A4-49)	40.00	180	0.89	21	15
	θ_x (A1-49)/Z (A4-49)			0.88	21	15

¹ The data analyzed were accelerations, but the results hold equally for the displacement ratios listed.

² Blank spaces indicate "unknown" because of uncertain calibration or gain.

Table A-3. Mode Shape Parameters (Cont'd.)

FREQUENCY (Hz)	FUNCTION ¹	AMPLITUDE ²	PHASE ² (deg.)	COHERENCE	DATA RUN	ANALYSIS RUN
0.96	X (A1-14)/Y (A1-14)	1.63	0	0.97	14	7
	" "	1.68	0	0.98	18	14
	Y (A1-14)/X (A1-14)	0.64	14	0.98	15	8
	" "	0.59	0	0.97	17	10
	Y (B4-14)/Y (A1-14)	0.83	-178	0.92	14	7
	Y (B4-14)/X (A1-14)	0.53	-158	0.97	15	8
	X (B4-14)/Y (A1-14)	2.25	178	0.97	14	7
	X (B4-14)/X (A1-14)	1.47	-165	0.98	15	8
	X (B3-14)/Y (A1-14)	0.96	-169	0.97	14	7
	X (B3-14)/X (A1-14)	0.62	-164	0.97	15	8
	X (A1-14)/Y (B4-49)	1.72	-4	0.95	22	13
	" "	1.60	-5	0.95	21	12
	Y (A1-14)/Y (B4-49)	0.94	180	0.88	22	13
	" "	0.86	177	0.88	21	12
	X (A1-49)/Y (A1-14)	2.70	3	0.98	18	14
	X (A1-49)/X (A1-14)	1.52	1	0.99	17	10
	Y (A1-49)/Y (A1-14)	1.08	1	0.99	18	14
	Y (A1-49)/X (A1-14)	0.65	7	0.96	17	10
	X (B4-49)/Y (A1-14)	3.05	177	0.98	18	14
	X (B4-49)/X (A1-14)	1.79	-178	0.97	17	10
	Z (A1-49)/Y (A1-14)	0.056	-176	0.93	14	7
	Z (A1-49)/X (A1-14)	0.035	-163	0.96	15	8
	Z (B3-14)/X (A1-14)		-173	0.94	17	10
	Z (A1-49)/Y (B4-49)	0.048	6	0.88	21	12
	" "	0.054	-1	0.87	22	13
	Z (A4-49)/Y (B4-49)	0.047	-4	0.75	21	12
	" "	0.057	-1	0.89	22	13

Table A-3. Mode Shape Parameters (Cont'd.)

FREQUENCY (Hz)	FUNCTION ¹	AMPLITUDE ²	PHASE ² (deg.)	COHERENCE	DATA RUN	ANALYSIS RUN
0.96	Z (B4-49)/Y (B4-49)	0.052	-2	0.70	21	12
	" "	0.055	0	0.79	22	13
	X (A1-49)/Z (A4-49)	26.00	0	0.73	21	15
	Y (A1-14)/Z (A4-49)	14.70	180	0.75	21	15
	Y (B4-49)/Z (A4-49)	15.40	6	0.73	21	15
	Z (A1-49)/Z (A4-49)	0.85	7	0.77	21	15
	Z (B4-49)/Z (A4-49)	0.94	10	0.66	21	15
	Y (A1-14)/ θ_z (A1-49)		10	0.98	18	11
	X (A1-14)/ θ_z (A1-49)			0.99	18	11
	X (A1-49)/ θ_z (A1-49)			0.99	18	11
	Y (A1-49)/ θ_z (A1-49)			0.97	18	11
	X (B4-49)/ θ_z (A1-49)			0.99	18	11
	θ_y (A1-14)/Y (A1-14)			0.95	14	7
	θ_y (A1-14)/X (A1-14)			0.98	15	8
1.28	Y (A1-49)/Y (A1-14)	2.75	-2	0.84	18	14
	" "	3.57	8	0.80	17	29
	Y (A1-14)/Y (B4-49)	0.20	25	0.43	21	12
	" "	0.19	1	0.48	22	13
	Y (A1-14)/X (B4-49)	0.20	-179	0.45	17	16
	Y (A1-49)/X (A1-14)	0.65	178	0.46	17	10
	Z (B4-49)/Y (B4-49)	0.052	165	0.33	22	13
	Z (B3-14)/X (B4-49)	0.13	20	0.36	17	16
	θ_x (A1-14)/Y (A1-49)			0.76	17	18
	θ_z (A1-49)/X (B4-49)			0.62	18	17

Table A-3. Mode Shape Parameters (Cont'd.)

FREQUENCY (Hz)	FUNCTION ¹	AMPLITUDE ²	PHASE ² (deg.)	COHERENCE	DATA RUN	ANALYSIS RUN
1.47	Y (A1-14)/X (A1-14)	1.02	22	0.50	15	8
	X (B3-14)/Y (A1-14)	0.59	-176	0.57	14	7
	X (B4-14)/Y (A1-14)	0.89	176	0.41	14	7
	Y (A1-14)/X (B4-49)	0.15	172	0.39	18	17
	Y (A1-14)/Y (B4-49)	0.17	10	0.34	22	13
	Y (A1-49)/Y (A1-14)	2.20	0	0.53	18	14
	X (B4-49)/Y (A1-14)	2.60	-170	0.39	18	14
	Y (A1-14)/Y (A1-49)	0.26	5	0.68	17	18
	Z (A1-49)/Z (A4-49)	0.49	-9	0.35	21	15
	Z (B3-14)/X (B4-49)	0.15	25	0.35	17	16
	Y (A1-14)/ θ_z (A1-49)			0.37	18	11
1.54	Y (A1-14)/X (A1-14)	0.95	30	0.43	15	8
	X (B3-14)/X (A1-14)	0.71	-167	0.33	15	8
	X (B3-14)/Y (A1-14)	0.58	-171	0.43	14	7
	X (B4-14)/Y (A1-14)	1.20	178	0.37	14	7
	Y (A1-14)/X (B4-49)	0.11	157	0.51	18	17
	Y (A1-49)/Y (A1-14)	2.10	2	0.50	18	14
	X (B4-49)/Y (A1-14)	4.70	-160	0.51	18	14
	Y (A1-14)/Y (A1-49)	0.20	-15	0.72	17	18
	X (A1-49)/X (B4-49)	0.54	96	0.38	18	17
	Y (A1-49)/X (B4-49)	0.27	155	0.37	18	17
	Z (A1-49)/Y (B4-49)	0.09	19	0.37	21	12
	Z (B4-49)/Y (B4-49)	0.13	175	0.34	21	12
	Z (B3-14)/X (B4-49)	0.10	-12	0.36	17	16
	Y (A1-14)/ θ_z (A1-49)			0.48	18	11
	X (A1-49)/ θ_z (A1-49)			0.58	18	11
	Y (A1-49)/ θ_z (A1-49)			0.44	18	11
	X (B4-49)/ θ_z (A1-49)			0.58	18	11

Table A-3. Mode Shape Parameters (Cont'd.)

FREQUENCY (Hz)	FUNCTION ¹	AMPLITUDE ²	PHASE ² (deg.)	COHERENCE	DATA RUN	ANALYSIS RUN
1.71	X (A1-49)/Y (A1-49)	1.16	-13	0.83	17	18
	X (B4-49)/Y (A1-49)	2.20	165	0.88	17	18
	Y (A1-49)/X (B4-49)	0.37	-170	0.85	18	17
	X (A1-49)/X (B4-49)	0.56	-178	0.83	18	17
	X (A1-14)/X (B4-49)	0.09	10	0.46	18	17
	X (A1-49)/ θ_z (A1-49)			0.83	18	11
	Y (A1-49)/ θ_z (A1-49)			0.80	18	11
	X (B4-49)/ θ_z (A1-49)			0.92	18	11
	X (A1-14)/ θ_z (A1-49)			0.43	18	11
	θ_x (A1-14)/Y (A1-49)			0.48	17	18
	θ_y (A1-49)/X (A1-14)			0.40	15	8
2.04	Y (A1-49)/X (A1-14)	0.49	-25	0.38	17	10
	X (A1-49)/X (A1-14)	1.03	50	0.70	17	10
	X (A1-14)/Y (B4-49)	0.40	5	0.35	21	12
	Y (B4-14)/Y (A1-14)	1.10	2	0.87	14	7
	Y (A1-14)/X (A1-14)	0.83	-150	0.38	15	8
	" "	0.65	-170	0.48	17	10
	Y (B4-14)/X (A1-14)	1.55	40	0.53	15	8
	Z (A1-49)/Y (A1-14)	0.29	20	0.81	14	7
	Z (A1-49)/X (A1-14)	0.33	-140	0.65	15	8
	Z (A4-49)/Y (B4-49)	0.27	-5	0.64	22	13
	Z (B4-49)/Y (B4-49)	0.28	28	0.60	22	13
	" "	0.33	5	0.50	21	12
	θ_z (A1-49)/X (B4-49)			0.48	18	17
	θ_x (A1-14)/Y (A1-49)			0.79	17	18

Table A-3. Mode Shape Parameters (Cont'd.)

FREQUENCY (Hz)	FUNCTION ¹	AMPLITUDE ²	PHASE ² (deg.)	COHERENCE	DATA RUN	ANALYSIS RUN
2.12	Y (A1-49)/X (B4-49)	0.60	3	0.30	18	17
	Y (B4-49)/X (A1-14)	1.40	-126	0.54	15	8
	X (A1-14)/Y (B4-49)	0.44	170	0.53	22	13
	X (A1-49)/X (A1-14)	1.22	80	0.55	17	10
	Y (A1-49)/X (A1-14)	1.70	0	0.60	17	10
	X (A1-14)/Y (A1-49)	0.25	-32	0.39	17	18
	X (B4-49)/X (A1-14)	1.78	-115	0.43	17	10
	Y (A1-14)/Y (A1-49)	0.74	161	0.91	17	18
	Y (A1-14)/Y (B4-49)	0.59	178	0.80	21	12
	Y (A1-14)/Y (B4-49)	0.74	-169	0.80	22	13
	Y (B4-14)/Y (A1-14)	0.90	1	0.84	14	7
	X (B4-14)/Y (A1-14)	0.63	170	0.67	14	7
	Y (A1-14)/X (A1-14)	1.33	-130	0.68	17	10
	Z (A1-49)/Y (A1-14)	0.24	13	0.76	14	7
	Z (A1-49)/X (A1-14)	0.35	-127	0.57	15	8
	Z (B3-14)/Y (A1-49)	0.36	-11	0.38	17	18
	Z (A1-49)/Y (B4-49)	0.21	-166	0.79	21	12
	" "	0.22	-170	0.63	22	13
	Z (B4-49)/Y (B4-49)	0.16	14	0.44	21	12
	" "	0.20	4	0.65	22	13
	Z (A4-49)/Y (B4-49)	0.18	0	0.60	21	12
	" "	0.24	8	0.70	22	13
	θ_x (A1-14)/X (A1-14)			0.40	17	10
	θ_x (A1-14)/Y (A1-49)			0.85	17	18

Table A-3. Mode Shape Parameters (Cont'd.)

FREQUENCY (Hz)	FUNCTION ¹	AMPLITUDE ²	PHASE ² (deg.)	COHERENCE	DATA RUN	ANALYSIS RUN
2.21	X (A1-49)/X (B4-49)	0.70	166	0.74	17	16
	Y (A1-49)/X (B4-49)	0.46	17	0.68	17	16
	X (A1-14)/X (B4-49)	0.24	0	0.44	18	17
	Y (B4-14)/Y (A1-14)	0.60	-10	0.50	14	7
	X (B4-14)/Y (A1-14)	0.66	166	0.42	14	7
	Y (A1-14)/X (A1-14)		15	0.35	15	8
	" "	0.53	-20	0.30	17	10
	Z (B3-14)/X (B4-49)	0.30		0.50	17	16
	Z (A1-49)/Y (A1-14)	0.90	0	0.51	14	7
	θ_y (A1-14)/Y (A1-14)			0.32	14	7
	θ_y (A1-14)/X (A1-14)			0.70	15	8
	θ_z (A1-49)/X (B4-49)			0.41	18	17
2.62	Y (B4-14)/Y (A1-14)	1.12	4	0.74	14	7
	X (B4-14)/Y (A1-14)	1.24	-10	0.48	14	7
3.01	Z (A4-49)/Y (B4-49)	0.87	-15	0.46	22	13
	" "	0.60	-25	0.37	21	12
	Z (B4-49)/Y (B4-49)	0.64	5	0.34	22	13
	Y (A1-14)/Z (A4-49)	0.63	18	0.33	21	15
	Y (B4-49)/Z (A4-49)	0.70	25	0.36	21	15
	Z (B4-49)/Z (A4-49)	1.10	2	0.63	21	15
3.05	Y (A1-14)/Y (B4-49)	0.89	-128	0.63	22	13

Table A-3. Mode Shape Parameters (Cont'd.)

FREQUENCY (Hz)	FUNCTION ¹	AMPLITUDE ²	PHASE ² (deg.)	COHERENCE	DATA RUN	ANALYSIS RUN
3.44	X (A1-49)/X (B4-49)	0.065	30	0.63	18	21
	Y (A1-49)/X (B4-49)	0.95	-140	0.41	18	21
	Z (B3-14)/Y (A1-49)		-100	0.80	17	29
	θ_z (A1-49)/X (B4-49)			0.49	18	21
3.50	X (A1-49)/X (B4-49)	0.08	30	0.57	18	17
	Y (A1-49)/X (B4-49)	0.27	-166	0.80	18	17
	X (B4-49)/Y (A1-49)	2.30	140	0.70	17	18
	Y (A1-14)/Y (B4-49)	0.28	152	0.74	21	12
	" "	0.37	160	0.93	22	13
	Y (A1-49)/Y (A1-14)		48	0.37	18	14
	X (B4-49)/Y (A1-14)	3.10	159	0.42	18	14
	Y (A1-14)/X (B4-49)	0.13	158	0.40	18	17
	X (B3-14)/Y (A1-14)	0.68	174	0.32	14	7
	Y (B4-14)/Y (A1-14)	0.91	17	0.68	14	7
	Z (B3-14)/X (A1-14)	2.90	40	0.49	17	10
	Z (A1-49)/X (A1-14)	1.45	60	0.35	15	8
	Z (A1-49)/Y (B4-49)	0.28	175	0.30	22	13
	Z (A4-49)/Y (B4-49)	0.85	-3	0.93	21	12
	Z (A4-49)/Y (B4-49)	1.00	-10	0.86	22	13
	Y (A1-14)/Z (A4-49)	0.33	153	0.70	21	15
	Z (B4-49)/Z (A4-49)	0.80	2	0.63	21	15
	Y (A1-49)/ θ_z (A1-49)			0.75	18	11
	X (B4-49)/ θ_z (A1-49)			0.79	18	11
	θ_z (A1-49)/Y (A1-14)			0.34	18	14
	X (A1-49)/ θ_z (A1-49)			0.42	18	11
	θ_z (A1-49)/X (B4-49)			0.79	18	17

Table A-3. Mode Shape Parameters (Cont'd.)

FREQUENCY (Hz)	FUNCTION ¹	AMPLITUDE ²	PHASE ² (deg.)	COHERENCE	DATA RUN	ANALYSIS RUN
3.30	X (A1-14)/Y (B4-49)	0.41	0	0.53	22	13
	Y (A1-14)/Y (B4-49)	0.15	-2	0.30	22	13
	X (A1-14)/Y (A1-49)	0.44	-15	0.43	17	29
	X (B3-14)/X (A1-14)	3.50	7	0.68	15	8
	Z (A4-49)/Y (B4-49)	1.83	-15	0.93	22	13
	Z (A1-49)/Y (B4-49)	1.83	0	0.85	22	13
	Z (B4-49)/Y (B4-49)	1.75	19	0.90	22	13
	X (A1-14)/Z (A4-49)	0.19	-165	0.50	21	15
	Y (B4-49)/Z (A4-49)	0.59	-10	0.82	21	15
	Z (B3-14)/Y (A1-49)	5.00	125	0.73	17	29
	Z (B3-14)/X (A1-14)		150	0.30	17	10
	Z (A1-49)/Z (A4-49)	1.20	25	0.76	21	15
	Z (B4-49)/Z (A4-49)	1.10	-11	0.93	21	15
	θ_x (A1-49)/Y (B4-49)			0.87	22	13
	θ_x (A1-49)/Z (A4-49)			0.88	21	15
3.92	X (A1-49)/X (B4-49)	0.10	35	0.75	17	16
	X (A1-49)/X (B4-49)	0.18	5	0.88	18	17
	Y (A1-49)/X (B4-49)	0.26	-143	0.92	17	16
	Y (A1-49)/X (B4-49)	0.28	-162	0.95	18	17
	X (A1-49)/Y (A1-49)	0.47	-175	0.75	17	29
	Y (A1-49)/X (A1-49)	1.93	165	0.87	18	20
	X (B4-49)/Y (A1-49)	3.50	151	0.92	17	29
	X (B4-49)/X (A1-49)	4.50	-40	0.87	18	20
	Y (A1-14)/X (B4-49)	0.16	175	0.60	17	16
	" "	0.24	0	0.69	18	17
	Y (A1-49)/Y (A1-14)	0.82	18	0.69	18	14
	X (B4-49)/Y (A1-14)	2.85	0	0.69	18	14
	X (A1-49)/Y (A1-14)	0.51	-145	0.65	18	14
	Y (A1-14)/Y (B4-49)	0.99	171	0.72	22	13

Table A-3. Mode Shape Parameters (Cont'd.)

FREQUENCY (Hz)	FUNCTION ¹	AMPLITUDE ²	PHASE ² (deg.)	COHERENCE	DATA RUN	ANALYSIS RUN
3.92	Y (A1-14)/Y (A1-49)	0.55	34	0.46	17	29
	Y (A1-14)/X (A1-49)	1.00	137	0.65	18	20
	X (B4-14)/Y (A1-14)	0.63	175	0.33	14	7
	X (A1-14)/Y (A1-14)	0.51	-25	0.51	18	14
	Z (B3-14)/X (B4-49)	1.35	-148	0.89	17	16
	Z (A4-49)/Y (B4-49)	2.40	-15	0.70	22	13
	Y (A1-14)/Z (A4-49)	0.37	-175	0.72	21	15
	Y (B4-49)/Z (A4-49)	0.36	5	0.65	21	15
	Z (B3-14)/Y (A1-49)		3	0.94	17	29
4.05	Y (A1-49)/X (B4-49)	0.16	-143	0.53	18	17
	X (A1-14)/X (B4-49)	0.19	140	0.35	18	17
	X (A1-14)/Y (B4-49)	0.73	-15	0.40	22	13
	" "	0.63	-35	0.57	21	12
	Z (A1-49)/Y (B4-49)	0.95	-173	0.58	22	13
	" "	1.18	-150	0.67	21	12
	Z (B4-49)/Y (B4-49)	1.70	165	0.45	22	13
	" "	1.48	160	0.39	21	12
	Z (B3-14)/X (A1-14)	2.00	-163	0.32	17	10
	Z (A1-49)/Z (A4-49)	0.48	10	0.33	21	15
	Z (B4-49)/Z (A4-49)	1.20	-12	0.76	21	15
	θ_x (A1-49)/Y (B4-49)			0.56	22	13
	θ_x (A1-49)/Z (A4-49)			0.40	21	15
	θ_z (A1-49)/X (B4-49)			0.55	18	17

Table A-3. Mode Shape Parameters (Cont'd.)

FREQUENCY (Hz)	FUNCTION ¹	AMPLITUDE ²	PHASE ² (deg.)	COHERENCE	DATA RUN	ANALYSIS RUN
4.4	Z (A1-49)/Y (B4-49)	1.20	-179	0.94	22	13
	θ_x (A1-49)/Y (B4-49)			0.85	22	13
4.5	Y (A1-49)/X (A1-49)	0.60	37	0.56	18	20
	Y (A1-49)/X (B4-49)	0.36	-140	0.49	18	17
	X (A1-49)/X (B4-49)	0.53	165	0.55	17	16
	Y (A1-49)/Y (A1-14)	0.79	20	0.74	18	14
	X (A1-14)/X (A1-49)	0.90	-30	0.90	18	20
	X (A1-14)/Y (B4-49)	0.52	-35	0.87	22	13
	Y (A1-14)/Y (B4-49)	0.51	120	0.38	22	13
	Y (A1-14)/X (B4-49)	0.31	-168	0.32	18	17
	X (A1-49)/X (A1-14)	1.00	39	0.92	17	10
	Y (A1-49)/X (A1-14)	0.90	-160	0.72	17	10
	X (B4-49)/X (A1-14)	1.23	-154	0.69	17	10
	Y (A1-14)/X (A1-14)	0.70	15	0.58	17	10
	Z (A4-49)/Y (B4-49)	0.60	20	0.34	22	13
	Z (A1-49)/Y (B4-49)	1.20	172	0.95	22	13
	" "	1.30	175	0.93	21	12
	Z (B4-49)/Y (B4-49)	0.50	-30	0.50	22	13
	Z (B3-14)/X (A1-14)		180	0.58	17	10
	Y (A1-14)/Z (A4-49)	0.40	30	0.38	17	10
	X (A1-14)/ θ_z (A1-49)			0.73	18	11
	X (A1-49)/ θ_z (A1-49)			0.71	18	11
	θ_x (A1-49)/Y (B4-49)			0.53	22	13
	θ_x (A1-14)/X (A1-14)			0.47	17	10

APPENDIX B

MASS DISTRIBUTION AND MODAL PLOTS

Appendix B

Mass Distribution and Modal Plots

Deck mass distributions used as inputs to the mathematic model of the platform are listed in Table B-1. A set of mode shape plots from the model are presented in Figures B-1 through B-22 for frequencies ranging from 0.639 Hz to 4.13 Hz . On each figure the mode shapes for the entire structure are shown on the left and for the upper levels of the platform on the right. The upper levels are labeled explicitly on Figure B-1. The modal deflections shown in the various upper level plots reflect the fact that the modes are normalized to unit generalized mass ($M = 1$); likewise, for the various overall mode shapes.

Table B-1. Deck Mass Distribution

Item	Total Weight (Mass) KIP (Mg)	Distributed Weight (Mass) KIP (Mg)	Nodes
Lower Deck ¹ Structure	393 (178)	49.1 (22.3)	1006,1010,1014,1018, 1040,1044,1048,1052
Upper Deck ¹ Structure	116 (53)	14.5 (6.6)	2006,2010,2014,2018, 2040,2044,2048,2052
4000-bbl Tank	244 (111)	48.8 (22.1)	2006,2020,2024,2035 2040
400-bbl Tank Fluids	929 (421)	194 (88.0)-X 263 (119)-Y 410 (186)-Z 273 (124)-X 263 (119)-Y 519 (235)-Z	2006 2040
Quarters Bldg.	50 (23)	25 (11.3)	2010,2021
Compressor Skid	800 (363)	100 (45.4)	2014,2015,2016,2017 2048,2047,2050,2051
Fan Skid	100 (45)	20 (9)	2018,2023,2034,2038, 2052
Crane	44 (20)	44 (20)	2055
Research Bldg.	5 (2)	5 (2)	2002
Pumps	60 (27)	30 (14)	1042,1055
Flotation Cell	40 (18)	20 (9)	1007,1041
Flotation Tank Fluid	116 (52.6)	28.2 (12.8)-X 28.2 (12.8)-Y 57.9 (26.3)-Z 42.3 (19.2)-X 42.3 (19.2)-Y 57.9 (26.3)-Z	1041 1007
Air Compressor	15 (7)	7.5 (3.4)	1025,1044
Fresh Water	35 (16)	35 (16)	1054
Generator Skid	176 (80)	44 (20)	1044,1048,1055,1056

¹ Mass in structural model of deck not included.

Table B-1. Deck Mass Distribution (Cont'd)

<u>Item</u>	<u>Total Weight (Mass)</u> <u>KIP (Mg)</u>	<u>Distributed Weight (Mass)</u> <u>KIP (Mg)</u>	<u>Nodes</u>
Evaporator Scrubber	7 (3)	7 (3)	1048
Free Water Knock Out	156 (71)	78 (35)	1003,1016
Gas Scrubber	40 (18)	20 (9)	1019,1034
Separator Skid	340 (154)	68 (31)	1014,1018,1033,1048 1052
Welder's Shock	5 (2)	5 (2)	1001
Work Shock	10 (5)	10 (5)	1010
Steel Rocks	15 (7)	7.5 (3)	1005,1039
Escape Module	<u>5 (2)</u>	2.5 (1)	1005,1039
Subtotal	3701 (1679)		
Structural Model			
Lower Deck	270 (122)		
Upper Deck	<u>221 (100)</u>		
Total Decks	4192 (1901)		
Breakdown:			
Structure	1000 (454)		
Equipment	1903 (863)		
Fluids	<u>1289 (585)</u>		
	4192 (1901)		

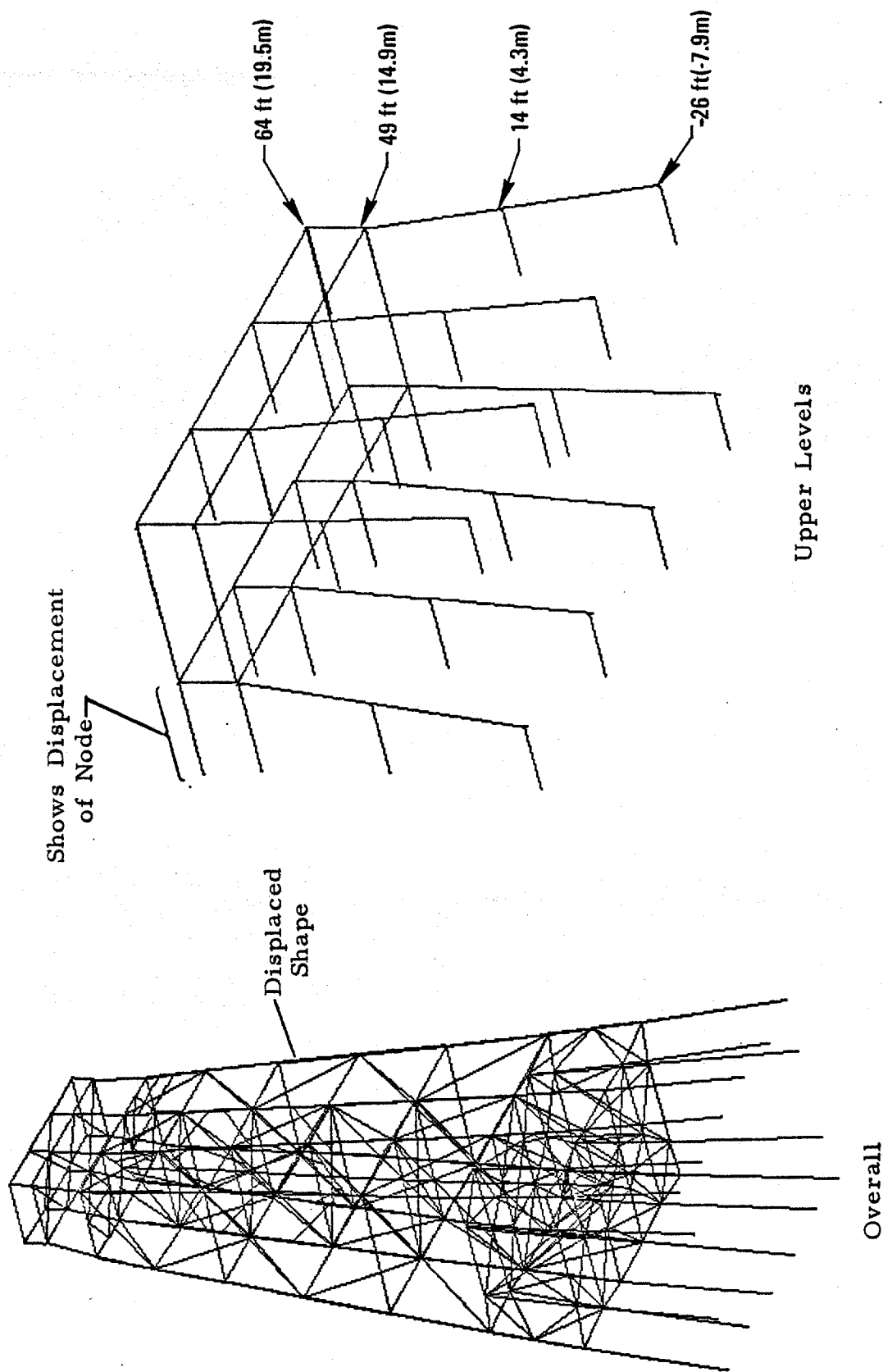
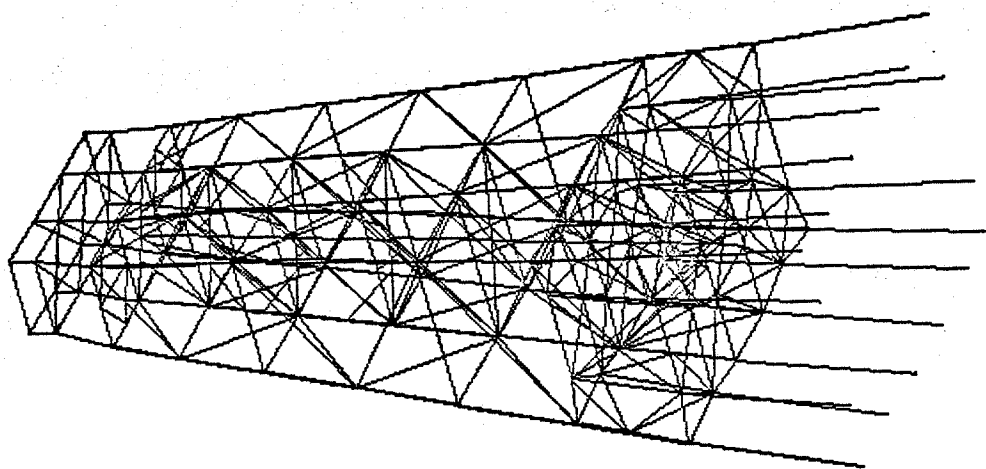
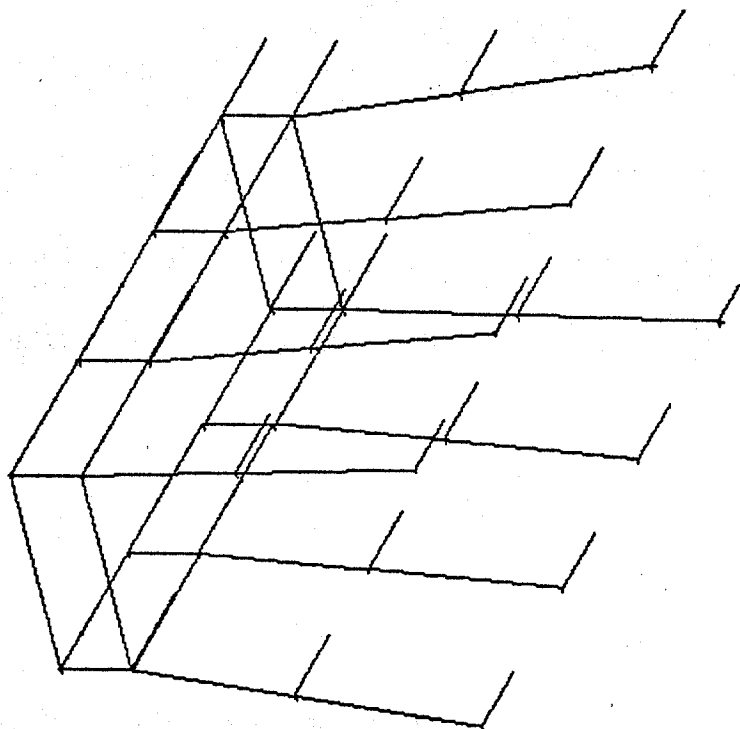


Figure B-1. Mode Shape 1, 0.639 Hz

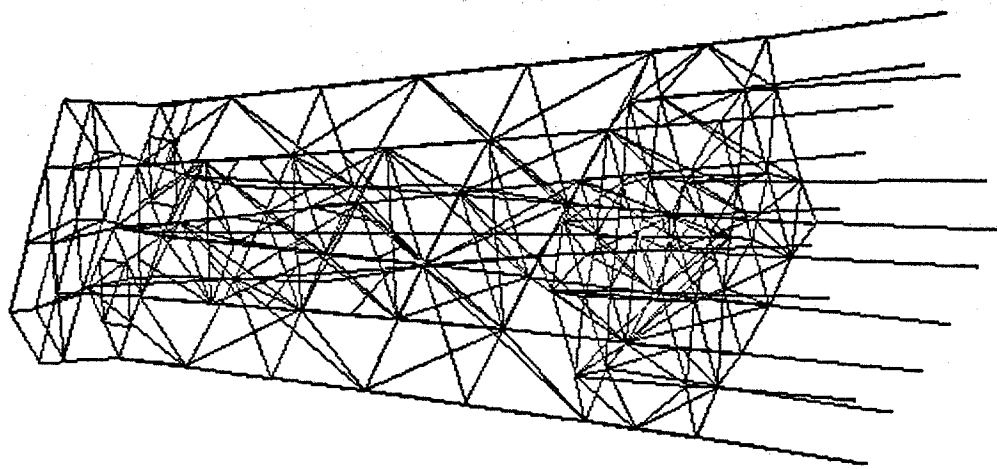


Overall

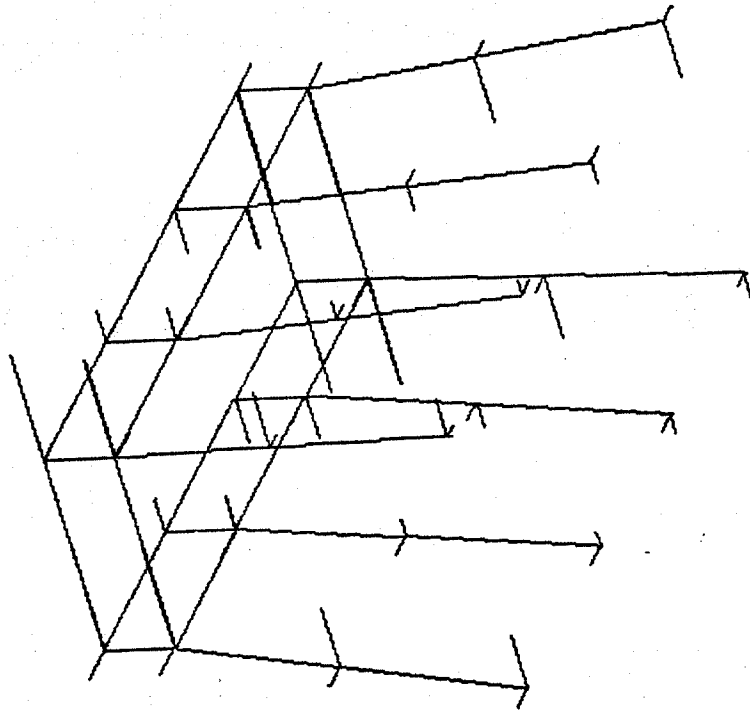


Upper Levels

Figure B-2. Mode Shape 2, 0.659 Hz

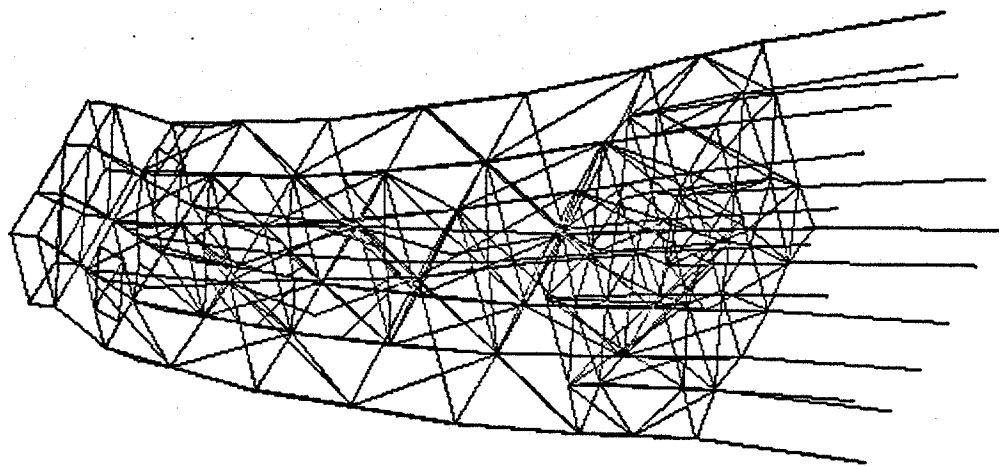


Overall

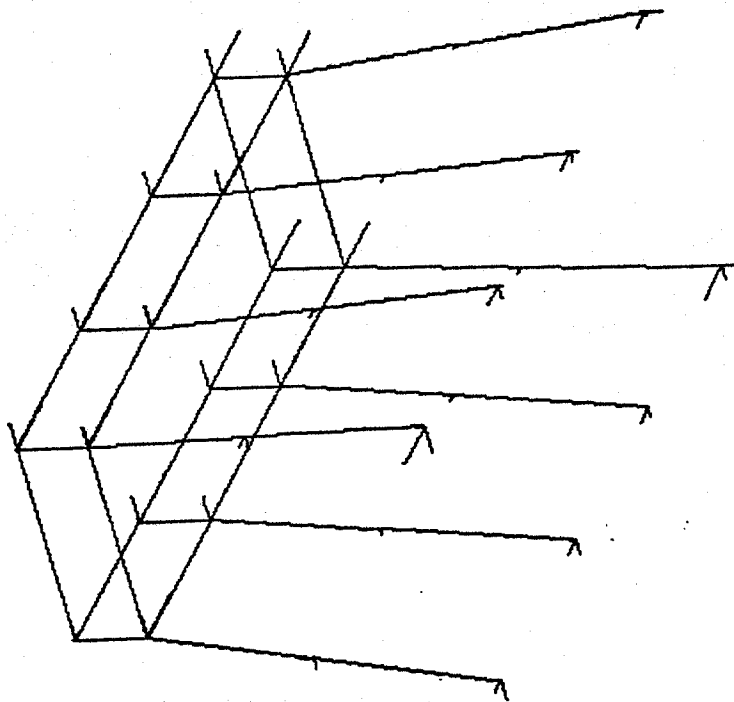


Upper Levels

Figure B-3. Mode Shape 3, 0.935 Hz

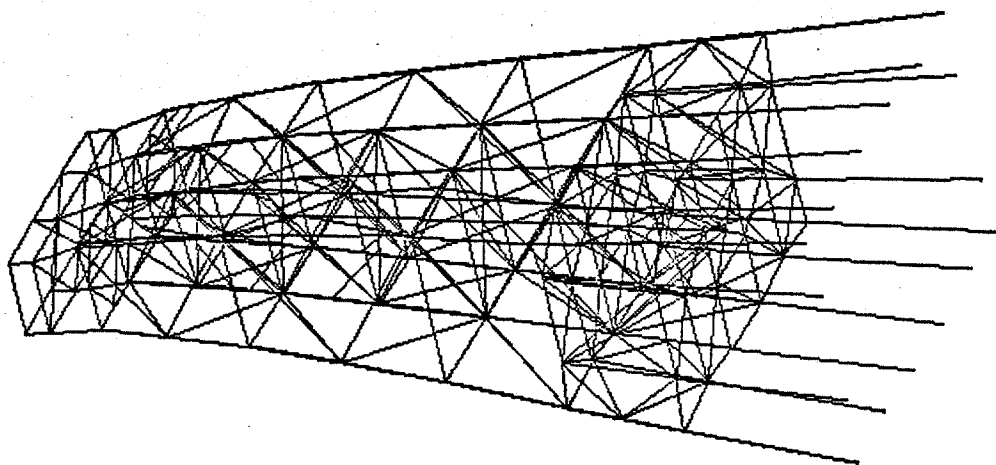


Overall

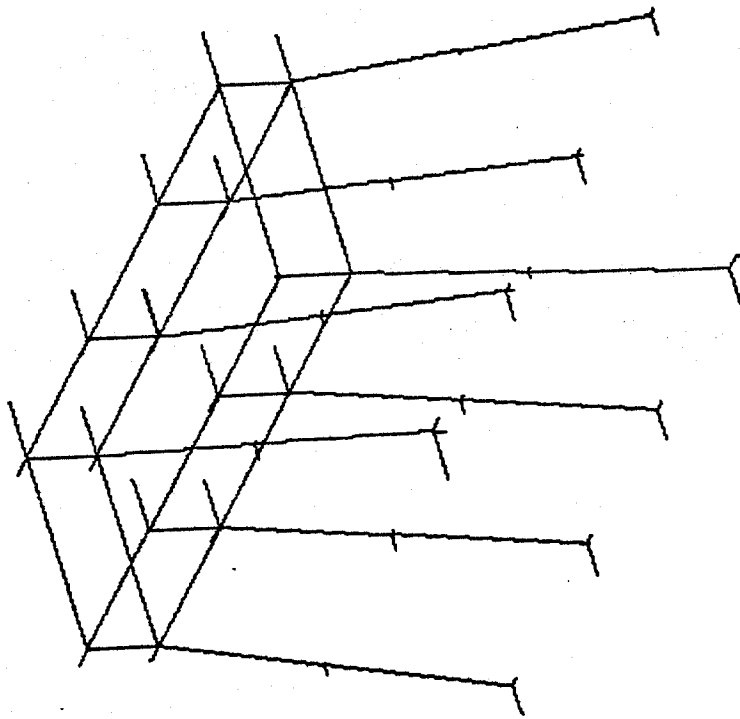


Upper Levels

Figure B-4. Mode Shape 4, 1.50 Hz

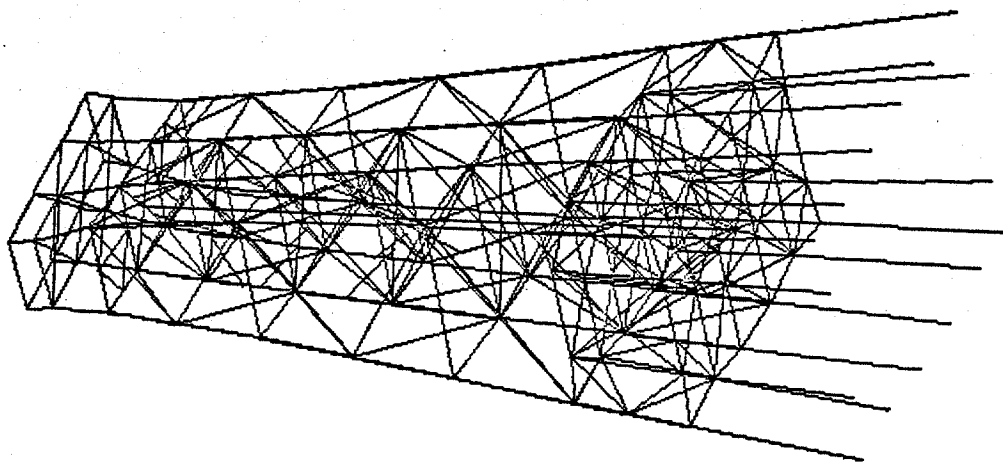


Overall

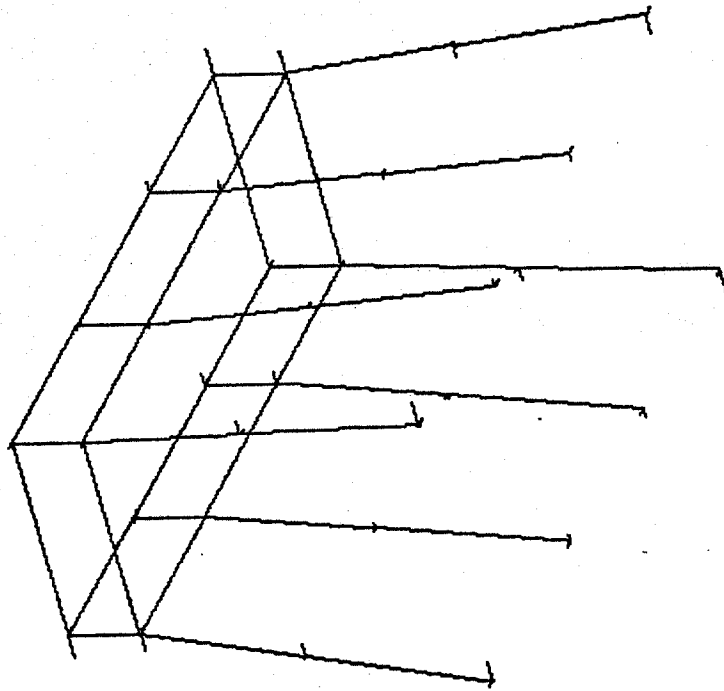


Upper Levels

Figure B-5. Mode Shape 5, 1.53 Hz



Overall



Upper Levels

B-6. Mode Shape 6, 1.69 Hz

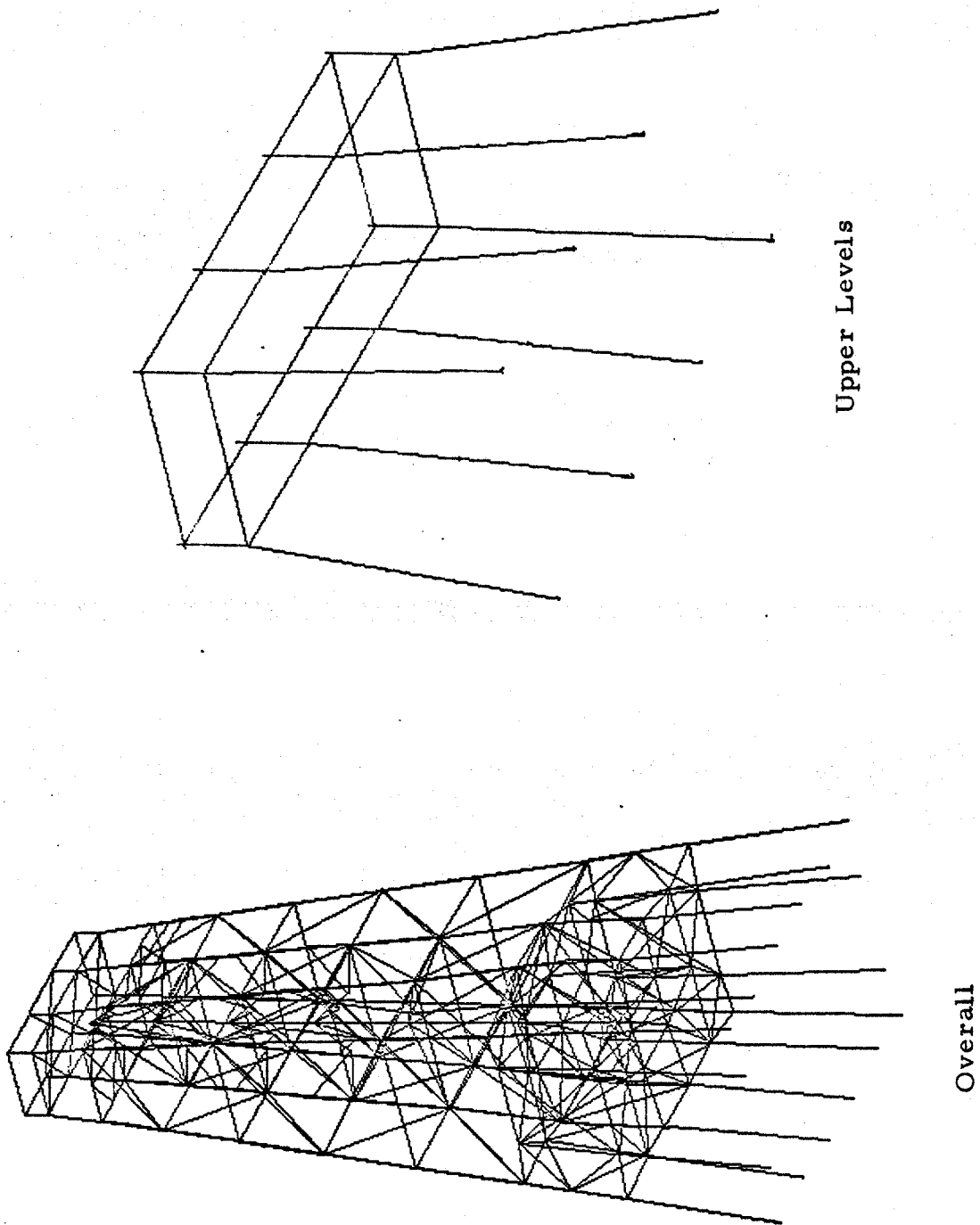
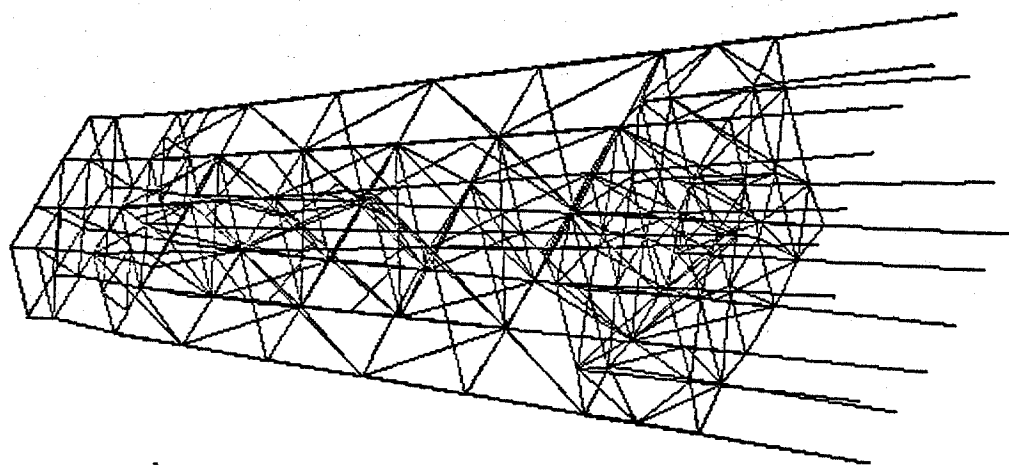
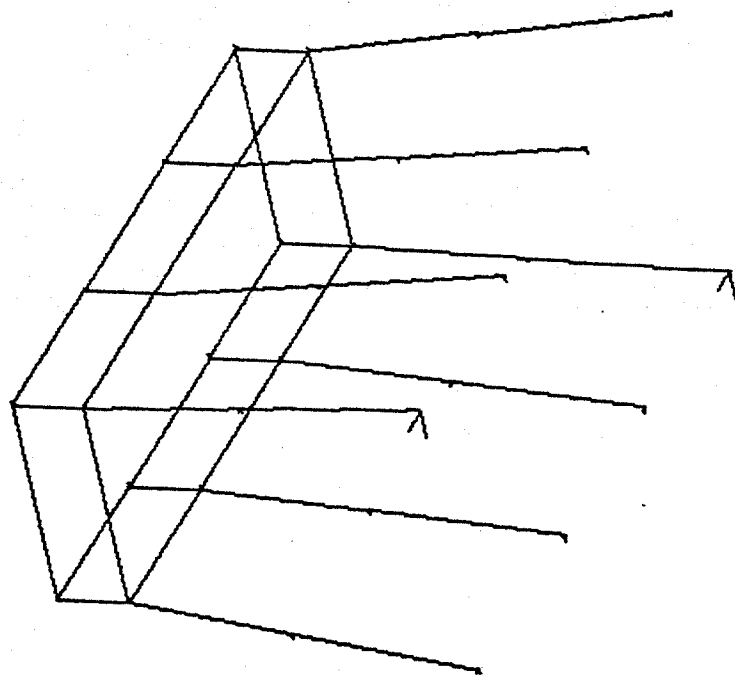


Figure B-7. Mode Shape 7, 1.85 Hz

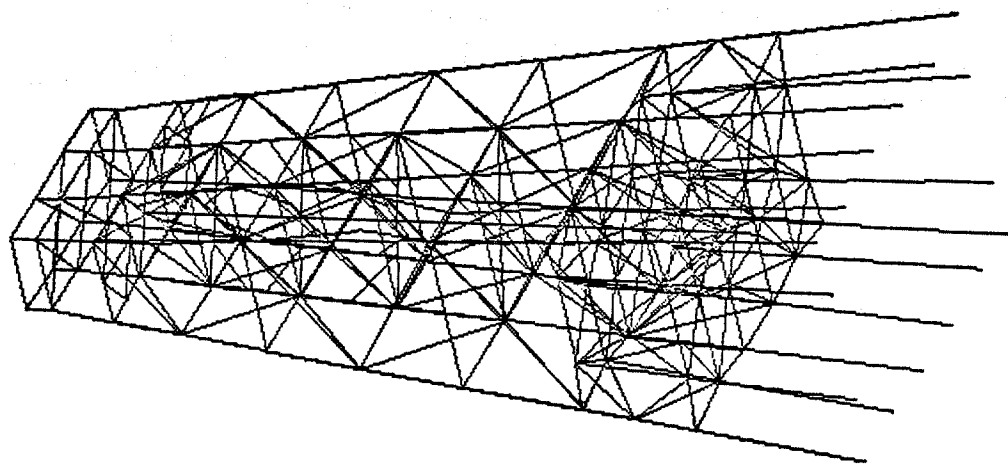


Overall

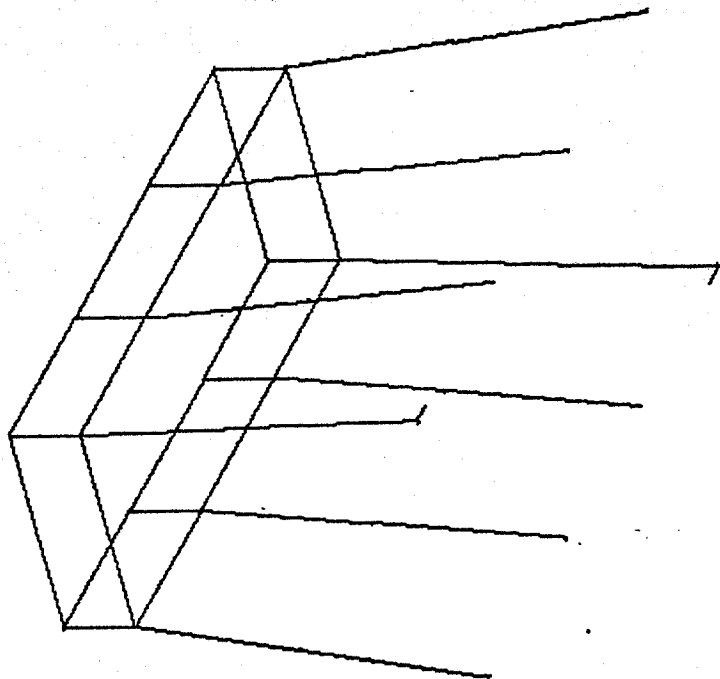


Upper Levels

B-8. Mode Shape 8 Configuration, 1.88 Hz



Overall



Upper Levels

Figure B-9. Mode Shape 9 Configuration, 1.89 Hz

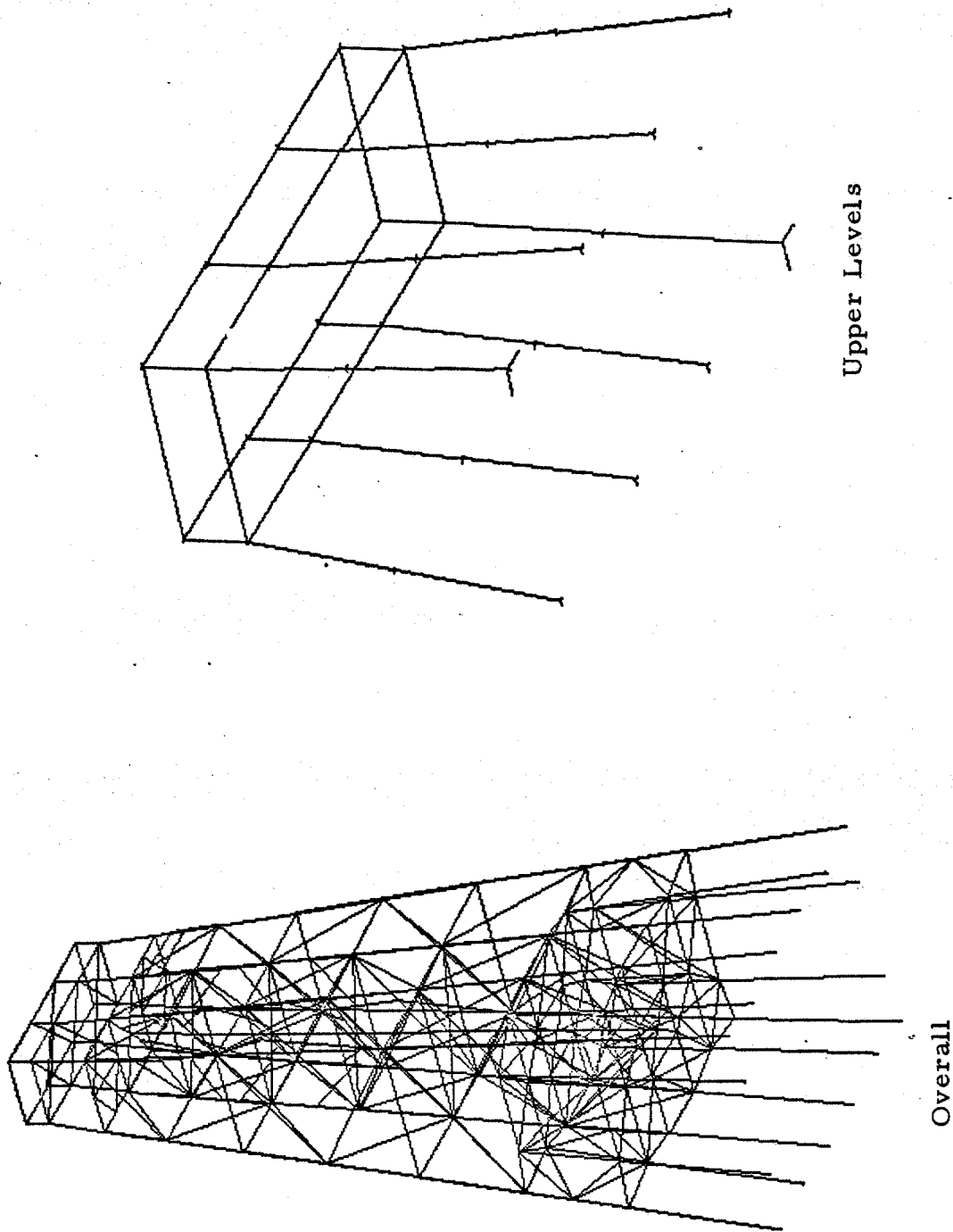
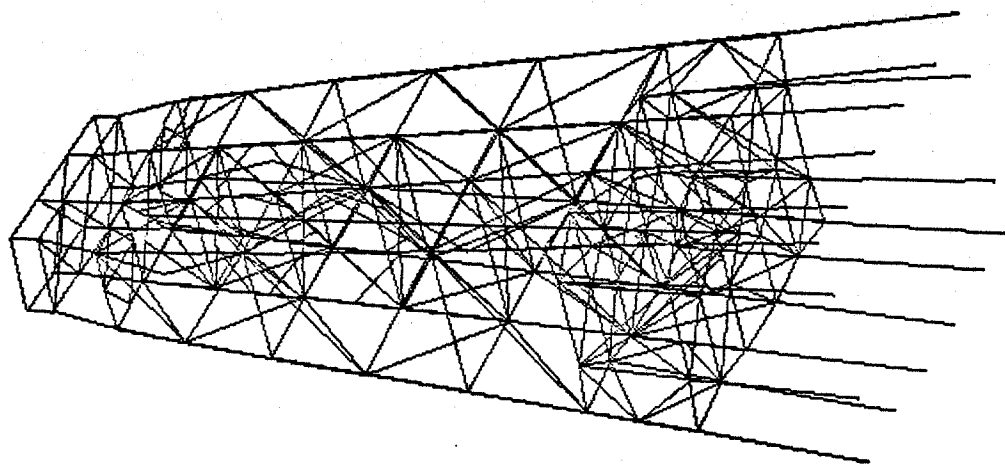
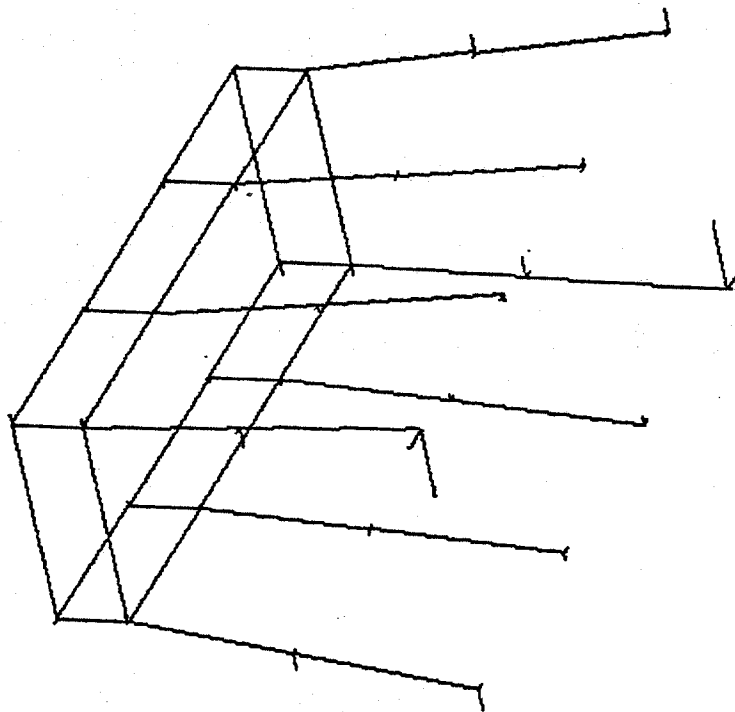


Figure B-10. Mode Shape 10, 1.92 Hz



Overall



Upper Levels

Figure B-11. Mode Shape 11, 2.00 Hz

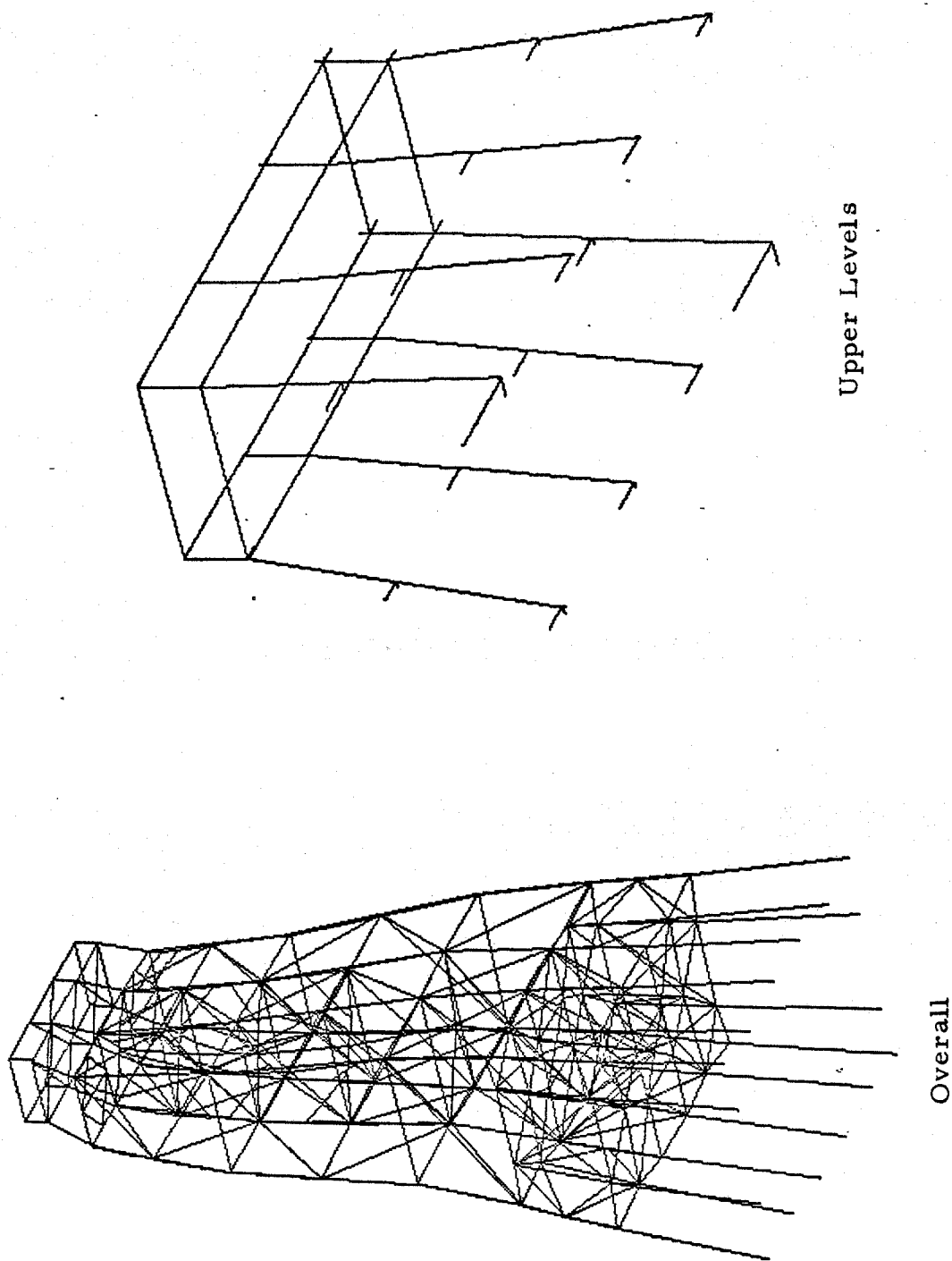
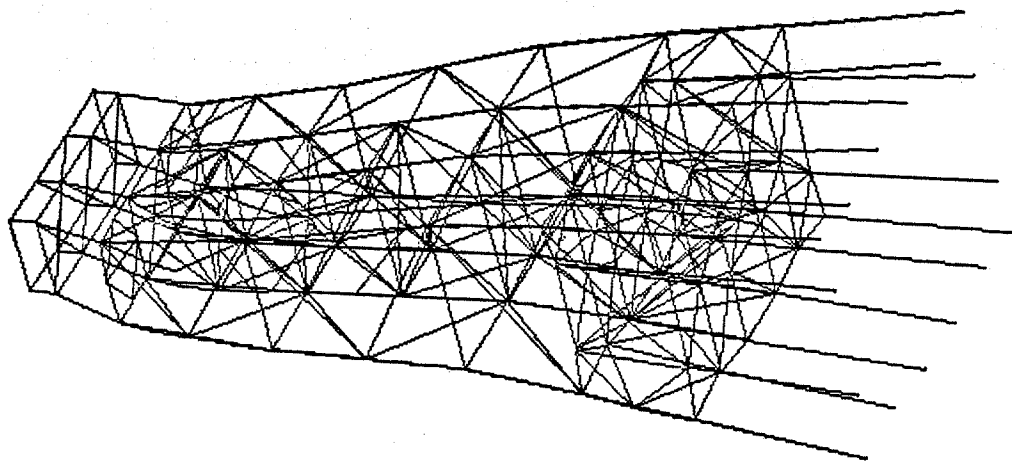
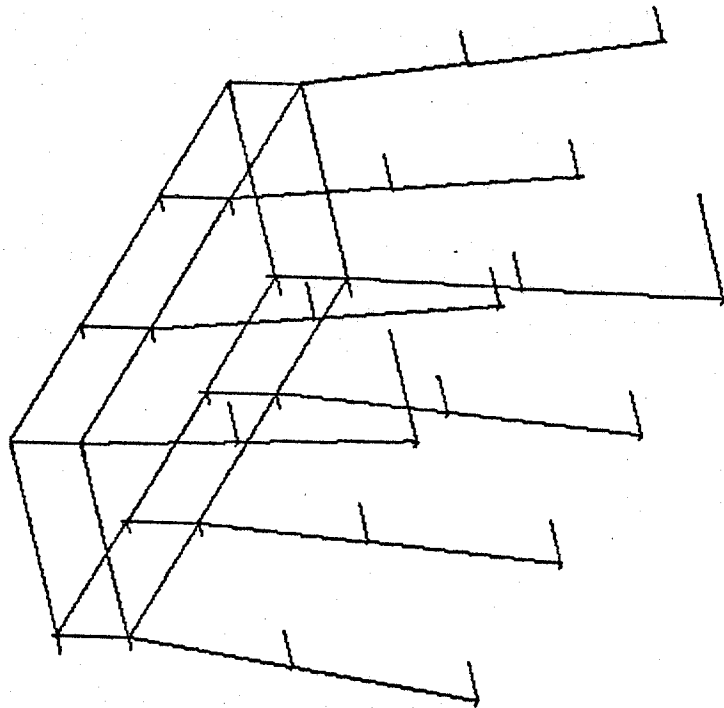


Figure B-12. Mode Shape 12, 2.43 Hz

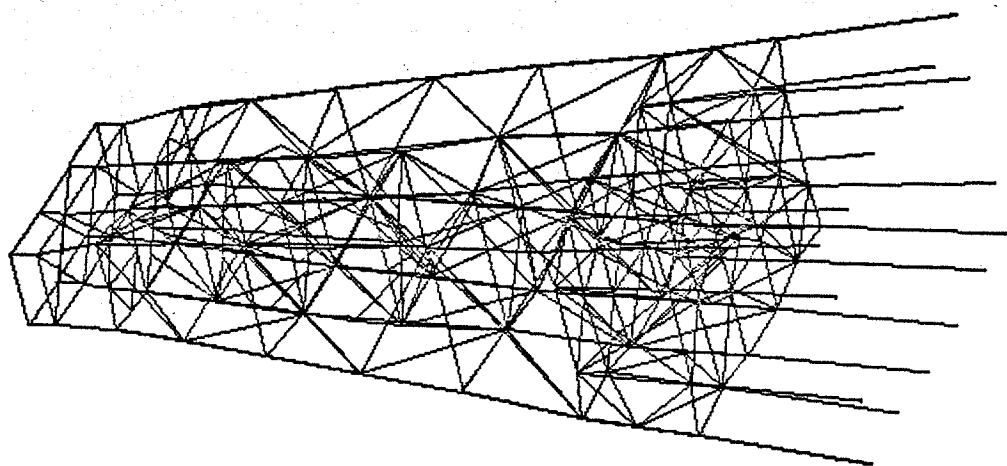


Overall

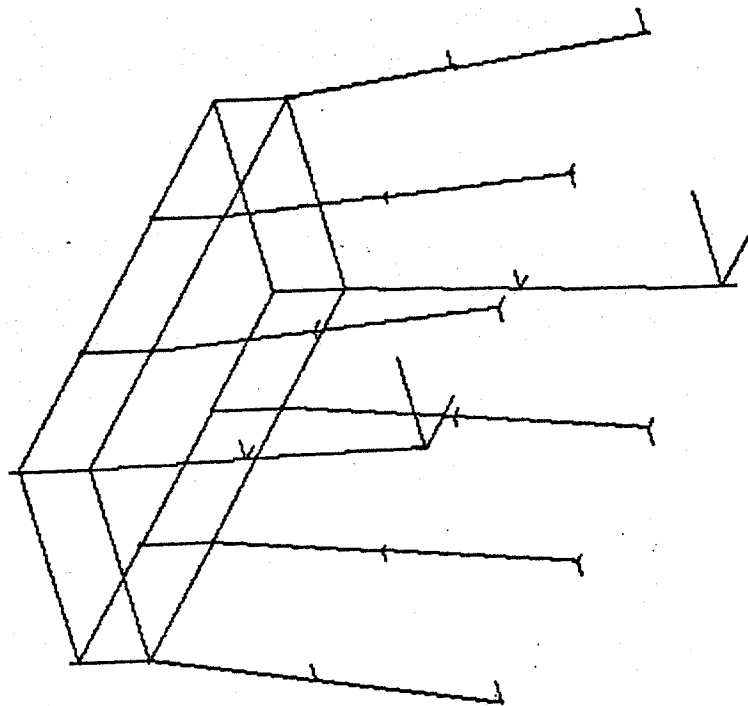


Upper Levels

Figure B-13. Mode Shape 13, 2.68 Hz

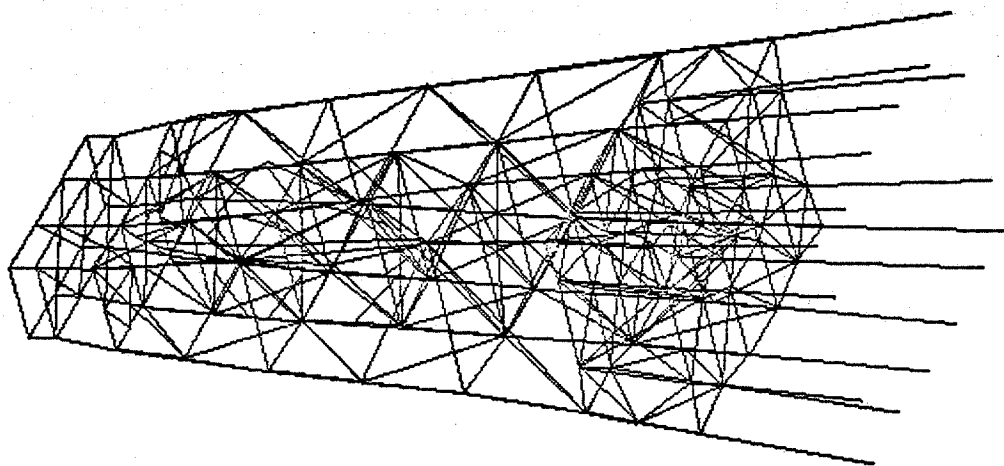


Overall

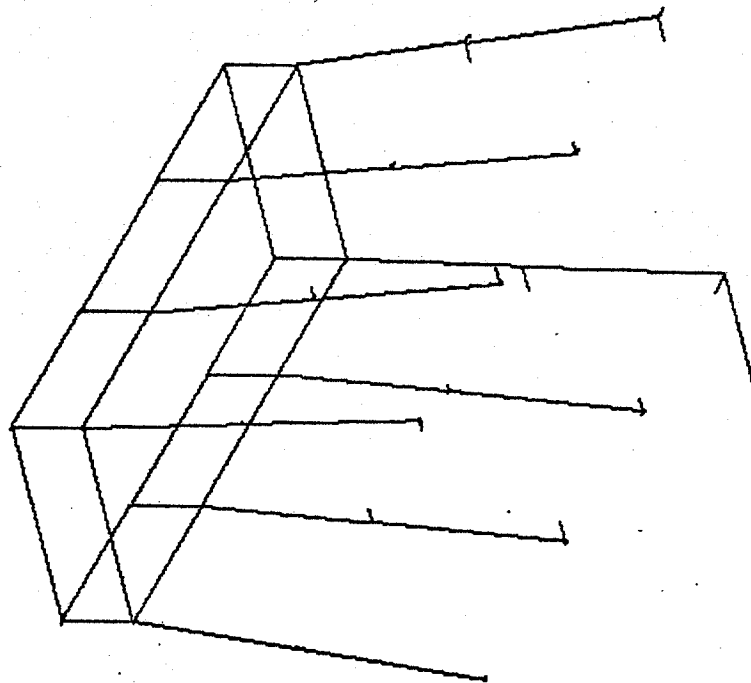


Upper Levels

Figure B-14. Mode Shape 14, 3.08 Hz

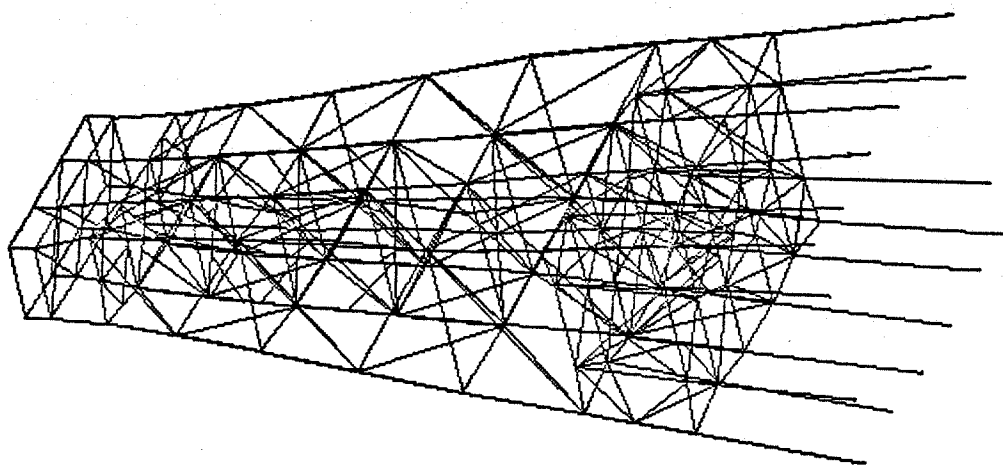


Overall

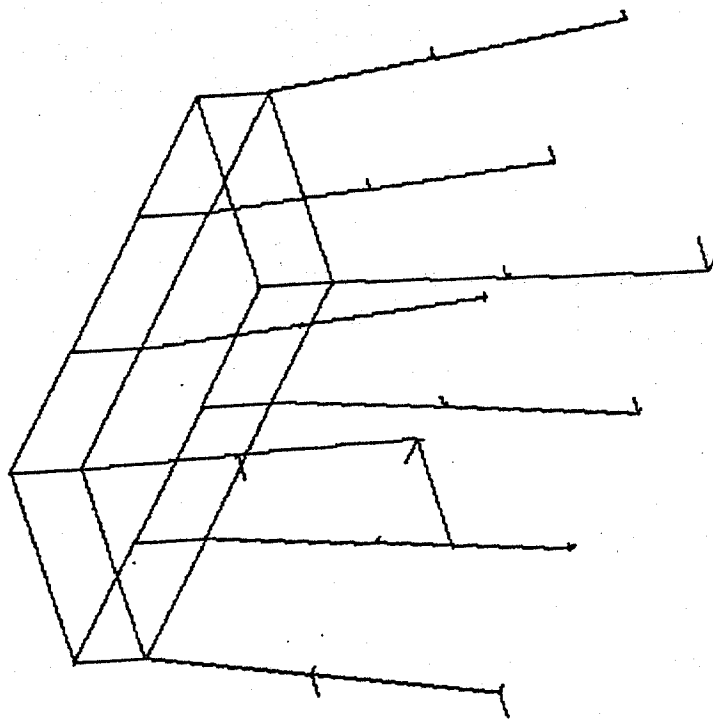


Upper Levels

Figure B-15. Mode Shape 15, 3.13 Hz



Overall



Upper Levels

Figure B-16. Mode Shape 16, 3.14 Hz

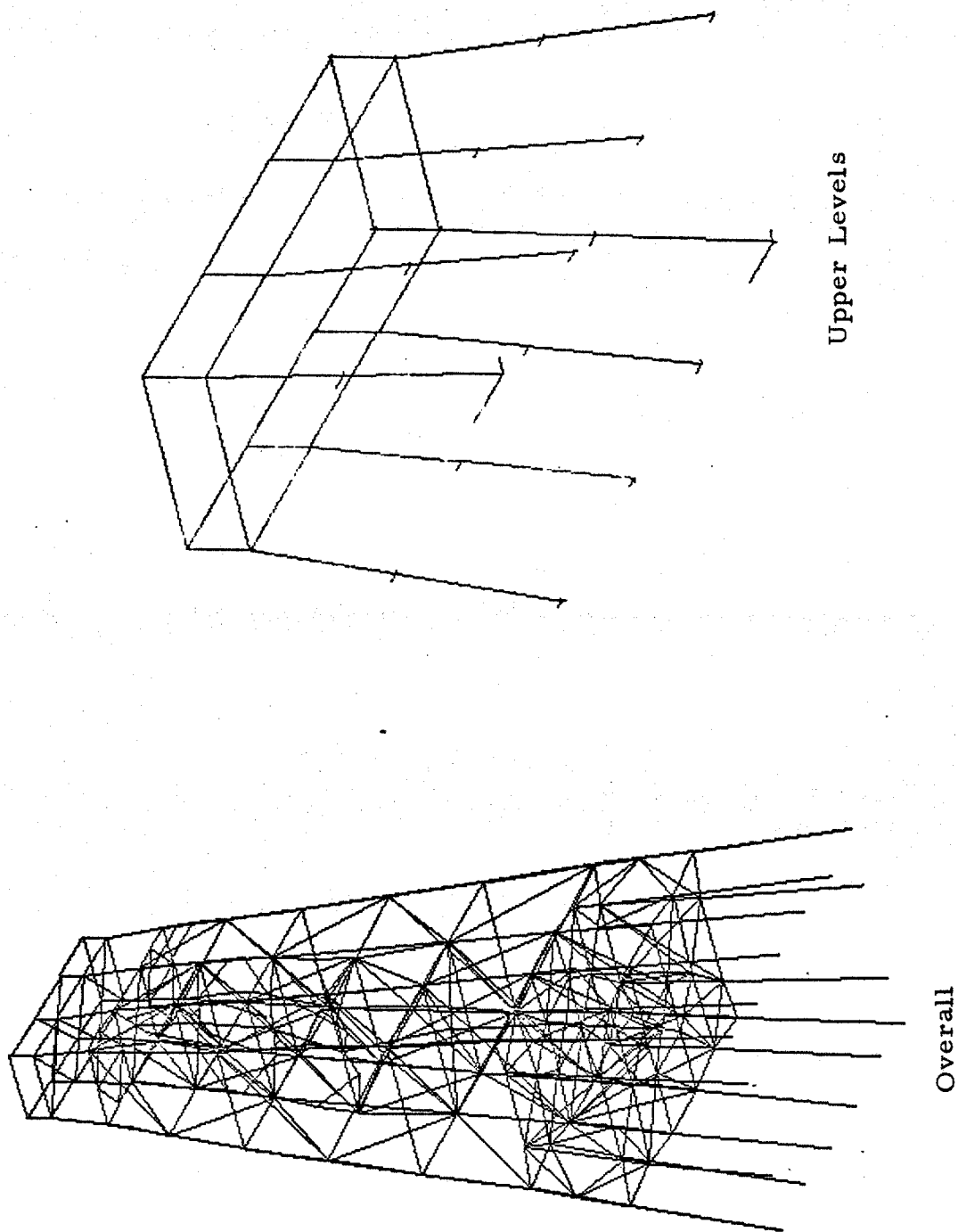
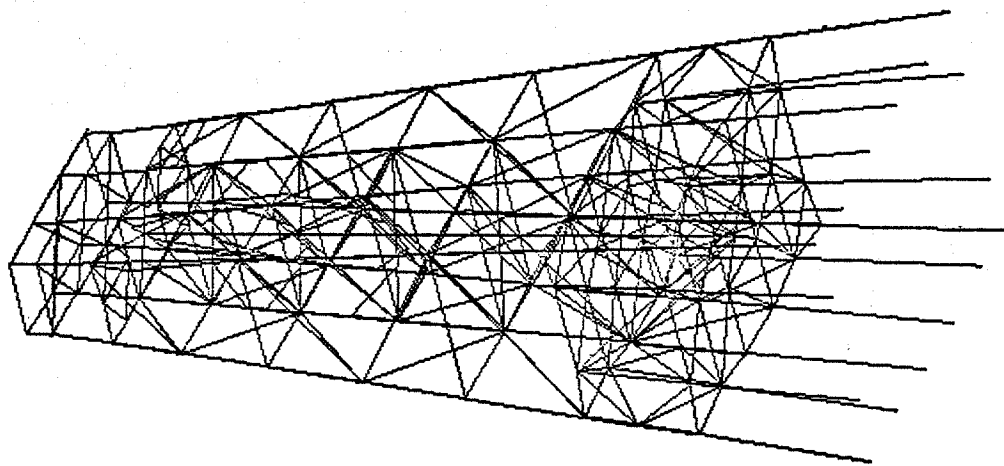
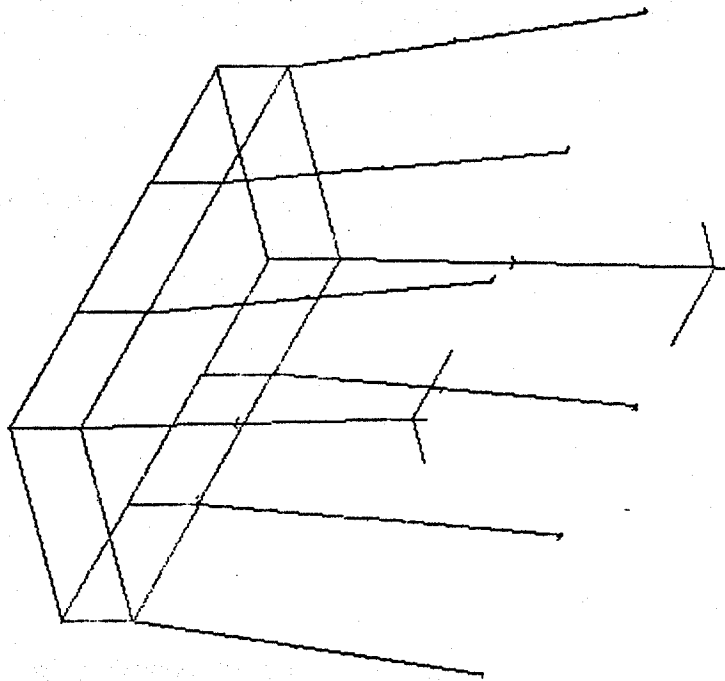


Figure B-17. Mode Shape 17, 3.28 Hz



Overall



Upper Levels

Figure B-18. Mode Shape 18, 3.53 Hz

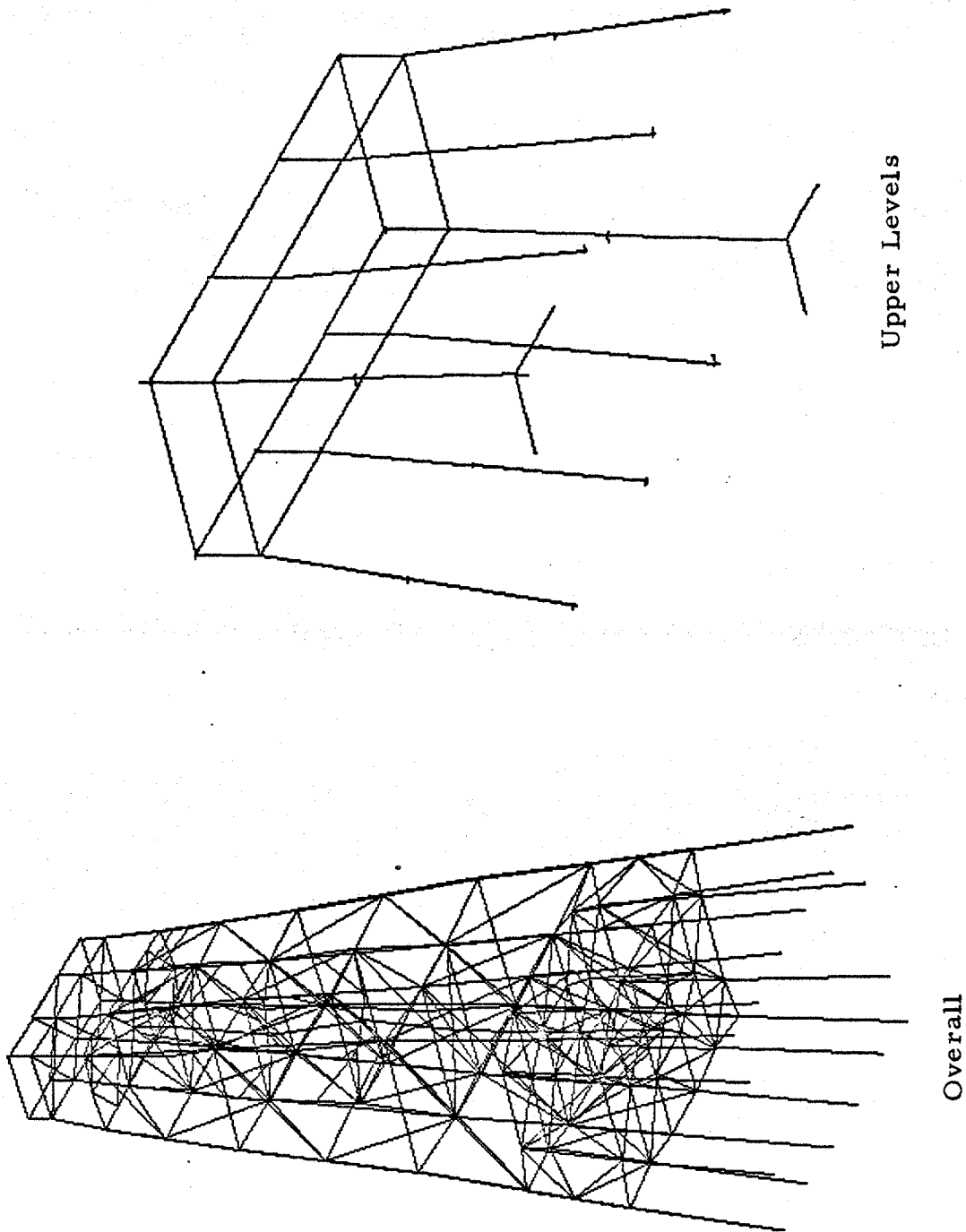


Figure B-19. Mode Shape 19, 3.71 Hz

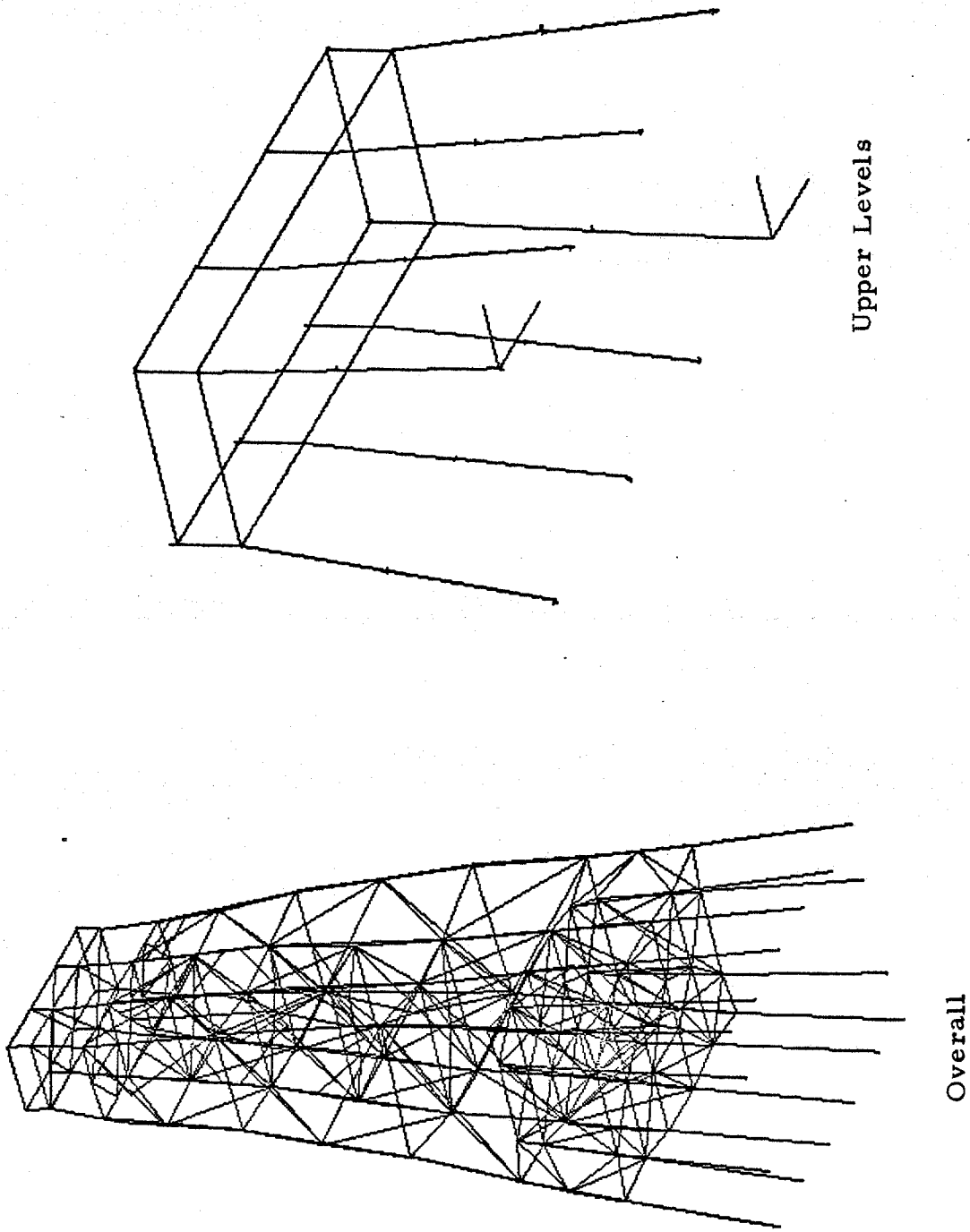
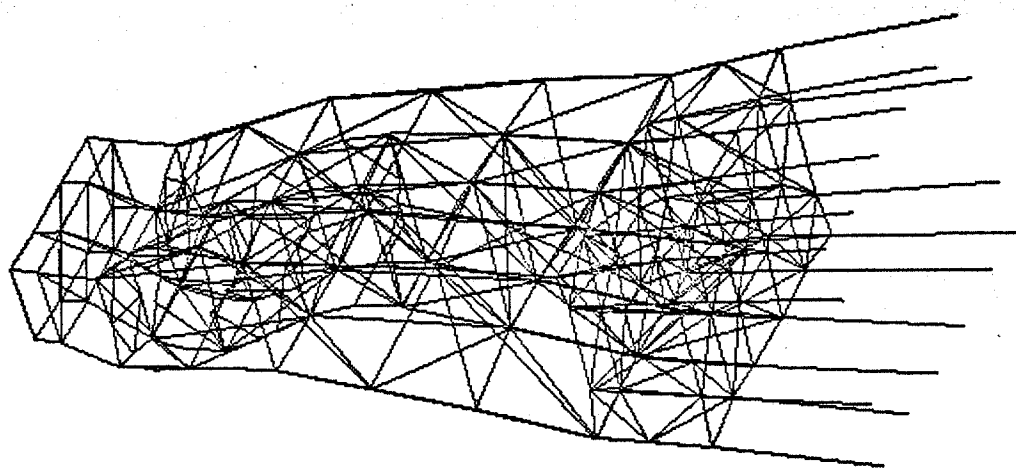
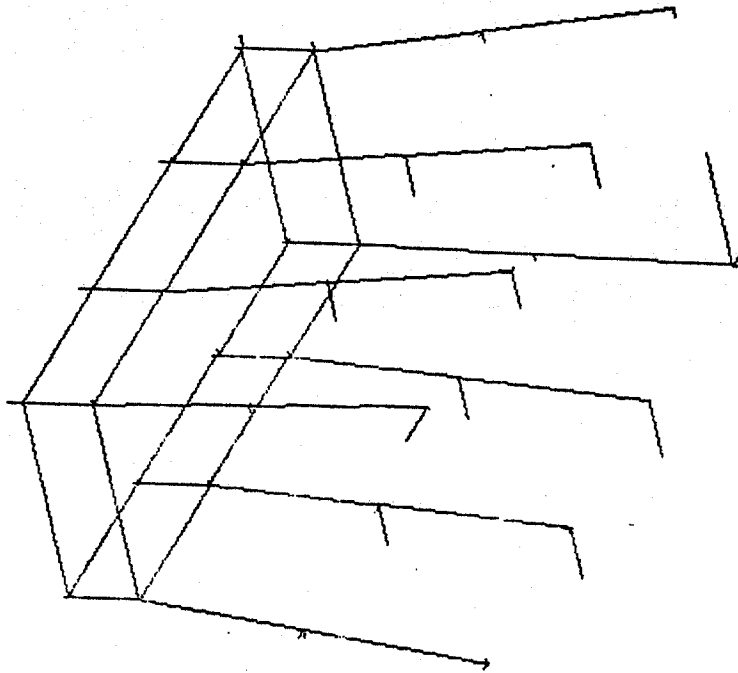


Figure B-20. Mode Shape 20, 3.81 Hz

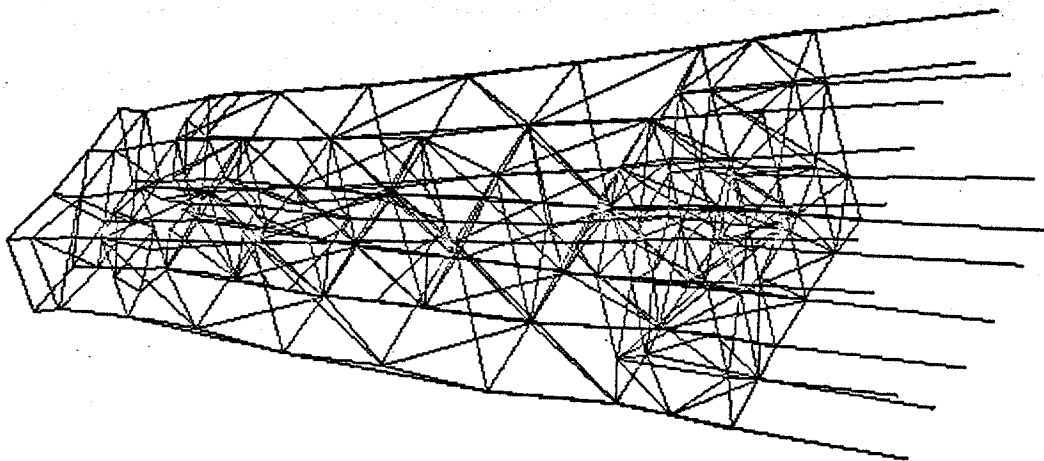


Overall

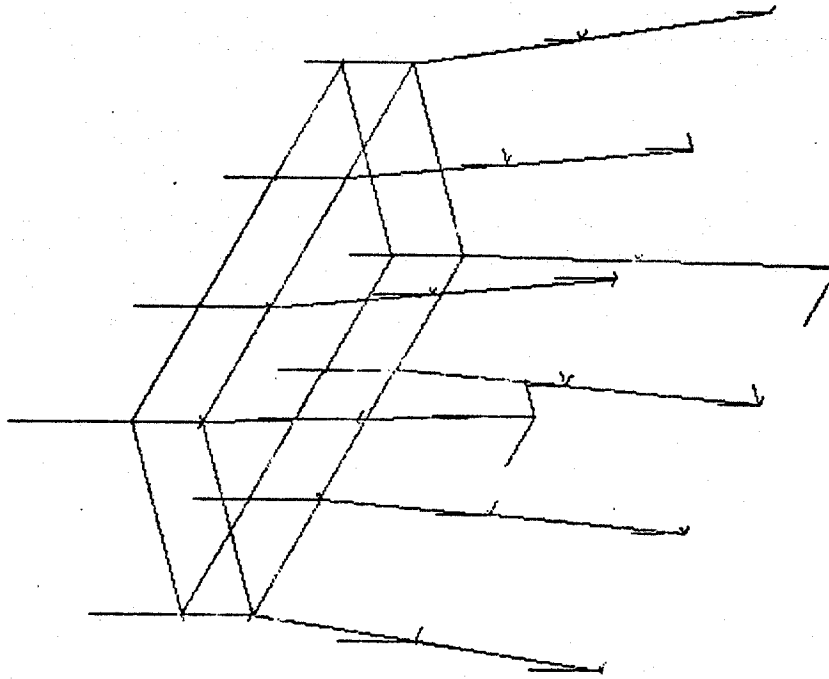


Upper Levels

Figure B-21. Mode Shape 21, 3.97 Hz



Overall



Upper Levels

Figure B-22. Mode Shape 22, 4.13 Hz

APPENDIX C

ACCELEROMETER TECHNOLOGY

APPENDIX C

ACCELEROMETER TECHNOLOGY

This appendix presents an introduction to the accelerometer technology suitable for the instrumentation of off-shore platforms. The discussion briefly describes the principles of operation of various types of instruments along with descriptions of typical designs and their performance. Both translational and angular accelerometers are discussed.

C. 1 SERVO REBALANCED (OR FORCE BALANCE)

Probably the most appropriate instrument for measuring translational accelerations associated with this application is the servo rebalanced hinged pendulum accelerometer. This type of instrument is diagrammed in Figure C-1. The sensor consists of a pendulum which is typically suspended relative to the instrument case by means of a flexure. The major mass of the pendulum is called the proof mass and it is equipped with a pick-off and a torquer. The pick-off is typically an electromagnetic device that continuously provides an electrical signal (voltage) which is proportional to the angular displacement of the pendulum relative to the sensor case. The sign of the voltage indicates the direction of the displacement from the pick-off midpoint (null). The torquer is a servo feedback element which when electrically excited with a DC current imparts a torque into the pendulum. The magnitude of the torque is proportional to the magnitude of the current, and the direction of the torque is controlled by the direction (sign) of the current. The servo loop is closed around the sensor by means of a set of capture electronics. This circuit accepts the pick-off signal and converts it to a feedback current which is continuously impressed on the torquer. The output of the accelerometer is a voltage proportional to the torquer rebalance current which is also proportional to input acceleration. To understand the operation of the system, consider the following. If the sensor is accelerated along its input axis, the proof mass will tend not to follow

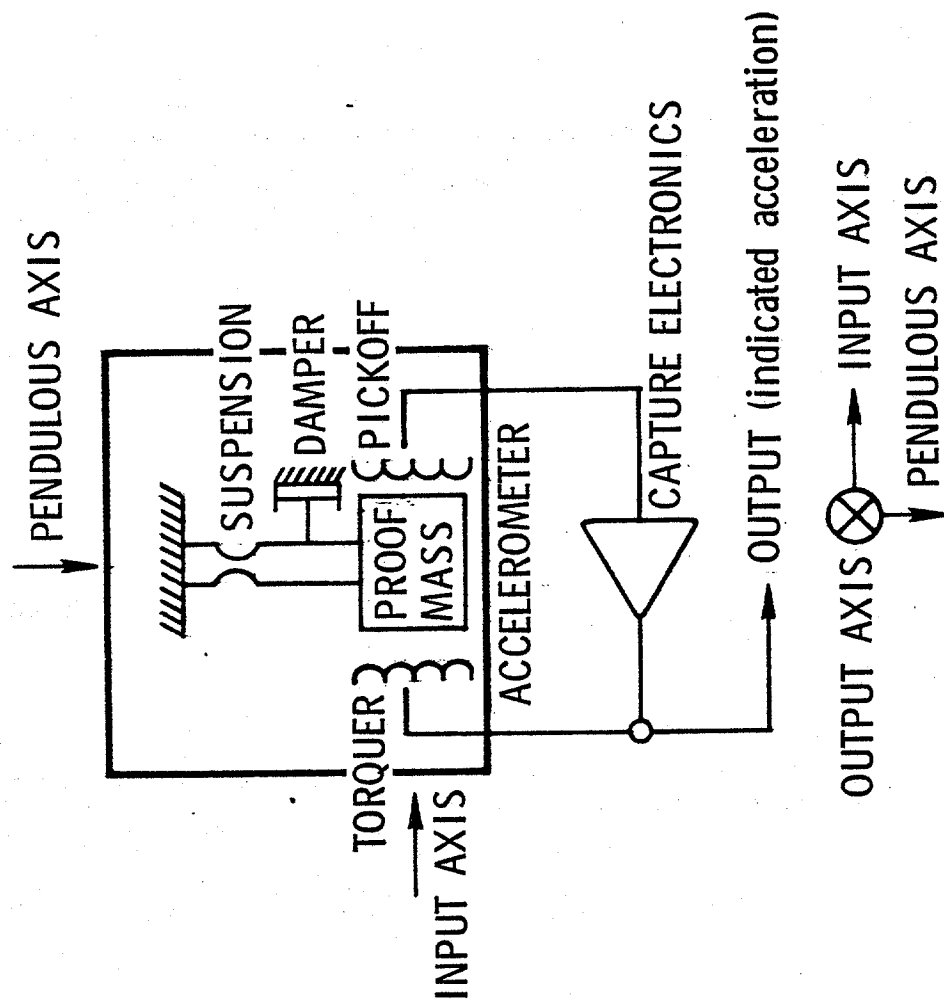


Figure C-1. Schematic Design of Hinged Pendulum Accelerometer

the case acceleration because the flexure suspension is deliberately made mechanically soft to force loads applied in this direction. The result is that the pendulum tends to move relative to the case in a direction opposite to that of the applied input acceleration. The pick-off provides a signal to the capture electronics which indicates the direction and magnitude of the instantaneous displacement. The electronics produce a current in the torquer applying a torque to the pendulum which tends to drive the pendulum back to the null (centered) position. The servo system thus described continuously tries to hold the pendulum at pick-off null and the resulting torquer current (which is easily converted to an output voltage) provides a direct measure of the input acceleration. When properly designed, this device is sensitive to accelerations applied along only one axis, the input axis. Ideally it is insensitive to inputs along any other axis. In most accelerometers the capture electronics are packaged inside the instrument case. Excitation voltage is applied to one pair of terminals and the output signal (indicated acceleration) appears on another terminal pair.

This type of instrument is particularly well suited to this application. It has a frequency response from 0 to an upper level which can be selected over the range from 10 to several hundred Hz. The scale factor stability is determined by the torquer current sensitivity which in most instruments is controlled by the stability of a permanent magnet field. The resulting stability is much better than that required for this application, typically 0.01%. Similarly the bias stability is considerably better than required for this application. The resolution and threshold of the device are typically better than 1 ppm of full scale which for a 1 g full scale instrument is 1 μ g and is considerably better than that required for this application.

The outline drawn of a typical accelerometer suitable for this application is shown in Figure C-2. This unit is manufactured by Sunstrand and is their model No. QA 1300. The unit is self-contained and utilizes a fused quartz flexure and a permanent magnet torquer. The unit is small and

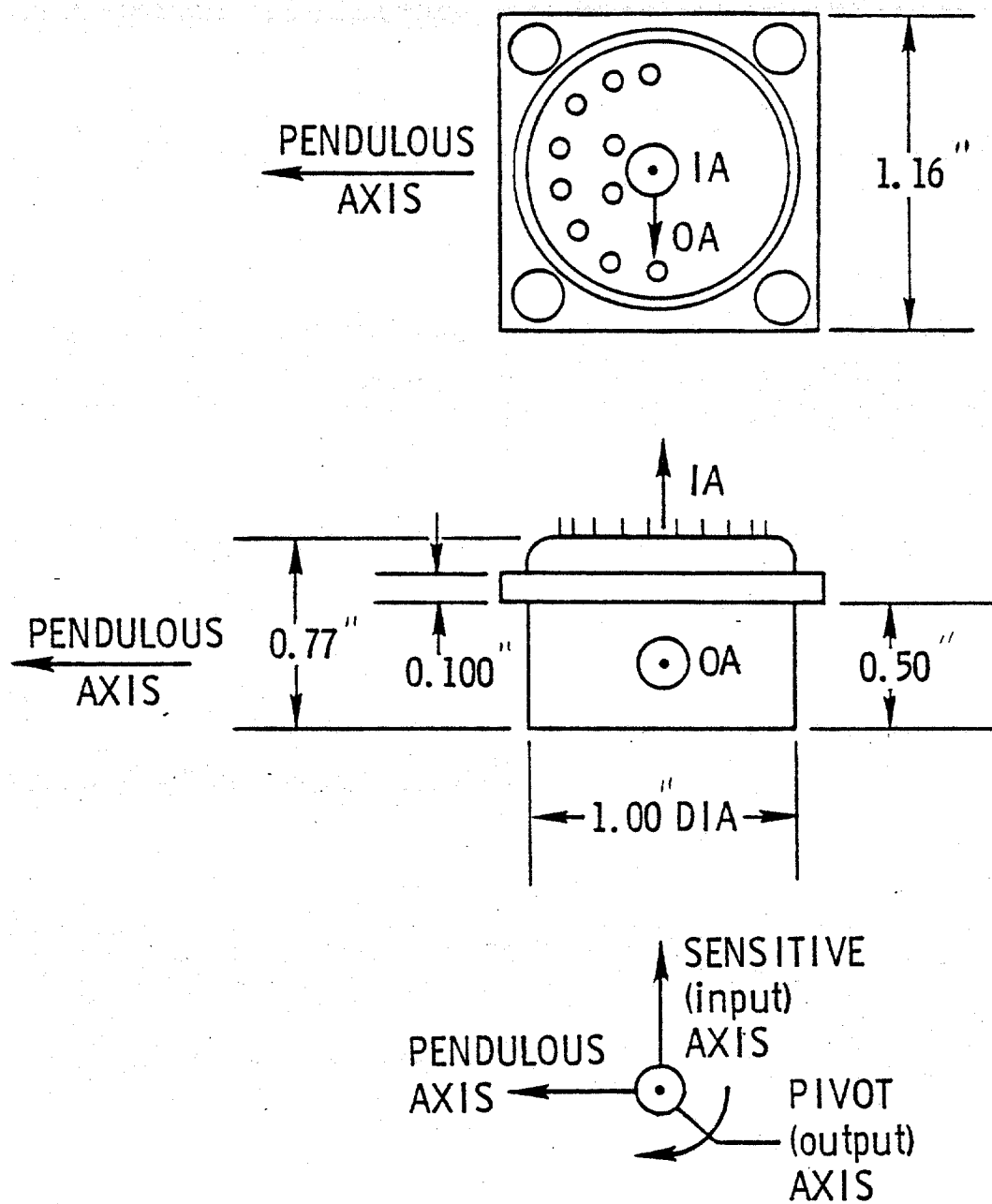


Figure C-2. Sunstrand QA 1300 Accelerometer

extremely rugged. It has been used extensively in numerous space applications and has been successfully subjected to severe environmental testing. Characteristics for this unit are listed below:

Range	$\pm 2.5 \text{ g}$
Scale Factor	5 V/g
Threshold/ Resolution	1 μg
Bias Stability	100 μg
Scale Factor Stability	100 ppm
Frequency Response	0 to 300 Hz
Noise 0-10 Hz	0.003 μg rms
0-50 Hz	0.03 μg rms

C. 2 PIEZOELECTRIC TRANSLATIONAL ACCELEROMETERS

Another type of accelerometer which may be useful in this application in the future is the piezoelectric accelerometer. In this instrument the proof mass is attached to the case by means of a piezoelectric beam. When the case is accelerated the beam is stressed and produces an output voltage proportional to the stress. No pick-off or servo loop is required. At the present time their performance is not as good as that of the servo rebalanced types. Endevco Corporation manufactures these units and indicates that a number of breakthroughs have been made, and hence the performance of these devices is improving rapidly. These instruments are inherently bandpass sensors with the lower cutoff which has recently been reduced to about 0.1 Hz. With careful filtering, the noise can be held to about 50 μg . This technology should be carefully examined, especially for use in an operational system since, with its inherent simplicity, improvements in system reliability and lower cost could probably be realized, provided that the other performance requirements can be met.

C.3 ANGULAR ACCELEROMETERS

Traditionally these devices have not had the scope of application enjoyed by translational accelerometers, and hence their development has received considerably less emphasis. Some years ago Systron Donner developed a novel design approach for such an instrument. The device consists of a servo rebalanced paddle which is similar in configuration to the hinged pendulum described above. In this case, the center of gravity of the paddle assembly is installed in a torroidal shaped chamber which is filled with fluid. A picture of the fluid container is shown in Figure C-3. If the unit is accelerated angularly about an axis perpendicular to the plane of the torroid, the fluid contained therein tends to remain stationary relative to the instrument case and, hence, appears to rotate relative to the case. In so doing, it impinges upon the paddle which upsets the paddle servo, producing an output voltage. This output is directly proportional to angular acceleration. The device is essentially insensitive to translational accelerations applied along any axis. An outline drawing of their model No. 4590F is shown in Figure C-4 and a summary of these characteristics is listed below:

Range	$\pm 0.25 \text{ rad/s}^2$
Scale Factor	$7.5 \text{ V/}(\text{rad/s}^2)$
Bandwidth	0 to 15 Hz
Noise	5 mV rms
Dynamic Range	greater than 100 dB
Weight	3 lb
Power	0.3 watts

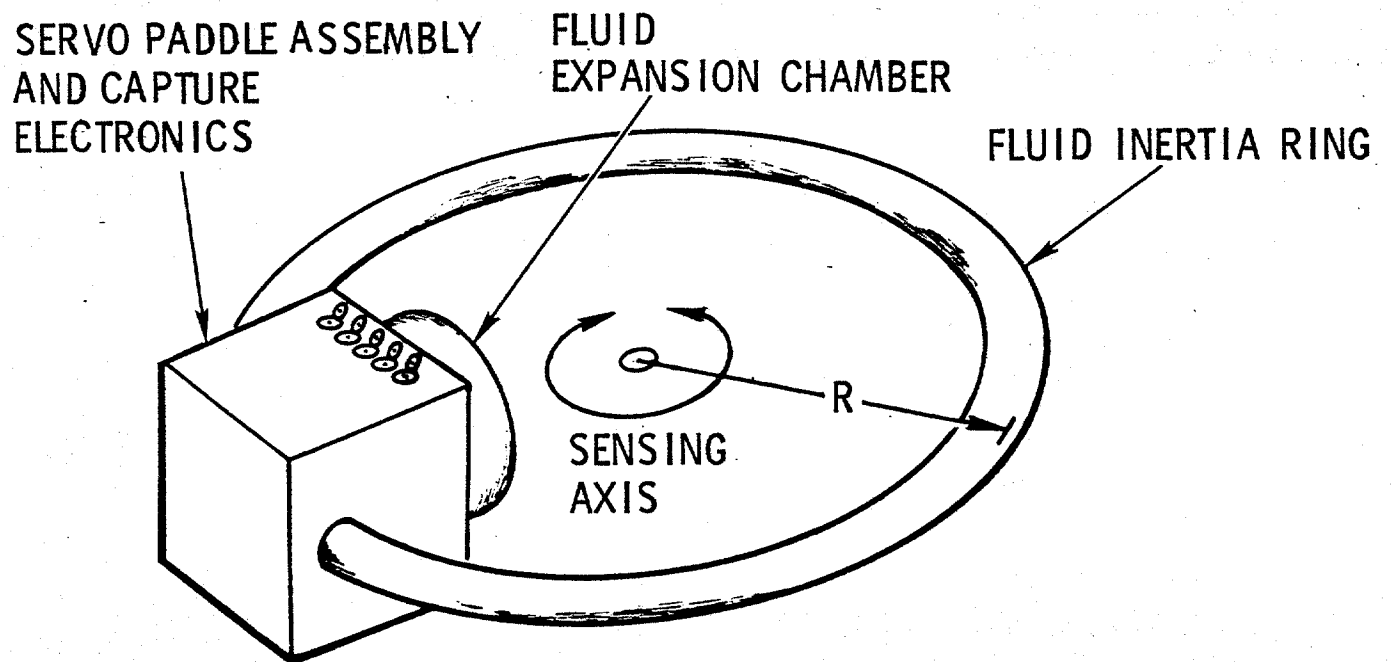


Figure C-3. Schematic of the Systron Donner Angular Accelerometer

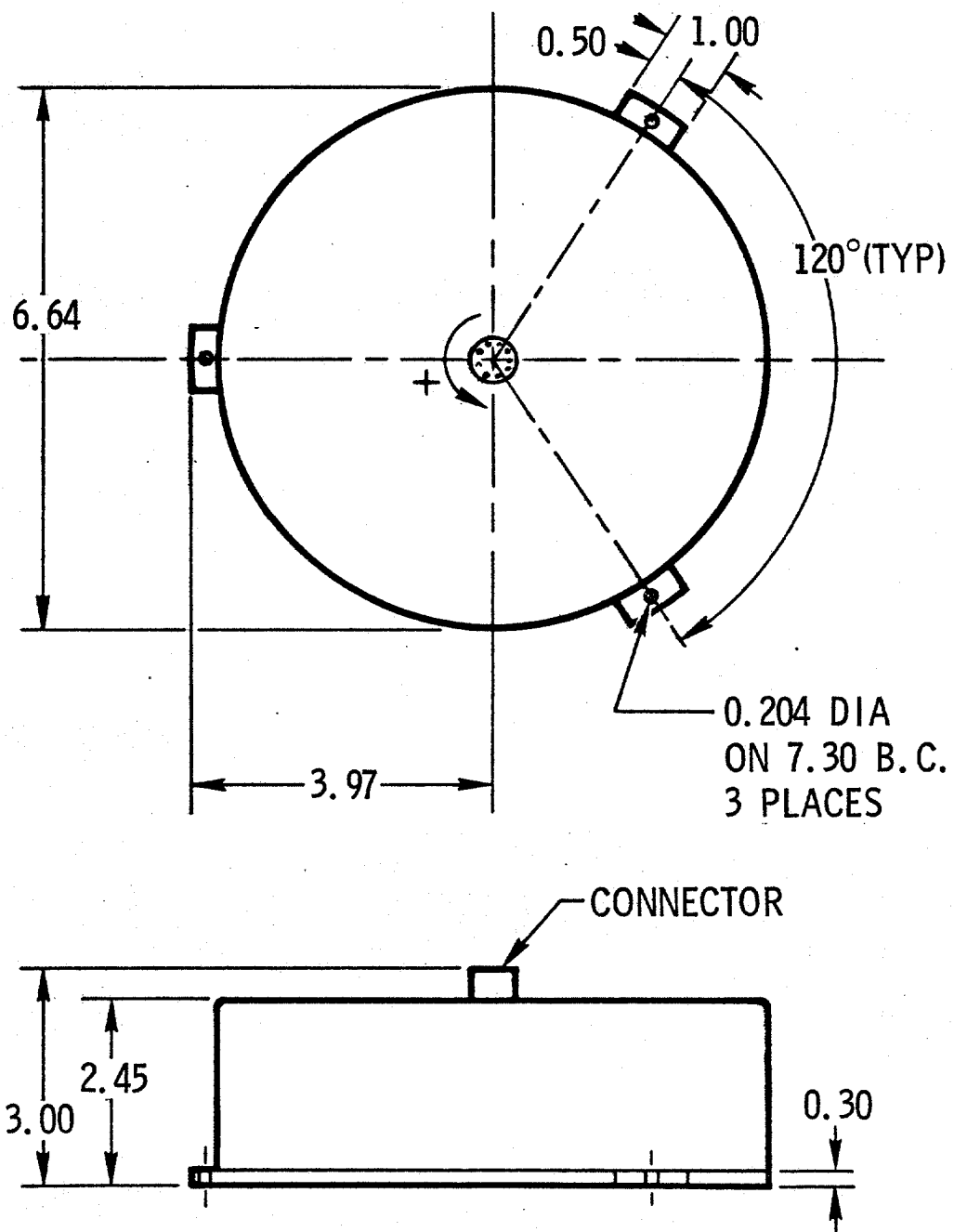


Figure C-4. Systron Donner Model 4590F Angular Accelerometer

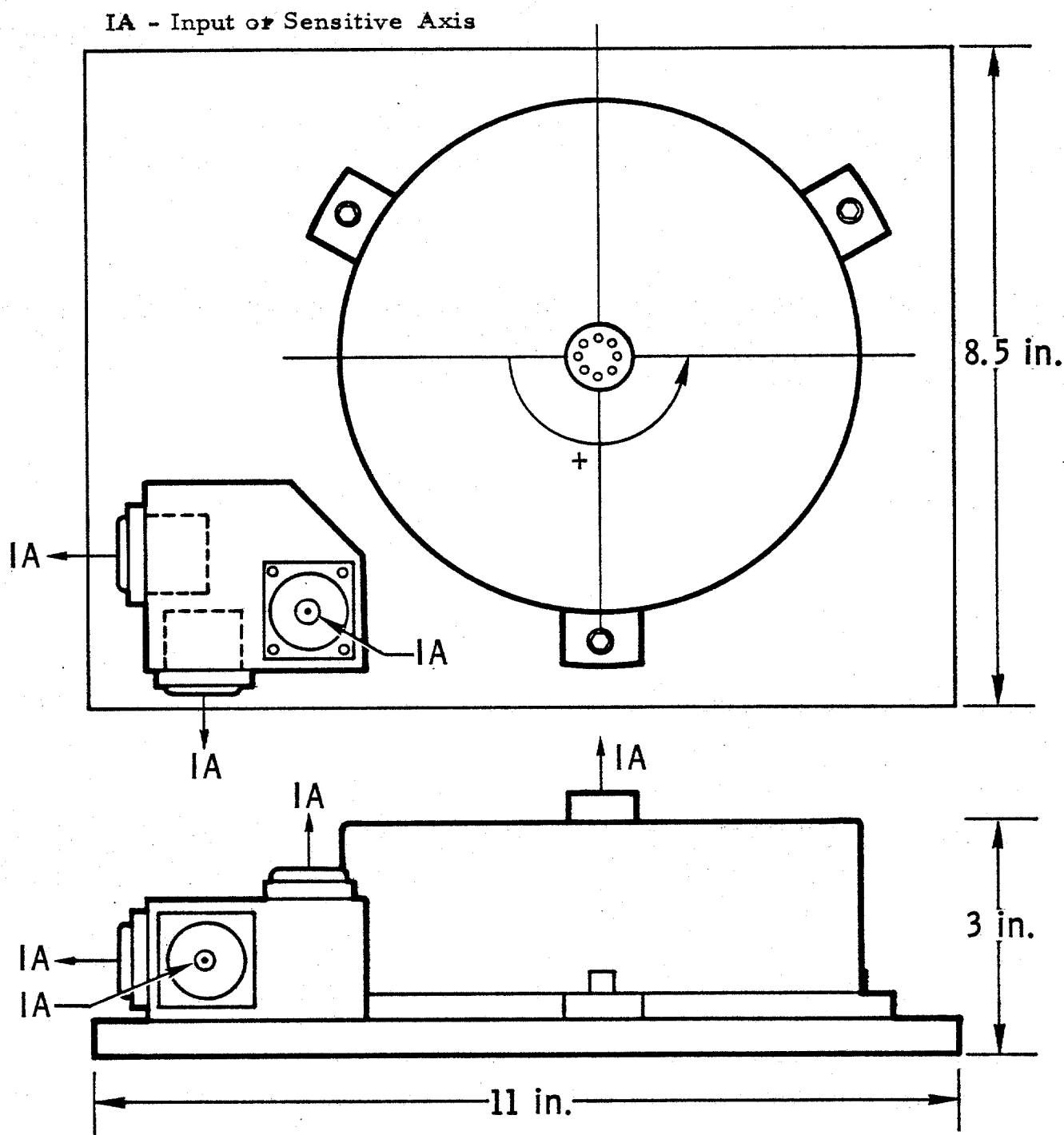


Figure C-5 Mounting of Three Translational and One Angular Accelerometer

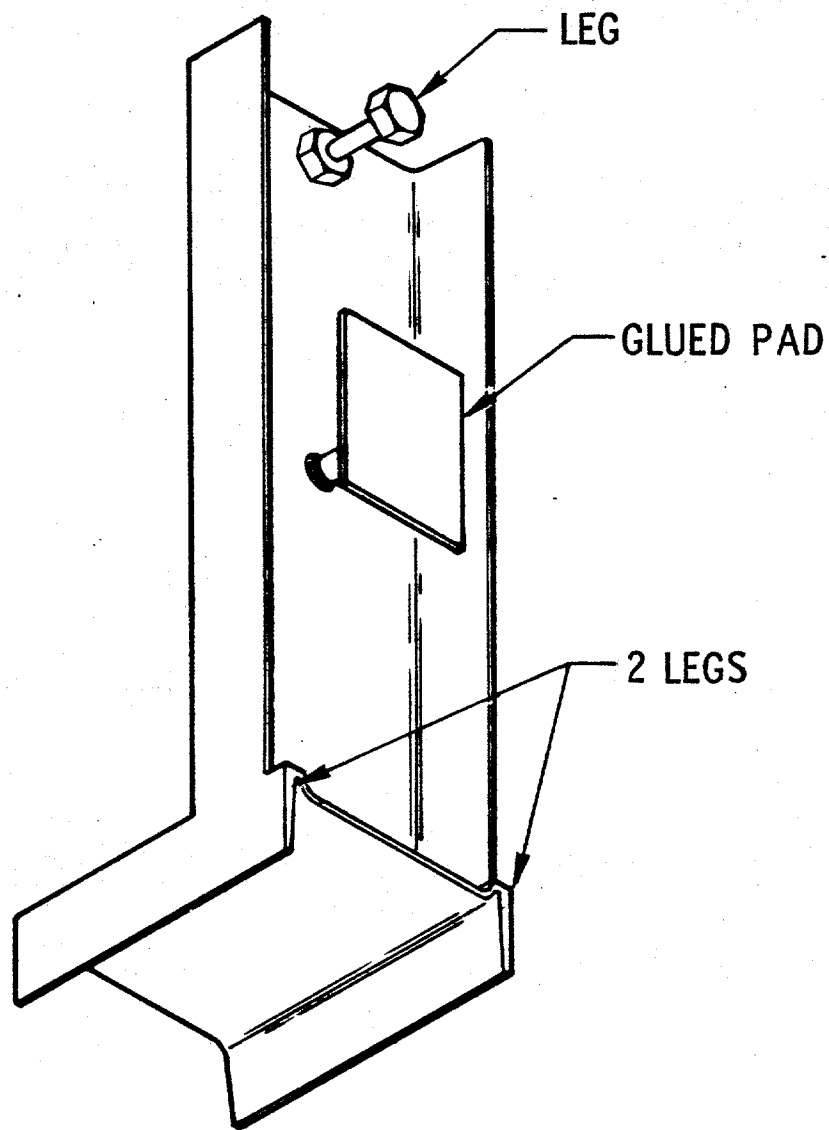


Figure C-6 Rear View of the Accelerometer Illustrating the Glued Pad and Mounting Legs

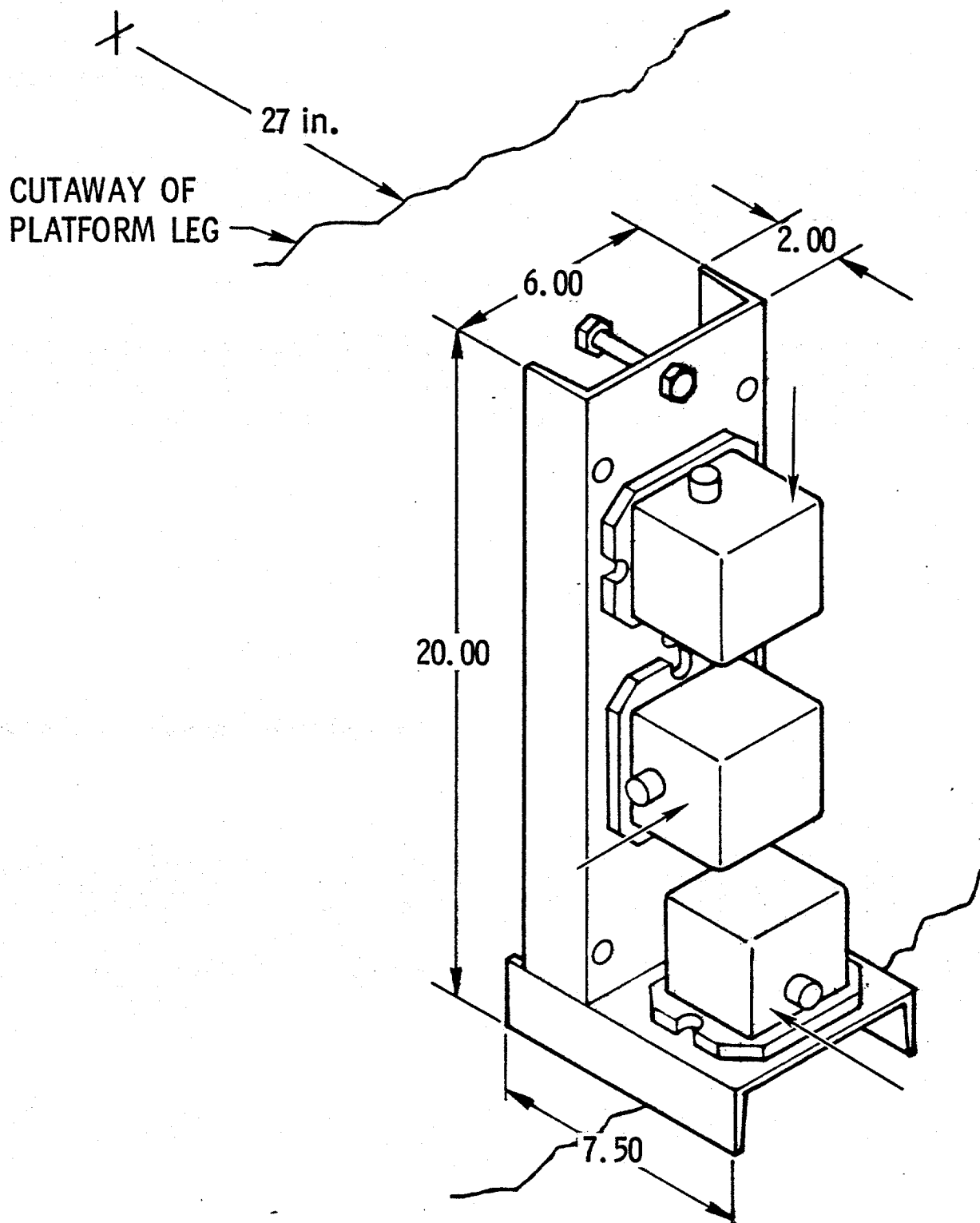


Figure C-7. Mounting Fixture With Three FBA-1 Accelerometers

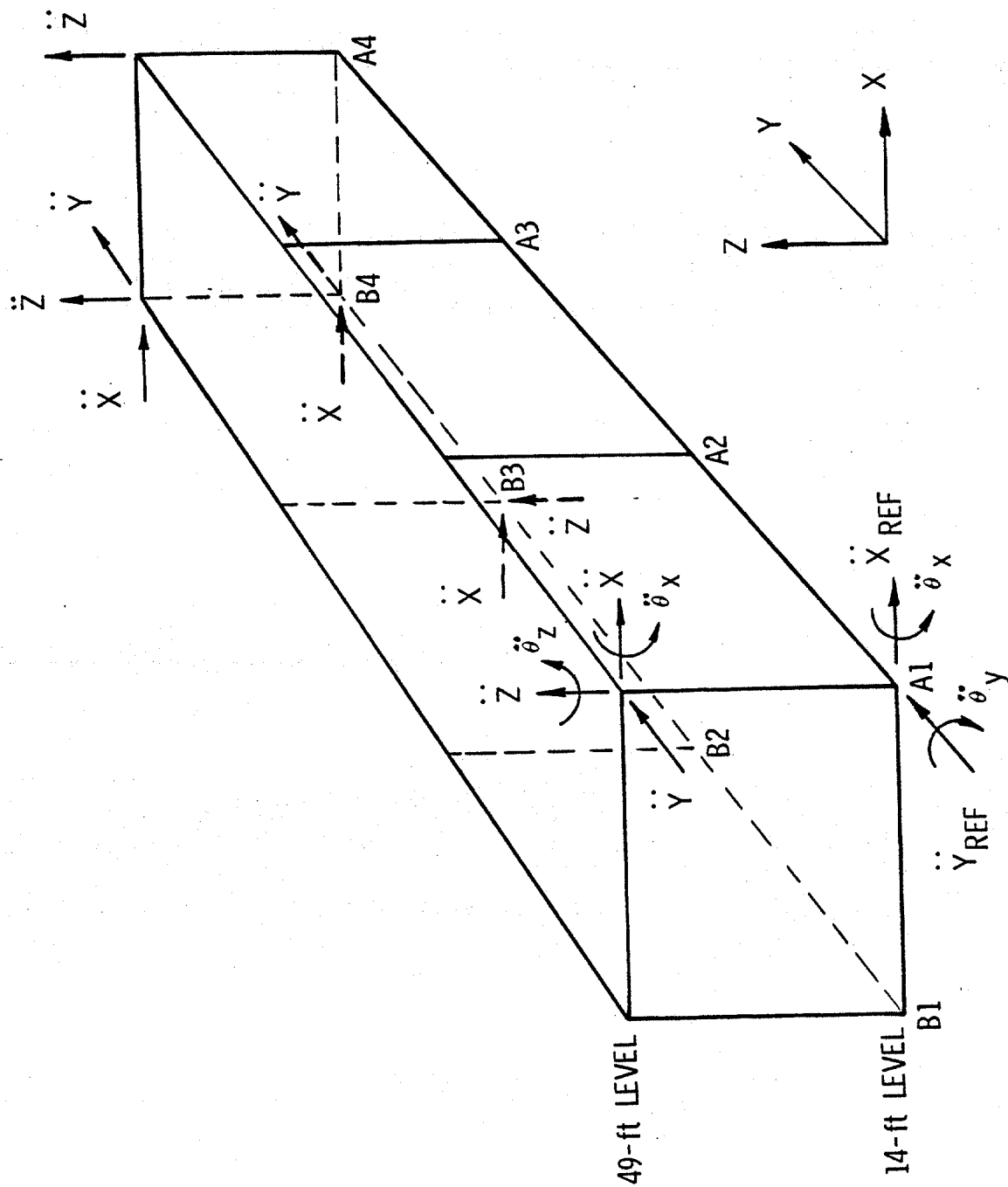


Figure C-8 Accelerometer Locations

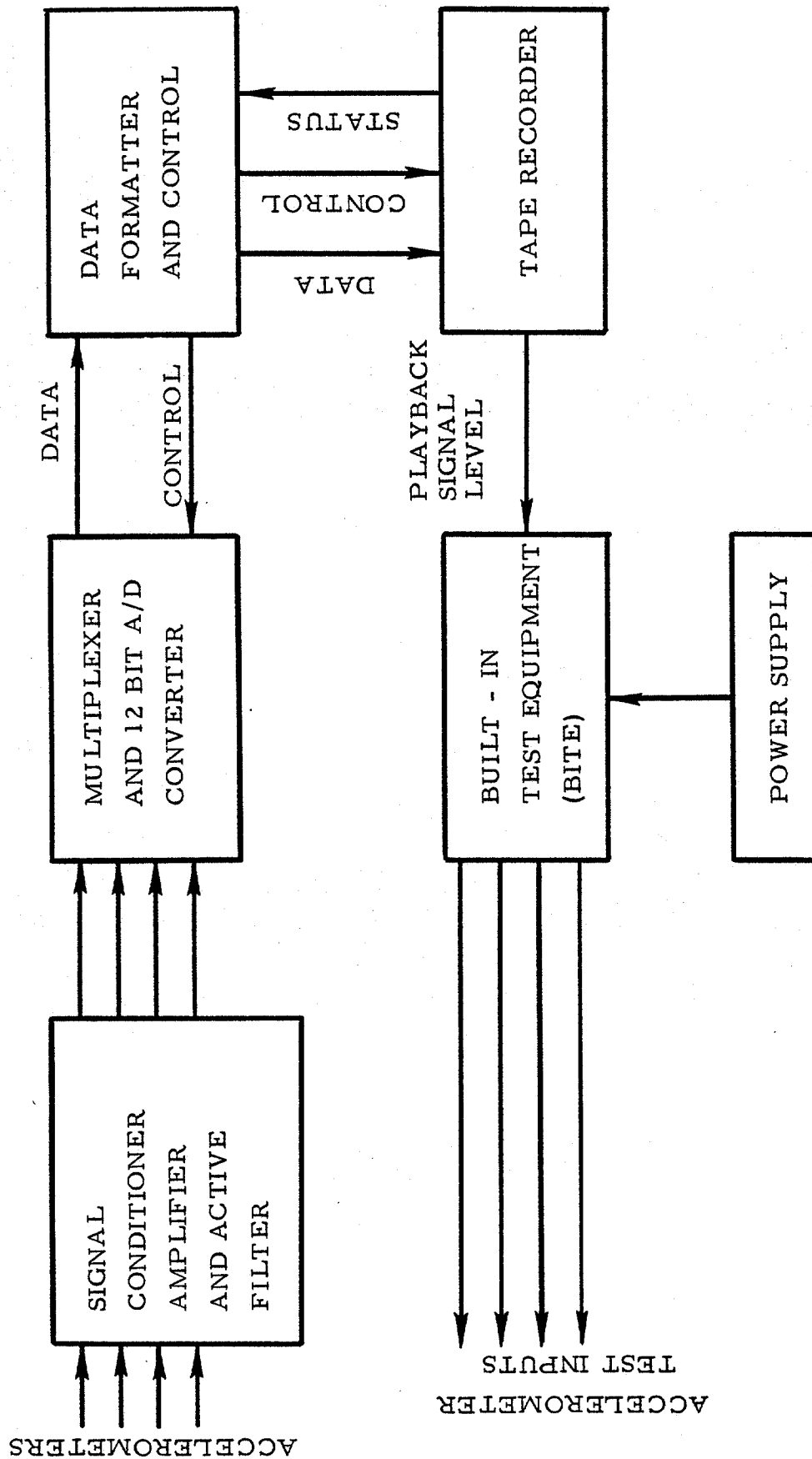
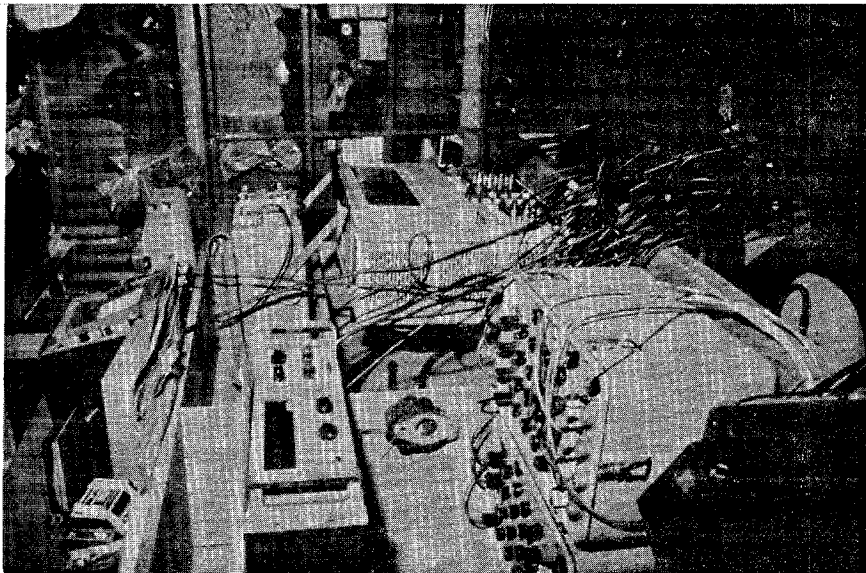
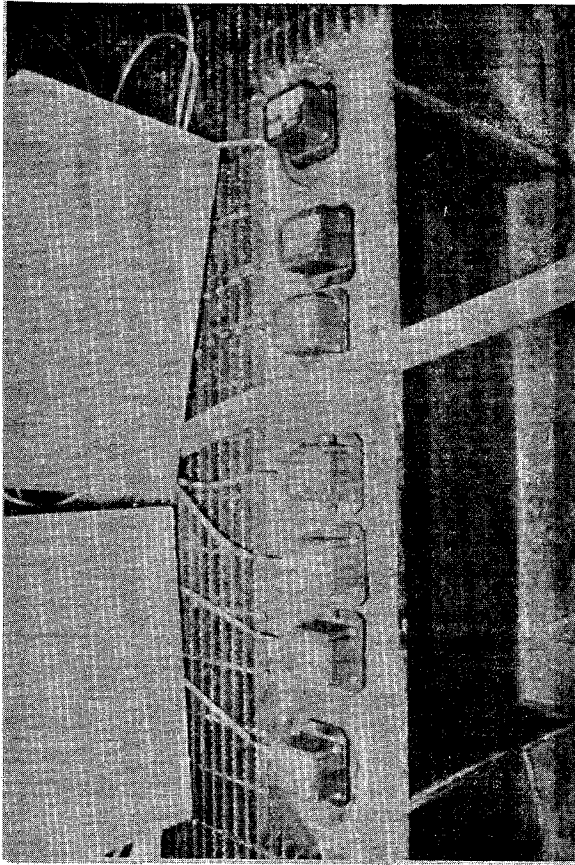


Figure C-9 Instrumentation Flow Chart



Recording and Signal Conditioning
Equipment Installed in Deck House



Calibrating the Accelerometers

Figure C-10. Instrumentation

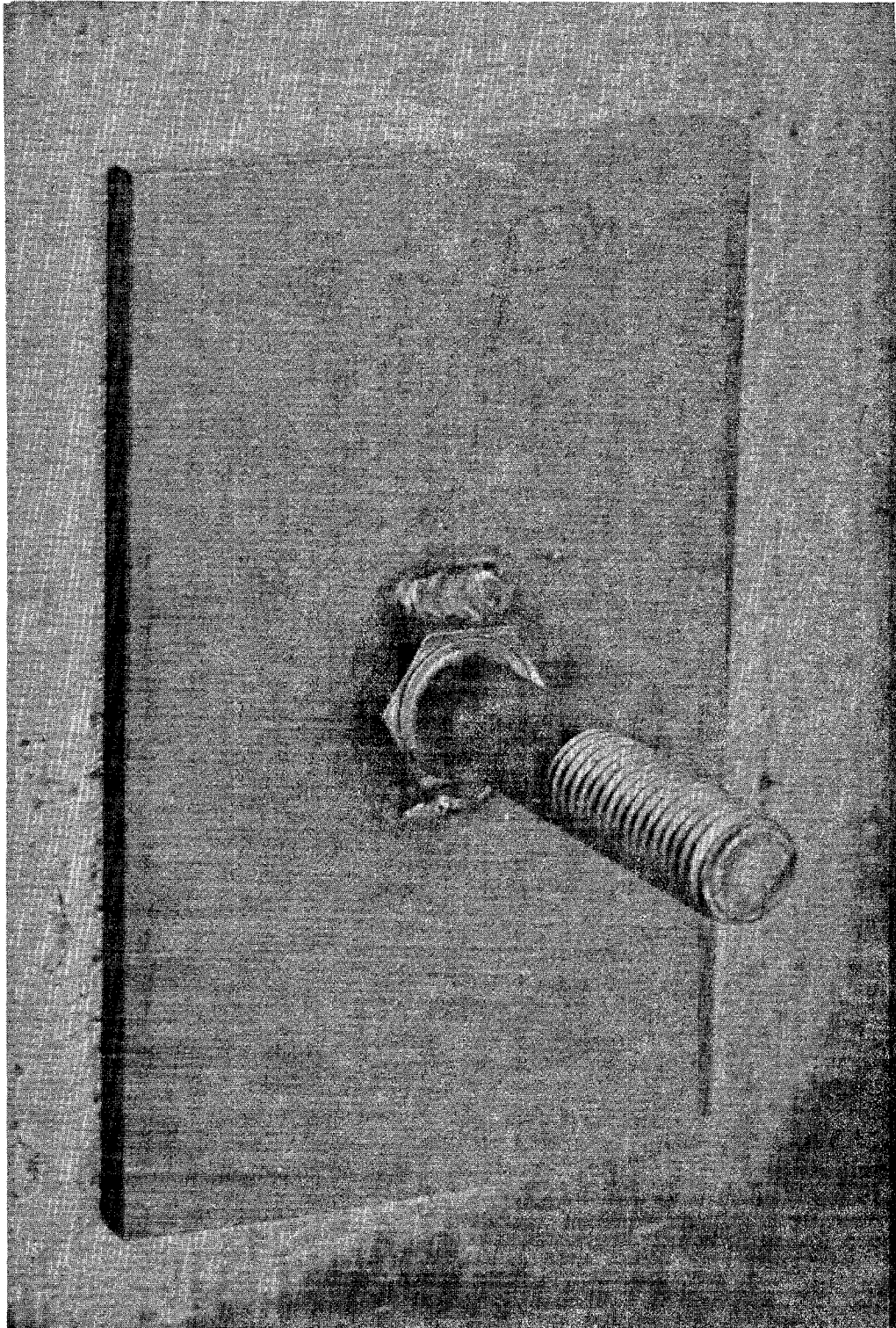


Figure C-11. Attaching Pad

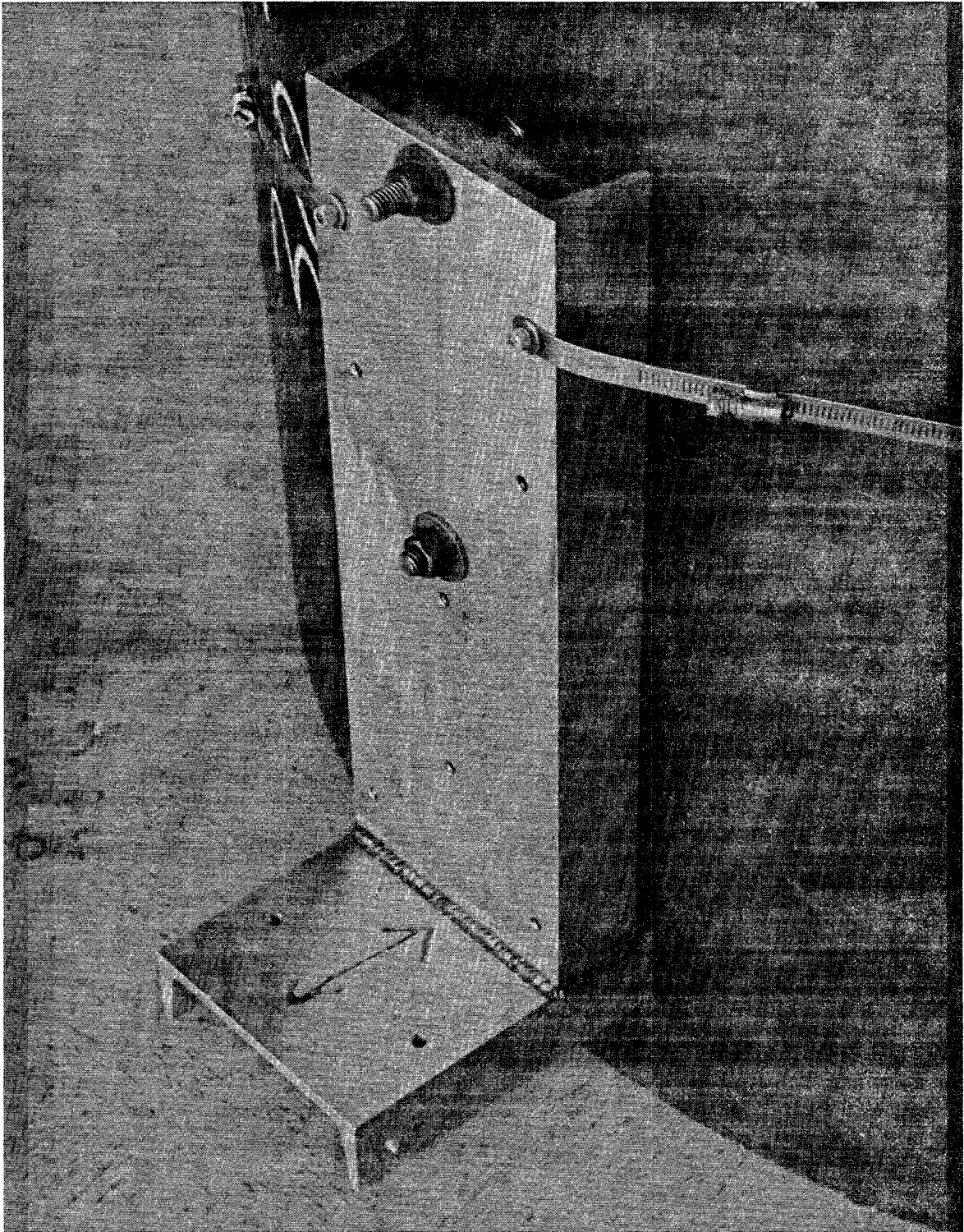


Figure C-12. Mounting Fixture Attached to Simulated Leg of Platform

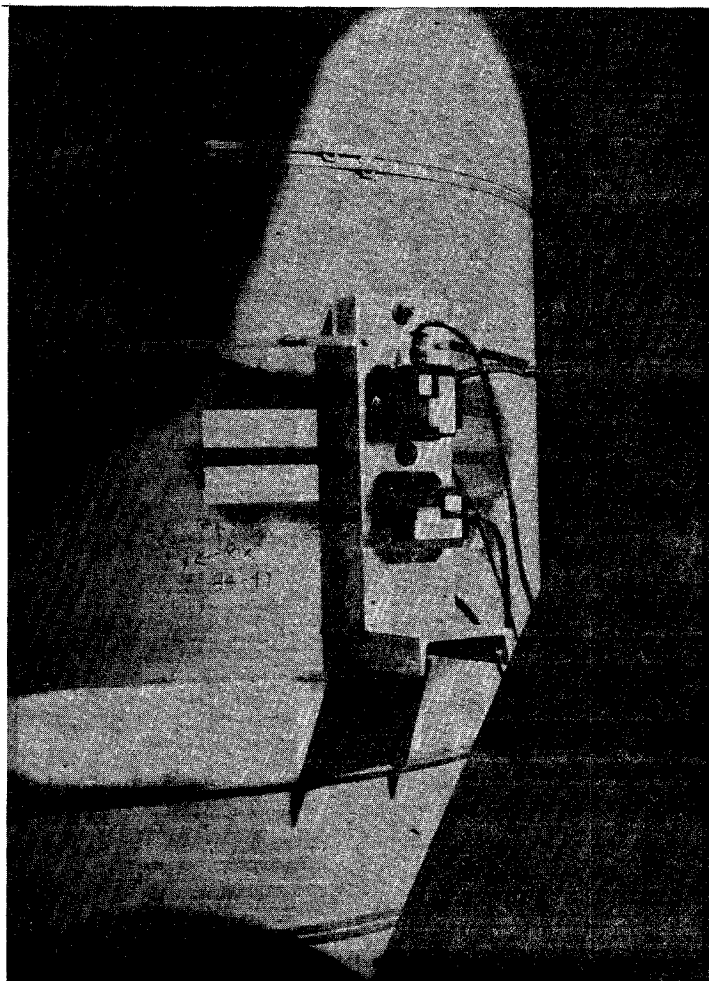


Figure C-13. Two Translational Accelerometers
Mounted on B-4 Leg

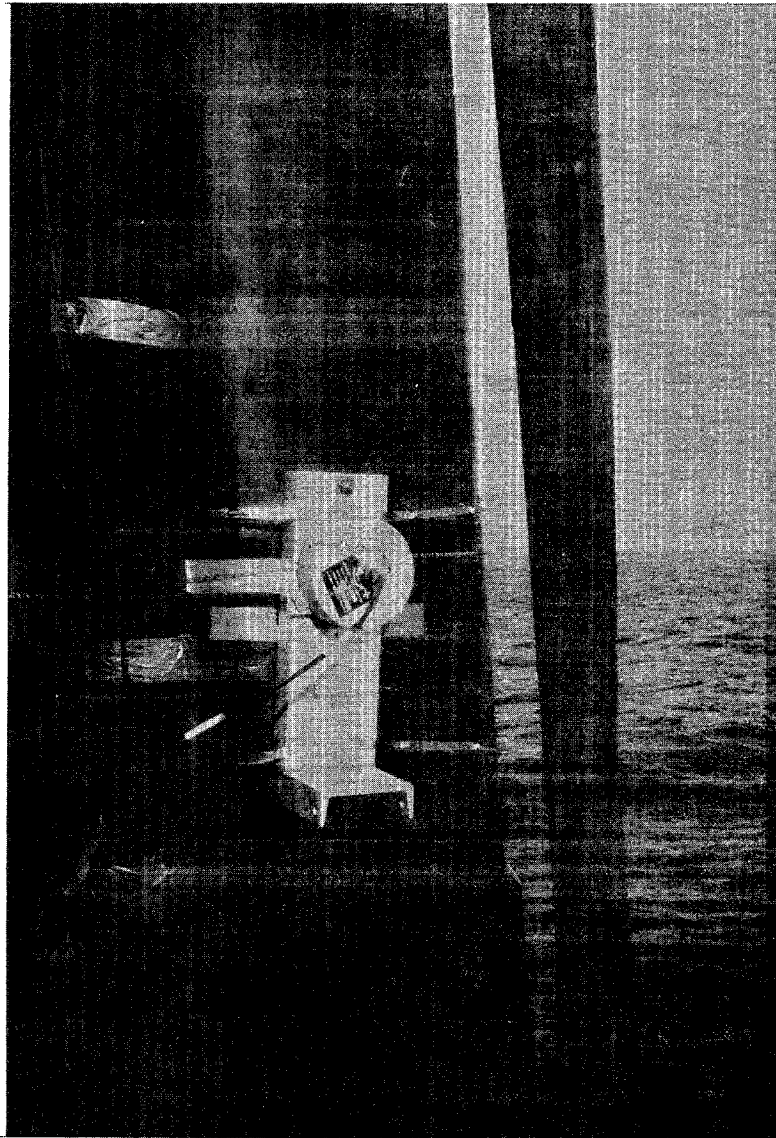


Figure C-14. Angular Accelerometer
Mounted on Leg